

Graphene and Boron Nitride Monolayers on Close-Packed Metal Surfaces: Growth and Interaction with Transition Metal Atoms

THÈSE N° 5639 (2013)

PRÉSENTÉE LE 1^{ER} MARS 2013
À LA FACULTÉ DES SCIENCES DE BASE
LABORATOIRE DE NANOSTRUCTURES SUPERFICIELLES
PROGRAMME DOCTORAL EN PHYSIQUE

ÉCOLE POLYTECHNIQUE FÉDÉRALE DE LAUSANNE

POUR L'OBTENTION DU GRADE DE DOCTEUR ÈS SCIENCES

PAR

Donat Fabian NATTERER

acceptée sur proposition du jury:

Prof. R. Houdré, président du jury
Prof. H. Brune, directeur de thèse
Prof. K. Albe, rapporteur
Prof. T. Greber, rapporteur
Prof. A. Kis, rapporteur



ÉCOLE POLYTECHNIQUE
FÉDÉRALE DE LAUSANNE

Suisse
2013

Abstract

This thesis presents a collection of experimental results that emerge from the interaction of the two related materials graphene (*g*) and hexagonal boron nitride (*h*-BN), with transition metal atoms, measured with a scanning tunneling microscope.

We describe the preparation of graphene on Ru(0001), and of hexagonal boron nitride on Rh(111) and Ni(111), respectively. In both cases the layer growth relies on the catalytic activity of the substrate to induce the pyrolysis of suitable precursor molecules at high temperature. This precursor is ethylene for *g*, and borazine for *h*-BN. Variations of the growth parameters allow for a preparation of a completely or, if desired, a partially covered surface.

For the deposition of transition metal atoms onto *h*-BN/Rh(111), we determine an initial sticking coefficient for Ti, Mn, Co below one. We investigate the evolution of Co island densities for different coverages at the temperatures of 10 and 50 K. The moiré pattern is shown to inhibit the inter-cell movement of Co adatoms at low temperature. For individual Mn, Fe, and Co adatoms a bi-stable adsorption complex was encountered, whereof one state is characterized by a sizeable weakening of the *h*-BN–substrate interaction, while the other leaves the interaction unchanged. Via tip manipulation we show the reversible switching between the two states and thus pinning and un-pinning the *h*-BN layer to and from the Rh(111) substrate.

By using Ti adatoms on *h*-BN on Ni(111) and Rh(111), we could establish how hydrogen from the residual pressure interacts with the sample even for base pressures as low as 5×10^{-11} mbar. The hydrogenation of a Ti adatom will result in a sizeable reduction of the apparent height, as well in the emergence of a Kondo feature in differential conductance (dI/dV). The interplay with hydrogen stimulated the development of an improved deposition routine that allowed for a dosing of transition metal atoms in the cleanliest fashion.

Through a deliberate dosing of molecular hydrogen we could prove the above interplay of hydrogen. In the course of those experiments we furthermore discovered a $(\sqrt{3} \times \sqrt{3})R30^\circ$ superstructure in which molecular hydrogen is stabilized. Measurements of dI/dV on molecules within this superstructure revealed an inelastic excitation reminiscent of a 3D rotational state. The latter was scrutinized with molecular deuterium and the energy shown to scale with 1/2, as expected for a rotational process.

Keywords: Scanning tunneling microscope, graphene, hexagonal boron nitride, layer growth, transition metal adatoms, layer detachment, hydrogen interplay, molecular rotations

Zusammenfassung

In der vorliegenden Arbeit werden Experimente mit einem Rastertunnelmikroskop vorgestellt, die sich mit der Adsorption von Übergangsmetallen (UM) auf den Oberflächen von Graphen (*g*) und hexagonalem Bornitrid (*h*-BN) beschäftigen.

Wir beschreiben das Wachstum von Graphen auf Ru(0001), beziehungsweise von *h*-BN auf Ni(111) und Rh(111). Die Methoden basieren auf der katalytischen Wirkung der Substrate, welche ein geeignetes Molekül bei hoher Temperatur dissoziieren. Dabei wird für *g* Ethen, und für *h*-BN Borazin als Precursor verwendet. Durch geeignete Wahl der Wachstumsparameter können partielle und vollständige Bedeckungen erzeugt werden.

Die Bedampfung von *h*-BN/Rh(111) mit UM lässt uns auf einen Haftkoeffizienten für Ti, Mn und Co, geringer als eins schließen. Wir untersuchen die Evolution der Inseldichten für Co in Abhängigkeit von der Dosis, jeweils bei den Temperaturen von 10 und 50 K. Es wird gezeigt, dass es Co Adatome bei tiefen Temperaturen nicht vermögen die Barriere in die nächste Moiré Einheitszelle zu überwinden. Für einzelne Adatome von Mn, Fe und Co, beobachten wir einen bistabilen Adsorptionskomplex. Der erste Zustand ist durch die Abschwächung der *h*-BN-Substrat Wechselwirkung gekennzeichnet. Der zweite Zustand lässt diese intakt. Wir demonstrieren die reversible Transformation zwischen diesen Zuständen mittels der Spitze des Rastertunnelmikroskops. Es ist dadurch möglich beliebig die *h*-BN Lage an das Substrat zu kleben, bzw. von diesem abzulösen.

Mittels einzelner Ti Adatome auf *h*-BN/Ni(111) sowie auf *h*-BN/Rh(111) konnten wir zeigen, dass der Restdruck des Vakuumsystems trotz seiner 5×10^{-11} mbar, zu einer Interaktion mit Wasserstoff führt. Die Adsorption von Wasserstoff auf Ti bewirkt einen starken Rückgang der gemessenen Höhe, sowie das Entstehen einer Kondo Resonanz an der Fermi-Energie in dI/dV Spektren. Wir entwickelten, angeregt durch die Beobachtung von Wasserstoff bedingten Einflüssen, eine verbesserte Depositionsstrategie, welche es uns erlaubt alle UM in reiner Weise aufzudampfen. Durch eine gezielte Aussetzung unserer Proben mit Wasserstoff konnten wir die obigen Annahmen überprüfen. Zudem entdeckten wir in diesen Experimenten eine $(\sqrt{3} \times \sqrt{3})R30^\circ$ Wasserstoff-Überstruktur. Die Vermessung einzelner Wasserstoffmoleküle in dieser Struktur zeigte uns inelastische Anregungen, welche mit einer Rotation erklärt werden können. Dies wurde mittels molekularem Deuterium überprüft, wobei sich die Anregungsenergie um den Faktor 2 änderte, wie es bei einer Rotation zu erwarten ist.

Schlüsselwörter: Rastertunnelmikroskop, Graphene, hexagonales Bornitrid, Wachstum, Übergangsmetalladsorbate, Schichtablösung, Wasserstoffwechselwirkung, molekulare Rotationen

Résumé

Ce travail présente l'adsorption de métaux de transition sur des surfaces de graphène (*g*) et de nitrure de bore hexagonal (*h*-BN), mesurée par microscopie à effet tunnel.

Nous étudions la croissance du *g* sur la surface de Ru(0001) et du *h*-BN sur les surfaces de Ni(111) et Rh(111). L'approche est basée sur l'activité catalytique d'une surface à haute température permettant de dissocier une molécule appropriée. Cette molécule est l'éthylène dans le cas du graphène, et la borazine dans le cas de la croissance du *h*-BN. Des variations des paramètres de croissance nous permettent de réaliser des surfaces partiellement ou entièrement couvertes.

La déposition de métaux de transition sur des surfaces de *h*-BN nous permet de déduire un coefficient de collage plus petit que un pour Ti, Mn, et Co. Nous déterminons l'évolution de la densité d'îlots de Co en fonction du recouvrement à des températures de 10 et 50 K. Il est démontré qu'à basse température un adatome de Co n'arrive pas à surmonter la barrière entre deux mailles du réseau moiré. Pour des atomes de Mn, Fe, et Co, nous montrons l'existence d'un complexe d'adsorption bistable. Son premier état est caractérisé par un affaiblissement de la liaison entre la couche de *h*-BN et le substrat. Par contre, le second état ne modifie pas l'interaction. À l'aide de la pointe de notre microscope à effet tunnel nous pouvons changer le complexe arbitrairement entre ces deux états, ce qui signifie que nous pouvons coller ou décoller localement la couche de *h*-BN.

L'observation des adatoms de Ti sur les surfaces du *h*-BN/Ni(111) et *h*-BN/Rh(111) nous a fait réaliser que l'effet de hydrogène est non négligeable même si la pression résiduelle du système est de l'ordre de 5×10^{-11} mbar. L'hydrogénation d'un atome de Ti provoque une réduction de sa hauteur apparente, et l'émergence d'un effet Kondo, dont la signature est visible dans les spectres dI/dV au niveau de Fermi. Vu que la présence d'hydrogène mène à des tels effets, nous avons amélioré notre façon de déposer les métaux de transition, ce qui nous permet de les doser le plus proprement possible. L'exposition délibérée de notre système à de l'hydrogène moléculaire a aussi généré les effets décrits ci-dessus. De plus, nous avons constaté la formation d'une superstructure $(\sqrt{3} \times \sqrt{3})R30^\circ$ d'hydrogène qui stabilise les molécules sur la surface. Sur ces molécules nous observons des excitations inélastiques dont l'énergie correspond à celle d'une rotation. Le dosage de deutérium moléculaire montre une excitation à une énergie deux fois plus basse, comme c'est attendu pour une rotation.

Mots-clés : microscope à effet tunnel, graphène, nitrure de bore hexagonal, croissance, métaux de transition, détachement de couche, interaction avec hydrogène, rotations moléculaires.

Contents

Abstract (English/Français/Deutsch)	i
List of figures	viii
1 Introduction	1
2 Scanning tunneling microscope	5
2.1 Principle of operation	5
2.2 Experimental setup	8
2.2.1 dI/dV spectroscopy	9
2.2.2 $d\ln I/dz$ spectroscopy	10
2.2.3 $d\ln I/dz$ spectroscopy for flexible tunneling junctions	10
2.2.4 STM data recording and image treatment	12
3 Monolayers of hexagonal boron nitride on close packed metal substrates	13
3.1 Growth of hexagonal boron nitride films	13
3.1.1 h -BN/Ni(111)	15
3.1.2 h -BN/Rh(111)	17
3.2 Adatom adsorption on metal supported h -BN	22
3.2.1 Ti on h -BN/Ni(111) and h -BN/Rh(111)	23
3.2.2 Mn, Fe and Co on h -BN/Rh(111)	29
3.2.3 Ring state for Mn, Fe and Co adatoms	36
3.2.4 Xe on h -BN/Rh(111)	50
3.3 Hydrogen related observations for Ti and Co adatoms	52
4 Graphene	57
5 Outlook and perspective	69
5.1 Au intercalation	69
5.2 Hydrogen superstructure - molecular rotations	73
A Appendix	79
Bibliography	93
Curriculum Vitæ	94
	vii

Contents

Acknowledgements

97

List of Figures

1.1	Graphite and boron nitride lattice.	1
2.1	Schematic view of a scanning tunneling microscope.	6
2.2	Differential conductance from $I - V$ traces and Lock-In amplifier.	9
2.3	$I - z$ data.	11
2.4	Apparent barrier height for flexible tunneling junctions.	12
3.1	Structural formula of borazine.	14
3.2	h -BN/Ni(111).	15
3.3	h -BN covered sputter holes on Ni(111).	16
3.4	h -BN/Rh(111)	18
3.5	Field emission resonance spectra on metal supported h -BN.	20
3.6	Sample with h -BN partially covering Rh(111) surface.	21
3.7	Analysis of partially h -BN covered Rh(111) surface.	22
3.8	Mean island size for statistical growth as a function of coverage.	22
3.9	Ti deposition on Rh(111) and Ni(111) supported h -BN at 10 K.	24
3.10	Height analysis of clean and hydrogenated Ti adatoms on h -BN/Ni(111).	25
3.11	Transformation of an ensemble of Ti adatoms by a bias pulse.	26
3.12	Differential conductance of hydrogenated Ti adatom.	28
3.13	Co islands at varying exposure for temperatures of 10 and 50 K.	30
3.14	Determination of initial sticking coefficient, mean island size, and island density.	32
3.15	Arrhenius plot of Co island densities on h -BN/Rh(111)	34
3.16	Mn, Fe, and Co rings.	42
3.17	$z - V$ spectroscopy on Co ring.	43
3.18	Evaluation of Mn dot ring populations.	44
3.19	Transformation of dots into rings via tip manipulation.	45
3.20	Bistable Mn ring.	46
3.21	Measuring h -BN deformation.	47
3.22	h -BN deflection at small tip-sample separation.	48
3.23	Spectroscopy on Mn ring and dot state.	50
3.24	Xe rings on h -BN/Rh(111).	51
3.25	Gradual hydrogenation of Ti adatoms at 50 K.	52
3.26	Hydrogen interference from desorption at elevated temperature.	54

List of Figures

3.27	Desorption from cryostat walls while increasing the temperature.	55
5.1	Intercalation of Au underneath <i>h</i> -BN/Ni(111).	70
5.2	Details of intercalated Au structures on <i>h</i> -BN/Au/Ni(111).	71
5.3	Mn rings on intercalated Au on <i>h</i> -BN/Ni(111).	72
5.4	Hydrogen superstructure on <i>h</i> -BN/Ni(111).	74
5.5	Differential conductance of hydrogen/deuterium molecules in superstructure.	76
A.1	Vibrational underground in labs H0482 and H1442.	80
A.2	Time evolution of UHV chamber assembly in lab H0482.	81

1 Introduction

If one was to arrange atoms at the corners of a honeycomb lattice, and if these atoms were carbon, one would have created the famous two dimensional (2D) crystal, notoriously known as graphene (*g*). The carbon atoms of this lattice are sp^2 hybridized and threefold coordinated with respect to their nearest neighbor atoms to which they are covalently bound. Similarly, if one was to replace alternately one C atom by a boron, and one C atom by a nitrogen atom, the resulting crystal would be known as hexagonal boron nitride (*h*-BN). While the π derived electrons in graphene are delocalized and responsible for many of the peculiar transport properties, the corresponding electrons in *h*-BN are bound to the nitrogen atom. This subtle difference between the two isoelectric materials entails that graphene is a zero-gap semiconductor whereas *h*-BN is a large gap isolator. As a consequence of their true 2D structure, many interesting properties emerge. Disregarding the already mentioned peculiar transport characteristics, other curious properties are, for instance, that one sheet of graphene or *h*-BN represents the lowest physically possible thickness of a material. This material can then be regarded as the prototype of an ideal 2D membrane.

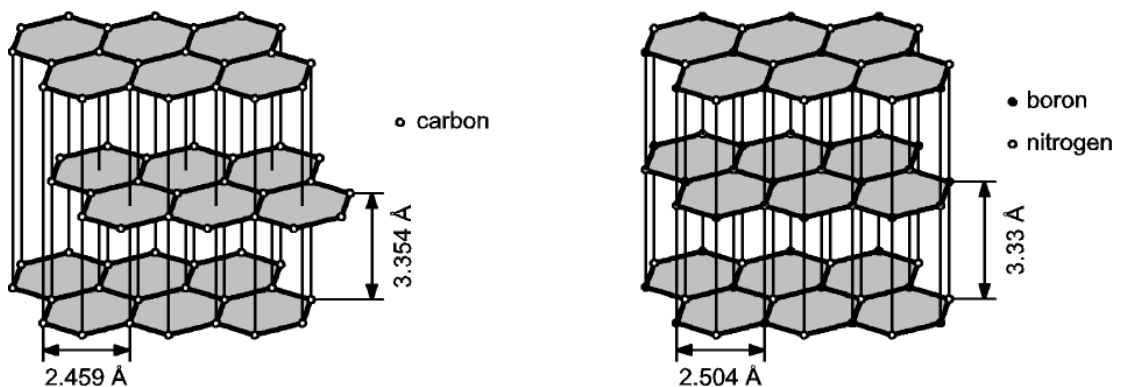


Figure 1.1: Graphite and hexagonal boron nitride stacking sequence and lattice parameters. Figure from Wiechert [144].

The investigation of the intrinsic properties of freestanding graphene and *h*-BN has become a large field of research. This is but the beginning. Exponentially more intriguing properties emerge through the interaction of these 2D layers with various substrates. Following this line of thought, one could stack a layer of graphene on another one, and would have created bilayer graphene. Depending on the stacking sequence, which could either be AB or AA, the resulting properties are quite distinct [103]. If many graphene layers are stacked together in the sequence ABAB, the corresponding bulk structure would be known as graphite, which is shown in Fig. 1.1. This layered crystal is characterized by a weak inter-layer van der Waals attraction. Similarly, the layered crystal of *h*-BN exhibits the equivalent weak inter-layer attraction. It is for this reason why graphite and *h*-BN are attractive lubricants in technical applications, and why the micro mechanical cleaving with adhesive tape, pioneered by Novoselov, Geim, and co-workers [97, 98], allows the creation of a single atomic sheet of graphite, *h*-BN, molybdenite, and related 2D materials.

Instead of stacking graphene or *h*-BN onto itself, these single sheets can be put on a lattice matched metallic substrate. The resulting interaction of the layer and the substrate can have a considerable different nature and modify the properties of both participating materials. The weak van der Waals attraction is completely replaced by a strong chemical interaction for the case of *h*-BN/Ni(111) which is characterized by a sizeable hybridization with the metal substrate [87, 7, 109]. This system is the focus of section 3.1.1. For a substrate with a different lattice parameter, the interaction of graphene and *h*-BN with the respective metal surface will be strongly inhomogeneous. The interaction is found to be modulated with the same periodicity as the resulting moiré pattern that results from the lattice mismatch of layer and substrate. Examples that are included within this thesis are the moiré structures of *h*-BN/Rh(111)-(12 × 12) [36, 110], examined in section 3.1.2, and *g*/Ru(0001)-(23 × 23) [82, 81, 84], focus of chapter 4. In both cases, the bonding between the layer and the substrate is locally modulated. Distinct regions are formed that are strongly hybridized with the substrate as well as areas that are only weakly attracted to the supporting substrate. A further degree of complexion is obtained from the relative rotation of the two lattice planes, as yet another moiré periodicity develops [93] with the corresponding local variations in the interaction strength between layer and substrate.

If we turn the carousel of changes to its extremes, for instance, by reducing the size of the metal substrate down to a small number atoms or even down to the individual atom, one can investigate the properties that arise from the interaction of an adsorbate with the surfaces of *h*-BN and graphene. For the latter, it was shown that a periodic array of Ir clusters arranged into a superlattice [92] could introduce a band-gap [115] in *g*/Ir(111).

For the case of individual transition metal atoms dosed onto *h*-BN/Rh(111) at low temperature, we found an initial sticking coefficient below unity. Upon dosing Mn, Fe, and Co, we discovered a bi-stable adsorption complex that is characterized by a strong perturbation of the *h*-BN–substrate interaction. Individual atoms of Mn, Fe, and Co were shown to locally detach the *h*-BN layer from the metal surface [89]. The two states exhibit a very peculiar topography.

While one state is imaged with a scanning tunneling microscope (STM) as a circular structure, the other state is seen as an individual protrusion, as expected for a single adatom. From a thorough analysis we could deduce that the attraction between the STM tip and the *h*-BN layer locally lifts the latter off the substrate. This deflection of the *h*-BN layer from the substrate takes us back to the beginning of this introduction, where *h*-BN was mentioned as being the ideal membrane. We show that we can reversibly switch the two states with the tip of our STM, and thereby pin and unpin the *h*-BN layer to and from the Rh substrate. These findings represent the major results of this contribution and are the topic of section 3.2.3.

In the outlook of section 5.1 we will allude to the intercalation of gold underneath a layer of *h*-BN that reverts the originally strong hybridization with the Ni(111) substrate and leaves the *h*-BN layer floating, and merely attached by van der Waals attraction to the intercalated Au islands. Curious one dimensional wire structures spread out from intercalated Au islands that may form a connected honeycomb structure reminiscent of the known moiré pattern of *h*-BN/Rh(111)-(12 × 12). Dosing of manganese allows to potentially generalize the above discussed findings for a local detachment of the *h*-BN layer. Circular structures were observed to behave in the same way as the above mentioned Mn, Fe, and Co rings.

In a final note in section 5.2, we will discuss exciting prospects of using the surface of *h*-BN as a decoupling layer to attenuate the interaction of the substrate with an adsorbate. This allows for a study of the intrinsic adsorbate properties, and we inspect and report rotational excitations of hydrogen and deuterium molecules.

Hydrogen has received a lot of attention throughout our contribution, since it was found to strongly interfere with the structures under study, even if the ultra-high vacuum system was in the low 5×10^{-11} mbar range. Our results were therefore scrutinized for a possible hydrogen interplay, and the corresponding problematic is presented in section 3.2.1 and section 3.3.

2 Scanning tunneling microscope

This chapter is devoted to our principal tool of investigation used in this study, the scanning tunneling microscope (STM). Since its invention by Binnig and Rohrer in 1982 [21], the STM has seen a tremendous development and the technique undergone a pronounced maturing. As beautifully expressed in the Nobel lecture of Binnig and Rohrer in 1986 [20], they have seen the birth of STM, its adolescence and witnessed its departure for a time of travel. Nowadays, the STM has become a widely employed instrument as ready-made units are commercially available alongside with its close relative, the atomic force microscope (AFM). Atomic resolution of surfaces and controlled manipulation of objects at the atomic scale are routinely achieved. Furthermore, scanning tunneling spectroscopy (STS) with high energy resolution is readily employed in the study of local electronic excitations. Naturally, a huge body of literature covering all aspects of this technique has evolved in the course of time (refer for instance to the review of Chen [33]). In view of the high abundance of this instrument in laboratories around the globe, we limit ourselves to describing the principal modi of operation that are also directly related to our main experimental results.

2.1 Principle of operation

The principle of operation of an STM is intriguingly simple. A sharp metallic tip is approached to a conducting sample and laterally scanned along the surface by piezoelectric actuators. This basic idea is illustrated in Fig. 2.1(a). Already before the actual physical contact, at a tip-sample separation of the order of a few angstroms (10^{-10} m), electrons can traverse the vacuum gap between the electrodes by the quantum mechanical effect of tunneling. A tunneling current flows as long as the Fermi levels between the electrodes are imbalanced. In order to establish a continuous tunneling current [cp. Fig. 2.1(b)], a bias voltage is applied between tip and sample that shifts the previously aligned Fermi levels (at $V_t = 0$) with respect to another by eV_t (e denotes the electron charge).

The constant current mode is the predominant modus operandi in STM. Hereby, the tunneling current is kept constant by the feedback-loop through varying the tip-sample separation with

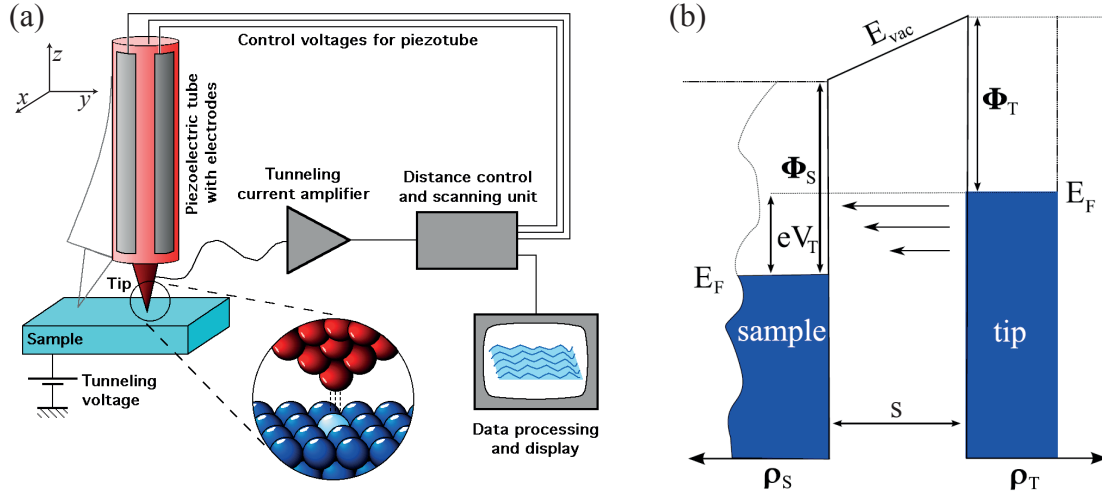


Figure 2.1: (a) Schematic view of a scanning tunneling microscope (figure by Michael Schmid, TU Wien). (b) DOS diagram of tip and sample with applied bias voltage V_T . Figure adapted from Ternes [132].

the z -piezo in order to match a desired current setpoint, typically of the order of pico to nano amps. When the tip is scanned laterally along the surface it follows the sample topography and the computer control records maps of vertical tip displacements $\Delta z(x, y)$.

The feedback control is facilitated by the exponential response of the tunneling current to variations of the tip–sample separation (Δs) which allows for a precise vertical tip positioning. The tunneling current for a 1D barrier is written as follows:

$$I_t(\Delta s) = I_t(0) \exp(-2\kappa \Delta s) \quad (2.1)$$

$$\kappa = \sqrt{\frac{2m\Phi}{\hbar^2}}$$

where m , \hbar and Φ are the electron mass, the reduced Planck's constant and the apparent barrier height, respectively. For the approximation of a trapezoidal tunneling barrier one can write $\Phi = \frac{\Phi_T + \Phi_S - eV}{2}$ [123], where Φ_T and Φ_S are tip and sample work function. A frequently used practical expression is $I_t(\Delta s) = I_t(0) \exp(-1.025\sqrt{\Phi}\Delta s)$ where Φ is expressed in units of electron volt and s in angstrom. Accordingly, for every angstrom change in the electrode separation, the tunneling current varies by about one order of magnitude (for a typical barrier height of 4–5 eV).

In order to study the electronic structure of the sample with spectroscopy, we apply Bardeen's formalism [12] for 1D tunneling that relates the tunneling current to the properties of two

planar electrodes¹:

$$I_t(V_t) = \frac{4\pi e}{\hbar} \int_{-\infty}^{\infty} d\epsilon \rho_S(\epsilon) \rho_T(\epsilon - eV_t) [f(\epsilon) - f(\epsilon - eV_t)] \times |M(\epsilon)|^2$$

$$f(\epsilon) = \frac{1}{1 + \exp\left[\frac{\epsilon}{k_B T}\right]}$$
(2.2)

Here, $\rho_{T,S}$ describe the density of states (DOS) of tip and sample, $f(\epsilon)$ the Fermi distribution function, and M the tunneling matrix element, respectively. The factor M denotes the probability flux between the two electrodes by the overlap of their respective wave functions and M carries the exponential current-distance dependence [12]². In a simplified picture, which is a good approximation at low bias voltage ($eV_t \ll \Phi$) and zero temperature, the energy dependence of the tunneling matrix element is irrelevant and M assumes a constant value at fixed gap width. Inserting this approximation into Eq. 2.1 and deriving with respect to V , we obtain the differential conductance:

$$\left. \frac{dI_t}{dV} \right|_{V_t} = \frac{4\pi e^2}{\hbar} \rho_S(E_F + eV_t) \rho_T(E_F) |M|^2$$
(2.3)

One recognizes from the convolution in Eq. 2.2 that, apart from M , a proper knowledge of either electrode is required in order to characterize the other. However, usually the tip DOS is assumed to be constant³, that is, featureless, and thus Eq. 2.3 is directly proportional to the sample DOS. It is for this reason that frequently differential conductance and sample DOS are interchangeably used. Since spectroscopy is performed with the tip at a distinct position we actually probe the local density of states (LDOS) of the sample. We note that an analytical account of the tunneling matrix element is given by Tersoff and Hamann [133] for a spherical tip and the approximation of a s -like tip orbital.

Another spectroscopy approach is the barrier height determination which relies on the z dependence of the tunneling current. Revisiting Eq. 2.1, applying the approximation of small bias voltage and considering the exponential gap width dependence of the tunneling current, we can write [58]:

$$\frac{d \ln I_t}{ds} = -2\kappa.$$
(2.4)

The parameters are the same as in Eq. 2.1 and valuable information about the local work function can be harvested from this approach. The apparent barrier height is defined as [33]:

$$\Phi = \frac{\hbar^2}{8m} \left(\frac{d \ln I_t}{ds} \right)^2 \approx 0.95 \left(\frac{d \ln I_t}{ds} \right)^2$$
(2.5)

¹ Here we principally follow the formulation and nomenclature of Chen [33]. Note that the energy scale refers to the common chemical potential of tip and sample.

² The tails of the wave functions decay exponentially into the vacuum.

³ Experimentally, great an effort is undertaken in order to prepare a tip with such conditions, *i.e.*, by small voltage pulses, field emission or gentle collisions with the sample surface.

We wish to note at this point that the tip displacement Δz and the change in gap width Δs are generally used synonymously, *i.e.*, $\frac{ds(z)}{dz} = 1$ is assumed to hold. However, we will highlight an important exception to this assumption in the following section where the actual experimentally accessible quantity is $\frac{d \ln I_t}{dz}$ and not $\frac{d \ln I_t}{ds}$.

2.2 Experimental setup

The measurements of this study were carried out with three different homemade STM in ultra high vacuum (UHV). For the investigation of graphene growth, presented in chapter 4, an STM at the EPFL [75], and at the APE beamline [102] at the ELETTRA synchrotron facility were used. The study of *h*-BN on close packed metal surfaces, reported in chapter 3, was carried out with a third STM at the EPFL [48], and preliminary results of Bulushek [29] were realized with the STM mentioned before for graphene [75]. The difference between the employed instruments is the effective temperature range for which they have been designed. For instance, the STM of Ref. [75] can operate at variable temperature of 60–800 K, the STM of Ref. [48] runs typically at 4.7 or 50 K, and the ELETTRA instrument works at room temperature. The common characteristic of these instruments are the UHV environment in which they are accommodated, and the efforts that are made in order to decouple the STM from mechanical vibrations.

Modulation techniques

The spectroscopic characterization of the samples were carried out by so called modulation techniques. In these approaches an external control parameter (*i.e.*, bias voltage, *z*-piezo actuator) is modulated by a small periodic perturbation and the concomitant reaction of the tunneling junction detected by a Lock-In amplifier. For differential conductance measurements the bias voltage is modulated, and for performing *z*-spectroscopy a small tip vibration is superimposed on the *z*-piezo displacement. In principle, already recording $I - V$ and $I - z$ traces without modulation allows for performing spectroscopy by numerically deriving the latter curves to determine the sought sample properties by Eqns. 2.3 and 2.4. However, it turns out that the signal to noise ratio is rather poor and that many spectra need to be averaged in order to improve the quality of the data⁴. The advantages of the modulation techniques are their better signal to noise ratio and the natural connection to the sample properties found from Eqns. 2.3 and 2.4, *i.e.*, the Lock-In signal is directly proportional to the differential conductance and work function, respectively.

A thorough account for STS is given by Ternes [132] for our principally employed low temperature STM [48]. Here we outline the principal aspects of the first reference that are relevant for differential conductance measurements and we will dwell in more detail on *z*-spectroscopy in the second part.

⁴The standard deviation per data point is of order \sqrt{N} , where N is the number of averaged spectra.

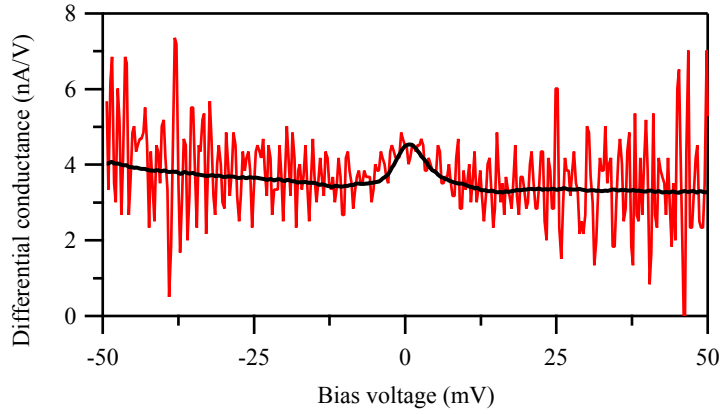


Figure 2.2: Differential conductance spectra of a hydrogenated Ti adatom [more details in section 3.2.1] from a numerically differentiated $I - V$ trace (red), in comparison with data directly obtained from a Lock-In amplifier (black). Although three curves each were recorded and averaged, the signal to noise ratio is much better for the Lock-In data. The Lock-In conductance was calibrated with the help of the $I - V$ trace. Setpoint before opening the feedback-loop: $V_t = -50$ mV and $I_t = 200$ pA.

2.2.1 dI/dV spectroscopy

In order to record the differential conductance, we added an alternating voltage from an external function generator to the bias voltage at a desired frequency ν , and used a Lock-In amplifier to detect the first harmonics for $\frac{dI_t}{dV}$, and the second harmonics for $\frac{d^2I_t}{dV^2}$ spectra. Typically a modulation voltage of the order of 10 mV at 397 Hz for point STS was used. A measurement routine includes (i) the stabilization of the tip at a setpoint current and bias, (ii) opening of the feedback-loop, (iii) varying the bias voltage in the chosen energy interval, and (iv) recording the concomitant response of current and differential conductance. As mentioned earlier, $I - V$ traces are typically not consulted for studying the spectroscopic characteristic of the sample, however, they allow to transfer the calibration onto data obtained from the Lock-In amplifier. An example of the latter is given in Fig. 2.2.

If the spatial differential conductance is of interest, *i.e.*, for mapping the local density of states, many $\frac{dI_t}{dV}$ point spectra need to be recorded, which is a time-consuming task. However, one can either reduce the density of points at which $\frac{dI_t}{dV}$ spectra are taken, or measure differential conductance maps at a single energy. For a $\frac{dI_t}{dV}$ map measurement the bias modulation frequency is set to a value much higher than the response time of the engaged feedback-loop and accordingly the gap width remains largely unaffected. From such an approach two data sets are generated when laterally scanning with STM. One contains the usual topographic information and the other the local $\frac{dI_t(x,y)}{dV}$ at one selected energy eV_t . This approach drastically quickens the recording time, however, at the cost of a significantly reduced information depth, since the differential conductance is only recorded at one energy. A frequently employed strategy is therefore to scrutinize point spectra for energies of pronounced differences and measure $\frac{dI_t}{dV}$ maps accordingly. In a first step, this serves to illustrate the approximate LDOS

variations at the scale of the STM image. In a second step, point spectra are consulted in order to present the LDOS of a structure in a more complete manner.

2.2.2 $d \ln I / dz$ spectroscopy

The z -spectroscopy can be carried out by recording current-distance ($I - z$) traces and numerically deriving the latter to yield information on the tip-sample apparent barrier height via Eq. 2.5. As mentioned earlier, the signal to noise ratio is rather poor in this approach but it can be greatly improved by employing a modulation technique. Hereby a small vibration of the tip is superimposed on the actual vertical tip displacement by adding a sinusoidal voltage to the z -piezo actuator that results, in the present case, in a 16 pm peak-to-peak modulation of the tip apex. The bandwidth of the current preamplifier is much smaller than the modulation frequency, which is in the present study mostly 777 Hz, and the measured tunneling current in consequence a time average over one oscillation cycle [50]. Furthermore, limitations of the preamplifier dynamic range and the form of Eq. 2.4 make it favorable to detect $\frac{d \ln I_t}{ds}$, *i.e.*, a signal that is directly related to the apparent barrier height via Eq. 2.5. In order to record the apparent barrier height, we feed the output of the preamplifier into a logarithmic amplifier before directing the signal into the Lock-In detector. A measurement routine for point spectra includes (i) the stabilization of the tip at a setpoint current and bias, (ii) opening of the feedback-loop, (iii) varying the gap width by approaching or retracting the tip, and (iv) recording the concomitant response of current and the $\frac{d \ln I_t}{dz}$ signal. In agreement with the previous discussion of the differential conductance, $I - z$ traces can serve to transfer the calibration to the data obtained from the Lock-In amplifier as is exemplified in Fig. 2.3. The inspection of the signal to noise ratio clearly advocates the Lock-In approach.

In analogy to aspects of the previously described $\frac{dI_t}{dV}$ maps, the corresponding imaging mode can also be applied to record maps of $\frac{d \ln I_t(x,y)}{dz}$ and hereby image local local variations of the apparent barrier height for rigid tunneling junctions, or, as we will see later, local deformations of the tunneling junction due to tip sample interactions, respectively. The latter is the main result of this contribution and will be treated in more detail in chapter 3.

2.2.3 $d \ln I / dz$ spectroscopy for flexible tunneling junctions

In the sofar discussed z -spectroscopy, dz and ds were used interchangeably, *i.e.*, the imposed tip displacement was assumed to be commensurate with the varying gap width of the tunneling junction. An important exception is given for flexible sample or tip geometries. In such cases, deformations of the respective electrode render the description of the gap width more elaborate, and we have to consider in the derivative of the current of Eq. 2.4 that [34]:

$$\left(\frac{d \ln I_t}{ds} \right) = \left(\frac{d \ln I_t}{dz} \right) \left(\frac{dz}{ds} \right) \quad (2.6)$$

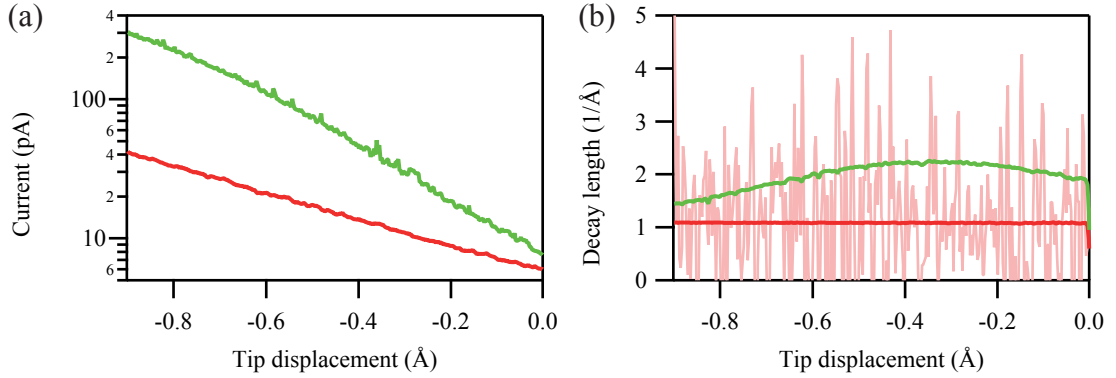


Figure 2.3: (a) Current-distance traces and (b) the resulting decay length of a Rh(111) supported *h*-BN layer. In subfigure (b) $d \ln I_t / dz$ data from the Lock-In amplifier is superimposed on a mean of three numerically differentiated $I - z$ traces. The latter exhibit a noisy background around the mean decay length of $\kappa = 1.1 \text{ \AA}^{-1}$. As expected, the decay length of this curve is constant whereas the green curve varies with tip displacement, *i.e.*, being a remainder of a sample deformation [more details in chapter 3]. The Lock-In data was calibrated with the help of the red $I - z$ trace and insertion of κ into Eq. 2.5 yields an apparent barrier height of $\Phi = (4.6 \pm 0.6) \text{ eV}$. Setpoint before opening the feedback-loop: $V_t = -100 \text{ mV}$ and $I_t = 5 \text{ pA}$.

The experimentally accessible quantity is the factor $\frac{d \ln I_t}{dz}$, because the tip displacement (dz) corresponds to the experimentally imposed z -piezo modulation. If we can ensure that the barrier height is a constant⁵, the analysis of $\frac{d \ln I_t}{dz}$ spectra focuses on how the true gap width (s) evolves with tip displacement, *i.e.*, we are interested in the functional dependence of $s = s(z)$. Figure 2.4(a) shows an example of a W-tip and a Si sample that exhibits a distinct decline in the apparent barrier height⁶ as the gap width is reduced [34]. It was found that such a behavior is characteristic for a deformation of the tunneling junction [34].

The relation between the quantities s and z can be modeled, and fit to $\frac{d \ln I_t}{dz}$ data. Following Chen and Hamers [34] (and references therein), the force acting in the tunneling junction is well described by a Morse potential ($F = -\nabla \phi$) [cp. Fig. 2.4(b)]:

$$F = -2\kappa U_e \{ \exp[-\kappa(s - s_e)] - \exp[-2\kappa(s - s_e)] \}, \quad (2.7)$$

where U_e denotes the binding energy, s_e is the equilibrium distance ($F \equiv 0$), and κ the decay length as in Eq. 2.1. If the deformation of the junction is assumed to be reversible, we can introduce an elastic constant and express small variations of the tip displacement as:

$$\delta z = \alpha F = (E^* a_0)^{-1} \approx (E_T^{-1} + E_S^{-1}) a_0^{-1} F, \quad (2.8)$$

⁵The current is found to strictly follow an exponential over several \AA tip displacement for most tip sample combinations. Close to contact, however, a dramatic reduction of the apparent barrier height will be observed [99].

⁶Figure. 2.3 also features a varying decay length and therefore also a different apparent barrier height with tip displacement. As is outlined in chapter 3, this barrier height characteristic is a remainder of a deformation of the *h*-BN layer due to an interaction with the tip.

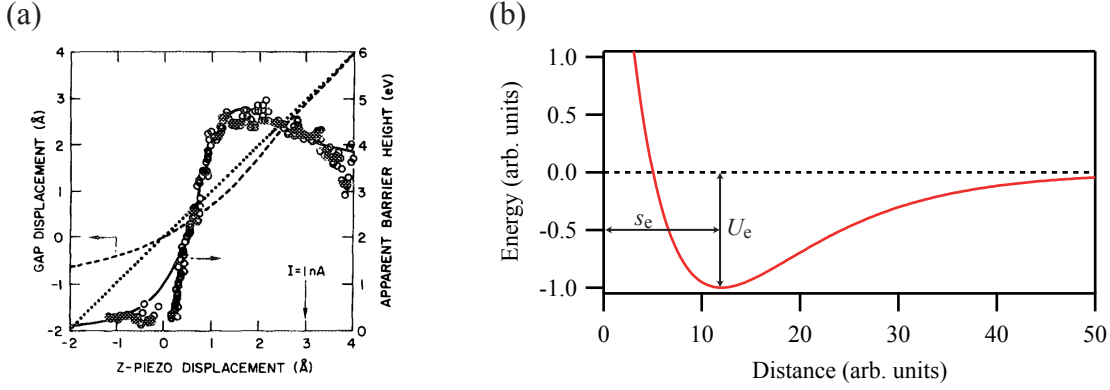


Figure 2.4: (a) The apparent barrier height varies due to forces acting between a W-tip and a Si sample that deform the tunneling junction. Figure from Ref. [34]. (b) Morse potential ϕ , where s_e corresponds to the equilibrium position and U_e to the binding energy, respectively.

where E^* is the effective Youngs modulus of the junction, which is determined by the respective moduli of tip and sample. The parameter a_0 expresses the characteristic radius of the tip apex. Summing up the elastic contribution ($\delta z = \alpha F$) and the true gap displacement (ds) we can finally relate the true and apparent gap displacement via Eqns 2.7 and 2.8:

$$\frac{dz}{ds} = 1 - \beta \{ \exp[-\kappa(s - s_e)] - 2 \exp[-2\kappa(s - s_e)] \}. \quad (2.9)$$

The parameter $\beta = 2\alpha\kappa^2 U_e$ governs the stability of the tunneling junction and expresses the tip-sample stiffness. Figure 2.4(a) demonstrates the application of this procedure and nicely shows the evolution of the true gap width with tip displacement. In chapter 3 we will present results for a *h*-BN layer that is detached from the underlying Rh substrate by a doping with transition metal adatoms, and show how the layer deflects due to an interaction with the tip.

2.2.4 STM data recording and image treatment

This is a short reminder of how STM image data was obtained and subsequently processed. All STM images presented within this contribution were recorded in the constant mode unless stated otherwise. We restricted the image treatment to an absolute minimum. The STM images of this work therefore reflect raw data without the application of any blur or other high level manipulation. The only modifications that were used, are the subtraction of a linear plane and the adjustment of contrast if judged necessary, for a better highlight in the presentation of a chosen detail. These image treatments were carried out with the software *ImageJ* [1]. The same program was used to create partial views of a region of interest and to extract the height values for line-profiles. We have furthermore used the above software to determine and to document every step of the island density analysis in order to conserve data transparency.

3 Monolayers of hexagonal boron nitride on close packed metal substrates

This chapter is designated to the principal results of this contribution and thereby outweighs the others in volume. In the following we will present a compilation of experiments that have hexagonal boron nitride (*h*-BN) supported by the surface of a close-packed transition metal in common. At first, we will outline the preparation of these atomically thin layers that are created by the catalytic action of the substrate through the pyrolysis of borazine at high temperature. Secondly, we will describe the adsorption of transition metals onto the *h*-BN layer, and indicate the calibration procedure. For the case of Ti, we will introduce the improved deposition procedure through which we were able to deposit transition metals in the cleanest fashion, since Ti adatoms showed a sizeable interaction with hydrogen. For Co, a large coverage range was explored at the temperatures of 10 and 50 K, and will be presented. The transition metal atoms of Mn, Fe, and Co showed a peculiar bistable adsorption complex whereof one state considerably weakens the *h*-BN–substrate interaction. These ring states represent the major finding of this thesis and are included in this chapter as well. The corresponding analysis for either transition metal is shown. Finally, we allude to hydrogen related issues that arose if the sample was measured at 50 K, or if the liquid helium of the cryostat was boiled off.

3.1 Growth of hexagonal boron nitride films

The preparation of atomically thin *h*-BN films is realized by the pyrolysis of precursor molecules at the catalytically active surface of a transition metal. A partial pressure of borazine [$\text{B}_3\text{H}_6\text{N}_3$, cp. Fig. 3.1(a)] is hereby introduced into the UHV system and exposed to the hot sample surface [87, 36]. The interaction with the sample tears away the hydrogen and leaves the fully dehydrogenated molecule to diffuse about the surface. When two or more of such trimmed molecules meet, they combine in order to saturate their open bonds. The tiling of many molecules finally results in a perfect two dimensional crystal lattice of hexagonal boron nitride, as is sketched in Fig. 3.1(c). As it turns out, the catalytic activity of the closed *h*-BN layer is drastically reduced compared to the one of the transition metal surface [87]. The different reaction rates entail a self-limiting growth and allow for a straightforward preparation of exactly one layer of *h*-BN. Only after largely extended borazine exposures, will a second

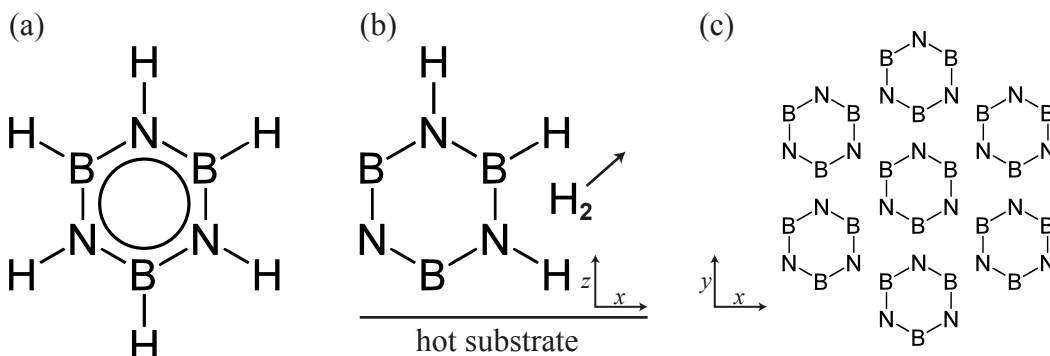


Figure 3.1: Structural formula of a borazine molecule. (a) The borazine molecule is isostructural to benzene. (b) The catalytic interaction with the hot sample surface removes hydrogen from the molecule. (c) Periodic tiling of dehydrogenated borazine that forms the layer of hexagonal boron nitride.

layer effectively be nucleated [87].

The preparation is experimentally done as follows. At first, several preceding cleaning cycles of our Rh and Ni samples are carried out by Ar^+ ion sputtering, annealing in oxygen and a finalizing flash to high temperature. The atomically clean surface is then exposed to a borazine dose of the order of 100 langmuir ($1\text{ L} = 1.33 \times 10^{-6}\text{ mbar}\cdot\text{s}$) at a sample temperature of 1040 K [36, 87]. This approach was successfully used in numerous studies to prepare *h*-BN on the close-packed surfaces of Ir(111) [107, 100], Pt(111) [88, 110, 107, 32], Ni(111) [87, 7], Rh(111) [36, 110, 107], Pd(111) [88], Ru(0001) [107, 51], Cu(111) [108], Ag(111) [85], and also on the more open surfaces of Ni(110) [53], Mo(110) [2], Pd(110) [37], and Fe(110) [139]. Note that the dehydrogenation temperature for the coinage metals was slightly lower. The growth procedure sets the standard in achieving excellent sample qualities and is routinely employed throughout this contribution. The recipe is furthermore robust to excursions in borazine exposure given the self-limiting growth properties discussed before. We note that *h*-BN can also be prepared by other means, for instance, by exposing ammonia and diborane simultaneously to a hot Ni(100) substrate [38]. Such alternative *h*-BN preparation procedures are, however, more elaborate and are not being referred to in the following.

In our case, the borazine¹ is delivered to the UHV chamber from a pressure cylinder that is permanently kept in a freezer at 250 K to avoid degradation of the molecule due to thermal decomposition. An aperture in the freezer allows to feed borazine to the leak-valve via a stainless steel tube. This gas line is always pumped with a turbo molecular pump and only filled with a borazine partial pressure minutes before the actual sample preparation is carried out. We typically expose our single crystals to a partial pressure of around $p = 1 \times 10^{-6}\text{ mbar}$ for a duration of 3 minutes. In the following sections, however, variations of this technique are also presented. We note that the growth method of *h*-BN is basically equivalent to graphene chemical vapor deposition with hydrocarbon precursor molecules without the parallel segregation

¹Advanced Delivery Chemical Systems (Austin, TX)

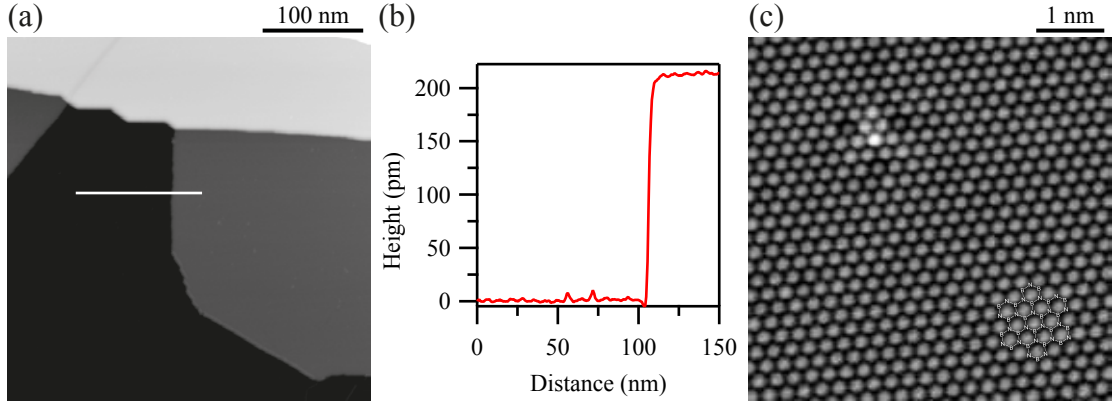


Figure 3.2: STM images of h -BN/Ni(111). (a) Overview scan showing large terraces and monoatomic steps with a height separation of about 200 pm. (b) Line profile across a step. (c) The atomic resolution illustrates the hexagonal arrangement of BN unit cells. [(a) $V_t = -200$ mV and $I_t = 20$ pA, (c) $V_t = -50$ mV and $I_t = 20$ pA.]

channel of bulk dissolved carbon impurities [cp. chapter 4].

3.1.1 h -BN/Ni(111)

In this section we focus on Ni(111) as a substrate for the growth of hexagonal boron nitride. Our interest in using this system stems from our studies of h -BN/Rh(111), where we intended to scrutinize our results for a possible hydrogen interaction [cp. section 3.2.1]. The lattice parameters of Ni ($a_{\text{Ni}} = 249.2$ pm) and h -BN ($a_{\text{BN}} = 250.4$ pm) are with $a_{\text{BN}}^{-1}(a_{\text{Ni}} - a_{\text{BN}}) = -0.5$ % very similar and thus allow the h -BN/Ni(111) system to adopt a commensurate (1×1) structure. The absence of a moiré pattern, as is otherwise frequently encountered for a variety of lattice mismatched h -BN substrate combinations, renders the height analysis of adsorbates more amenable. The system h -BN/Ni(111) was extensively studied with STM and photoemission by Auwärter [6]. He found two possible lateral arrangements of nitrogen and boron atoms with respect to the Ni atoms. These are described with respect to the Ni surface atoms by the registry (N,B) = (*top*, *fcc*) or (N,B) = (*top*, *hcp*), whereof the latter is slightly less favorable in energy [52]. There exist furthermore a strong chemical interaction between the h -BN layer and the Ni(111) substrate through a Ni $3d$ -BN π hybridization, rendering the interface metallic [109].

Our experiments are in line with the already established works as is briefly explained in the following. The Ni(111) single-crystal was cleaned in UHV by repeated cycles of Ar⁺ ion sputtering (300 K, 30 min, $10 \mu\text{A}/\text{cm}^2$, 1 kV), annealing in oxygen (815 K, 5 min, 2×10^{-7} mbar) and flash to 1100 K. Cleanliness of the Ni surface was checked with STM and the stated cleaning routine repeated if required. The single layer h -BN was prepared by exposing the sample surface held at 1040 K to a borazine partial pressure of 2×10^{-6} mbar for three minutes [36, 87]. Figure 3.2 gives an account of the sample topography after the growth of one layer h -BN/Ni(111). Large terraces are visibly separated by mono atomic steps of 200 pm

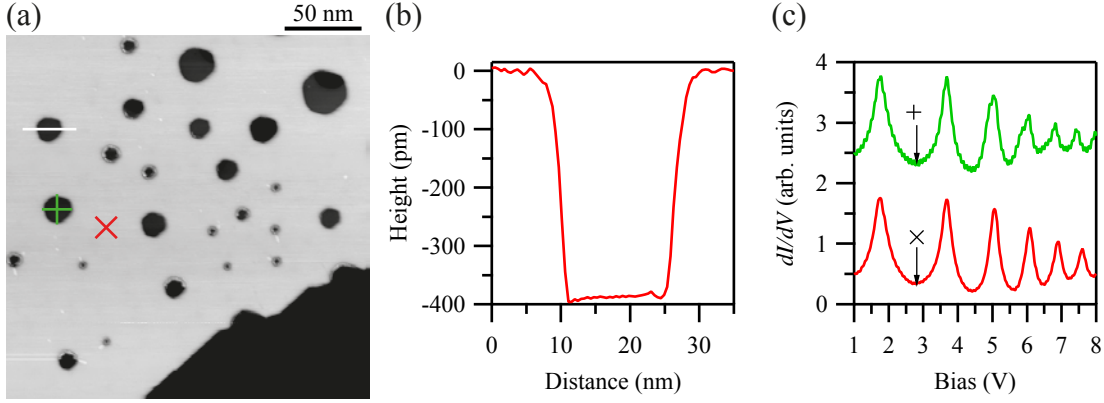


Figure 3.3: Holes in Ni substrate persist the *h*-BN growth. (a) The STM image shows sputter holes distributed about the terrace. (b) Line profile across a hole. (c) Field emission resonances (FER) show that even the holes are covered with *h*-BN. [(a) $V_t = -1$ V, $I_t = 20$ pA, and $T_{STM} = 50$ K, (c) FER spectra recorded at constant current with the parameters: $I_t = 100$ pA, $V_{mod} = 10$ mVpp, and $\nu = 1387$ Hz.]

height, which matches the value of the Ni(111) interlayer separation of 203 pm. An STM image with atomic resolution highlights the honeycomb arrangement of the BN unit cells. From this data alone, however, no conclusion whether the boron atom is situated in the *fcc* or *hcp* position can be made. The choice of the honeycomb overlay in Fig. 3.2(c) is therefore arbitrary modulo a rotation by 60° . The absence of dislocation lines that separate the two stacking regions, however, favors the phase with the boron atom located in the *fcc* position [9, 52]. Note that the enhanced resolution, despite the moderate tunneling conditions, is likely to be mediated by a hydrogen molecule trapped in the gap of the tunneling junction [131]. The corrugation of the layer in this case is (12.3 ± 0.2) pm.

Finally, we demonstrate a scenario where the Ni surface exhibits holes due to an insufficient finalizing flash in the course of the sample preparation. The sputter damage could not be healed with annealing, and therefore holes are distributed about the surface as can be inspected in Fig. 3.3. Interestingly, these holes survive the growth of the *h*-BN layer and, what is even more curious, many of the smaller holes are covered with *h*-BN. From the line profile in Fig. 3.3(b) and from the peak positions of the field emission resonances (FER) [16, 19], we recognize that two monolayer deep holes are equally covered with *h*-BN as is the remaining sample surface. With the exception of the deepest sputter holes, the *h*-BN layer thus covers the complete surface as it strictly follows the sample topography. We note that some of the shallow holes exhibit a strong noise when scanning with STM. We ascribe this to some adsorbate species that is trapped in the hole and that interacts with the electrical field of the STM tip. The latter is a further indication that the shallow hole is actually covered with *h*-BN, since adsorbates in bare Ni holes would be better trapped due to the high surface reactivity and the limited adsorbate mobility at the low temperatures employed.

The *h*-BN/Ni(111) system is extensively used in this contribution in order to scrutinize the

interplay of transition metal adatoms with hydrogen, which is described in section 3.2.1. We performed a series of test experiments, in particular with Ti adatoms, to measure how hydrogen modifies their appearance in STM images. With the help of these studies we developed a cleaning routine for our transition metal evaporation source that enabled us to prepare TM adatoms in the cleanliest fashion. The knowledge of these studies is applied to the experiments relying on TM adatoms. In the outlook of chapter 5, we furthermore discuss the properties of a hydrogen related superstructure on a *h*-BN/Ni(111) surface, and show some gold intercalation experiments.

3.1.2 *h*-BN/Rh(111)

The preparation of hexagonal boron nitride on rhodium substrates represents the most used sample configuration of this contribution. The principal results of this work were found for transition metal adatoms deposited on *h*-BN/Rh(111). Before we give an account of the sample preparation and highlight some modifications of the standard recipe, we briefly start by reviewing the characteristics of this system.

The lattice parameters of Rh (268.7 pm) and *h*-BN (250.4 pm) differ by 6.8 %. This large misfit cannot be accommodated by a stretching of the *h*-BN layer and the strain has to be resolved by some different means. It turns out that the system finds a favorable configuration for 13 BN unit cells situated on 12 Rh atoms [36]. The resulting structure is the characteristic *h*-BN/Rh(111)-(12 × 12) moiré pattern [36] with its 3.22 nm periodicity [30]. Since the surface topography resembles a honeycomb lattice, the structure is frequently referred to as nanomesh. However, it was shown not to exhibit holes but to be rather covered by a periodically rippled single layer *h*-BN [74]. In contrast to Ni(111), where the *h*-BN layer is virtually flat, the *h*-BN/Rh(111) system features a strong vertical corrugation of 1 Å [40]. Experimentally, the apparent corrugation of the moiré pattern is strongly bias dependent and it can even appear inverted at high positive bias [25]. The two regions are also characterized by an inhomogeneous bonding landscape. The first region appears in STM images as a circular depression of 2 nm diameter. This region is strongly bound due to the hybridization of the N lone pair orbital with the Rh *d*-states [110, 40]. The second region is merely weakly bound to the substrate by a van der Waals interaction [40]. This so called wire region [36] appears as a connected honeycomb network and is vertically lifted by 1 Å with respect to the hole areas [40]. The inhomogeneous binding involves a splitting of the *sp*²-derived σ and π bands by 1 eV [36, 18, 26]. Another consequence is a nonuniform charge transfer from *h*-BN to Rh [73, 40], leading to a spatial modulation of the work function [39, 54, 76] and to large lateral electric dipoles [39]. These dipoles exert electrostatic forces on polarizable adsorbates enabling the trapping of naphthalocyanine [18], of Cu-phthalocyanine [39], and of water molecules [40, 76], as well as of rare gas atoms [39, 143]. Using a Xe buffer layer technique, large Co clusters could be preferentially adsorbed in the hole regions of the moiré pattern [146].

Turning to the experimental part. The Rh(111) single-crystal was cleaned in UHV by repeated

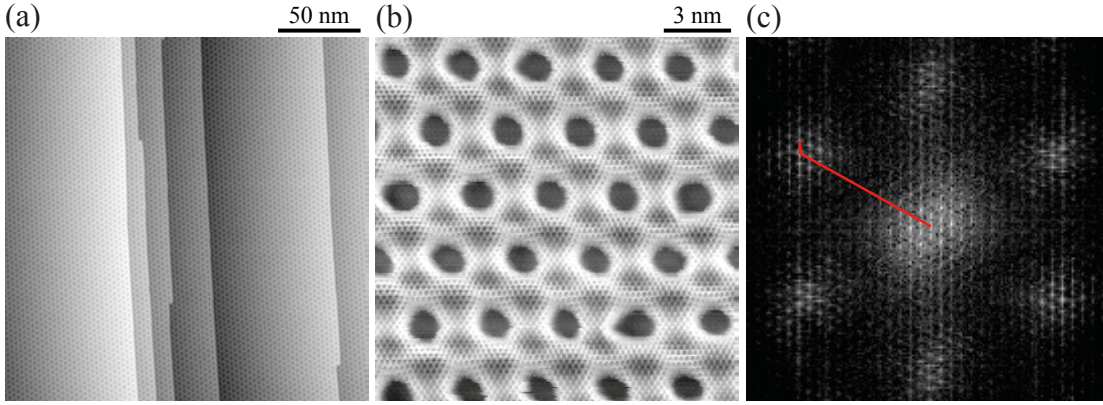


Figure 3.4: STM images of *h*-BN/Rh(111). (a) The *h*-BN layer exhibits a moiré pattern with macroscopic long range perfection. (b) Atomic resolution of the wire region and the (c) FFT image corroborating the (13×13) BN unit cells periodicity. [(a) $V_t = -1$ V, $I_t = 50$ pA, and $T_{STM} = 4.7$ K, (b) $V_t = -100$ mV and $I_t = 100$ pA.]

cycles of Ar^+ ion sputtering (300 K, 30 min, $10 \mu\text{A}/\text{cm}^2$, 1 kV), annealing in oxygen (815 K, 5 min, 2×10^{-7} mbar) and flash to 1450 K. Cleanliness of the Rh surface was checked with STM and the stated cleaning routine repeated if required. The single layer *h*-BN was prepared by exposing the sample surface held at 1040 K to a borazine partial pressure of 2×10^{-6} mbar for three minutes [36, 87].

The result of such a preparation is shown in Fig. 3.4. The beautiful moiré pattern persists with great perfection over macroscopic distances of the sample surface. It is aligned along the close-packed directions, $\langle 110 \rangle$, of the Rh substrate. A high resolution image and the concomitant FFT data [cp. Fig. 3.4(b)-(c)] corroborate the (13×13) structure, *i.e.*, 13 BN unit cells are situated on 12 Rh atom sites. Note that the STM maps the BN unit cells and not the Rh sites. Since the sample preparation readily yielded surfaces of this quality, we relied on the 3.22 nm periodicity of the moiré pattern [18] to calibrate our (x, y) -piezo scanner. All length data are therefore measured relatively to the moiré periodicity. A line profile along $[\bar{1}1]$ in Fig. 3.5(c) indicates a height difference between the wire and the hole region of about 90 pm at -100 mV bias voltage. The two different heights in the wire regions furthermore reflect the threefold symmetry of the underlying Rh^2 substrate that is transferred to the *h*-BN layer. We recall the varying degree of hybridization between the *h*-BN layer and the Rh substrate of the wire and the hole region [110, 40], *i.e.*, the height profile is a direct fingerprint of the local metal-*h*-BN attraction. A valuable mean to gauge this interaction is found from field emission resonance spectra (FER) [16, 19]. Figure 3.5(b) shows a series of FER spectra recorded at the indicated positions of the *h*-BN/Rh(111) interface. If we focus on the first resonant peak below the energy of 3 eV, we can clearly follow its evolution when moving from the strongly (1), to the weakly (5) bound regions of the *h*-BN layer. The first peak is fully quenched at the weakly bound wire regions. An interesting analogy arises from comparison with the

²Rh is an *fcc* metal and its (111) surface features two inequivalent hollow sites in contrast to, *e.g.*, Ru(0001) which is a *hcp* metal.

interfaces of h -BN/Ni(111) and h -BN/Au/Ni(111). While the first is characterized by a strong hybridization of the h -BN layer with the Ni surface [109, 108], the latter interface is expected to be dominated by an equally weak van der Waals interaction as was found for the coinage metal- h -BN interfaces of Cu(111) [108] and Ag(111) [85]. Returning to the first resonant peak in FER spectra of Fig. 3.5(b): The peak persists for the strongly bound h -BN/Ni interface, in agreement with the strongly bound region (1) of the h -BN/Rh case. In contrast, the peak is quenched for the weakly bound h -BN/Au/Ni interface, a behavior equally characterizing the van der Waals bound part of the wire region (5). The FER spectra are thus valuable in identifying the respective bonding nature of the metal- h -BN interface, and in scrutinizing whether a certain sample location is actually covered with h -BN or still terminated by the bare metal surface. The latter was extensively applied in the study of the sputter holes in the h -BN/Ni system.

We have also slightly modified the above cited growth recipe. In the following we will illustrate the resulting surface morphology and the intention why the particular recipe was chosen. The first modification is straightforward and consists simply in a reduced borazine exposure. As was discussed above, the recipe is robust to excursions to higher exposures, since the catalytic activity of the h -BN layer is negligible as compared to the one of the transition metal surface [87]. Lower exposures, on the other hand, will result in a partially covered substrate [25]. Figures 3.6(a)-(b) show an example of such a sample after the borazine dose was reduced to 15 L, and the recipe otherwise applied as usual. We find large regions with the bare Rh surface exposed and no trace of h -BN, and vice versa, large regions covered with h -BN and no sign of the Rh substrate. Figures 3.6(a)-(b) were recorded at the very boundary of such regions and confirm the coexistence of both surface terminations on the same sample.

The samples with the bare and the covered Rh substrate are essential for a precise adsorbate calibration in the study of transition metal (TM) adsorption on h -BN. For low temperature deposition of TM adatoms, we found, in the course of our experiments, an initial sticking coefficient below unity. On the bare metal substrate, on the other hand, the initial sticking coefficient is one. We therefore distinguish in the followings sections, concerning TM adatoms, between exposure and coverage. Exposure corresponds to the actually dosed amount of material, as obtained from the calibration on the bare metal substrate, whereas the sticking coefficient of the respective TM on the h -BN layer is included if we mention coverage. We note that a sticking coefficient below unity was reported for Co/ h -BN/Ni(111) [8], and in our recent contribution for Mn/ h -BN/Rh(111) [89]. More details will be presented in the respective section where the adsorption of transition metal adatoms is covered.

A second variation of the standard recipe consist in exposing the sample, held at low temperature, to a partial pressure of borazine, followed by a flash. The resulting surface shows a quite distinct topography resembling the coat pattern of a jaguar. Figure 3.6(c) demonstrates this particular sample surface resulting from a 200 L borazine exposure at room temperature and a flash to 1040 K. In contrast to the standard high temperature recipe, large areas of the bare Rh substrate remain uncovered. This behavior is rationalized by the saturation coverage of

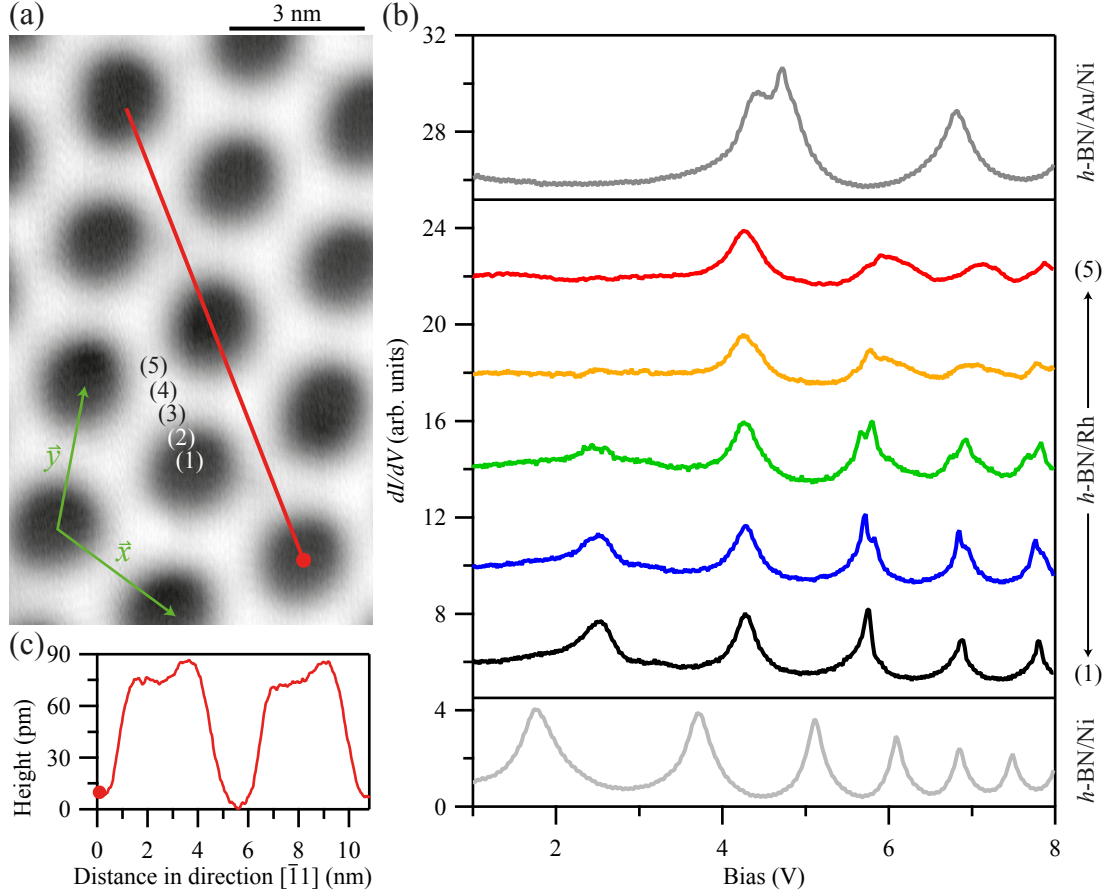


Figure 3.5: Field emission resonance spectra (FER) gauge the metal- h -BN interaction. (a) STM image indicating the positions where the respective (1)-(5) FER spectra and the height profile were recorded. The sequence (1)-(5) follows decreasing hybridization with the Rh substrate. The interfaces $h\text{-BN}/\text{Ni}$ (strongly hybridized) and $h\text{-BN}/\text{Au}/\text{Ni}$ (van der Waals) are shown for comparison. (c) Height profile along $[\bar{1}11]$ as defined by the surface vectors \vec{x} and \vec{y} . [(a) $V_t = -100$ mV and $I_t = 20$ pA, (c) FER spectra recorded at constant current with the parameters: $I_t = 100$ pA, $V_{\text{mod}} = 10$ mVpp, and $\nu = 1387$ Hz. The FER spectra were normalized with respect to the initial conductance and laterally offset by four units.]

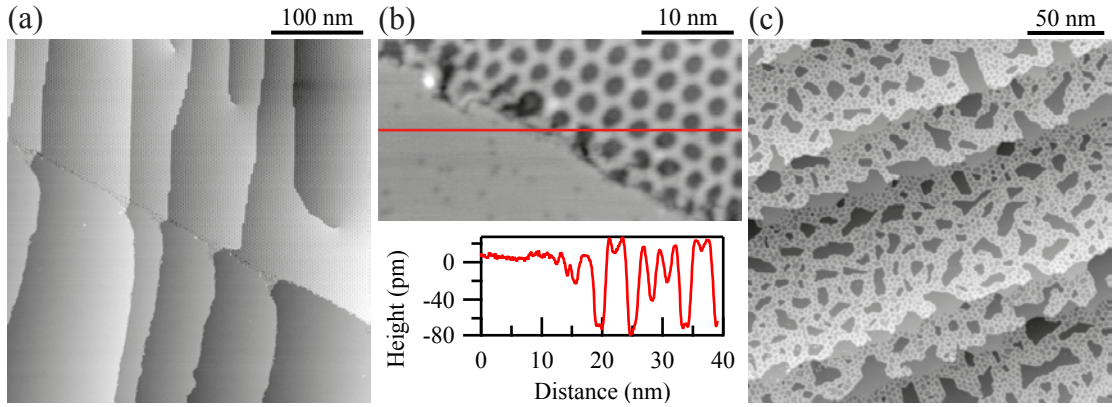


Figure 3.6: STM images of *h*-BN partially covering Rh(111). (a) Large scale STM image showing the coexistence of the bare Rh substrate and the *h*-BN layer. (b) Close inspection of the transition region with the corresponding line profile. (c) Jaguar coat like pattern resulting from the room temperature borazine exposure on Rh(111). (For all STM images $V_t = -1$ V and $I_t = 20$ pA.)

borazine molecules on a Rh(111) surface. For the analog case of ethylene exposure at room temperature, discussed in chapter 4, the saturation coverage is 25 %, whereas it is (71.4 ± 0.5) % in the present circumstance. We note that a lower dose will result in a more loosely connected *h*-BN network and that small isolated *h*-BN islands can be created with this technique. The moiré pattern formed by the method of room temperature exposure and flash shows an inhomogeneous distribution of pore sizes as can be inspected from a close-up in Fig. 3.7(a). The corresponding height histogram in Fig. 3.7(b), reveals that the aerial ratio of wire and hole regions is approximatively constant in the room temperature (red), as compared to the high temperature preparation (black). This aerial ratio is therefore a characteristic figure of how the system lowers its energy, since we recall that the hole and the wire regions reflect areas of strong and weak metal-*h*-BN interaction, respectively. The *h*-BN layer therefore accommodates the misfit strain from the (1×1) registry in the hole regions of the *h*-BN unit cells with respect to the Rh sites by a buckling away from the substrate in the wire regions. Finally, the height histogram also measures a vertical separation of the *h*-BN layer with respect to the Rh substrate of about 140 pm.

We finish by noting the intention of using the room temperature exposure and flash method. In the study of TM adatoms on *h*-BN/Rh(111), we were challenged to explain the mean size of the found TM adsorption complexes either by a high mobility at low temperature, or by an initial sticking coefficient below unity. The idea of employing the loosely connected *h*-BN regions was to obscure a hypothetical TM adatom motion across the surface by creating distinct regions, separated by the exposed Rh substrate where TM adatoms are known to be immobile at the low temperatures employed [22]. In the following sections, we will show that the mean size of the TM adsorption complexes is a consequence of an initial sticking coefficient below one.

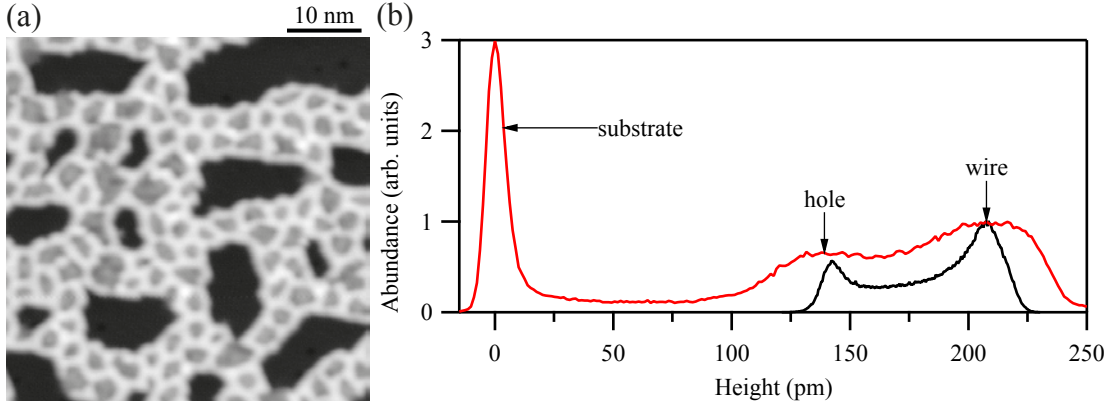


Figure 3.7: (a) STM image of *h*-BN partially covering Rh(111). (b) Height histogram of the inhomogeneous moiré pattern (red) in comparison with the regular moiré pattern of a high temperature sample (black). The histograms were normalized with the counts of the peaks at large height values, and both data sets were harvested from STM images recorded at the same bias and current setting. ($V_t = -1$ V and $I_t = 20$ pA.)

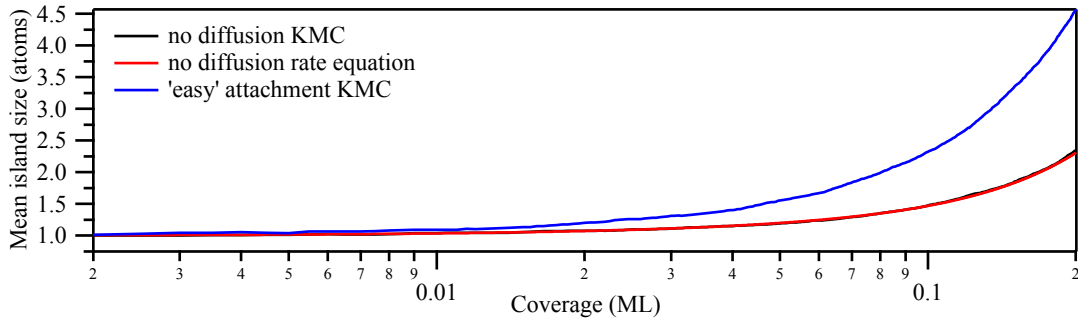


Figure 3.8: Mean island size as a function of coverage. Figure from Brune [27].

3.2 Adatom adsorption on metal supported *h*-BN

Having learned how to prepare the metal supported *h*-BN layer in the preceding section, we now turn to the deposition of adsorbates onto these samples. Ideally, the calibration of the deposition source is carried out with small adsorbate quantities on samples with no adsorbate mobility. The experimental realization is frequently given for the deposition of per mill amounts onto a bare metal surface at low temperature. Inspection of Fig. 3.8 shows the mean island size evolution with coverage for the case of a hit and stick deposition, and easy attachment [27]. Focusing on the low coverage regime, we can immediately appreciate that most of the measured islands are in fact individual adatoms. This is especially true for coverages below $\Theta \leq 0.01$ ML, where 1 ML is defined as one adsorbate adatom per substrate atom. We can therefore deduce the coverage with sufficient precision by a determination of the adatom densities on the metal substrate. Higher coverages are finally obtained from extrapolation of the calibrated flux.

In the present study, we used a thoroughly degassed electron bombardment evaporator³ and high purity transition metal (TM) rods as the material source. The exit nozzle of the evaporator is biased with a stable 12 V battery. The electrical field deviates the ionized fraction of the sublimated TM atoms to the exit capacitance, where the drain current is measured with a nanoamperemeter. This allows for a precise measurement and control of the deposition flux. A shutter finally enables a quick interruption of the atom beam. The flux calibration was carried out separately on the bare Rh(111) substrate, on Ag(100), and, in particular, on the partially *h*-BN covered Rh(111) samples at a deposition temperature of 10 K. The first two examples were employed to exclude that either substrate exhibits a high mobility for the selected adsorbate species that would obscure the calibration procedure. If a low temperature mobility was an issue, the two distinct substrate symmetries would entail a different diffusive behavior and we would observe disparate adsorbate densities [27].

The partially covered sample helped to exclude systematic deviations from one deposition cycle to the following. Since a flux calibration on the bare metal substrate, and the deposition on the *h*-BN sample need necessarily to be carried out in two separate experiments, the second exposure suffers from deviations due to fluctuations in the flux, and from the uncertainty in the exposure time. For instance, many experiments relied on per mill coverages and the exposure time was consequently short; frequently of the order of 10 seconds. Although the shutter allows for a quick interruption of the atom beam, we estimate the error of this approach to be about 10 %, which has to be added to the deviations intrinsically present due to flux fluctuations. Relying on the partially *h*-BN covered sample nullifies both uncertainties. This is true, since the deposition simultaneously populates both regions, *i.e.*, the bare and the *h*-BN terminated parts of the sample, and allows for a direct and unbiased comparison of the respective densities.

3.2.1 Ti on *h*-BN/Ni(111) and *h*-BN/Rh(111)

We start by discussing the deposition of Ti adatoms onto Ni(111) and Rh(111) supported *h*-BN. Titanium was found to exhibit a strong affinity for capturing hydrogen molecules with a strong concomitant change in its appearance in STM, as well as a dramatic shift in its electronic properties. Hydrogen can be removed from the Ti host adatom by tip manipulation. We furthermore show an improved deposition procedure in order to prepare samples with clean Ti adatoms. The new and clean deposition technique was also used in the study of the other transition metal adsorbates, in particular, our principal result obtained for manganese adatoms was scrutinized for a possible hydrogen interplay.

Figure 3.9 shows the sample after deposition of per mill amounts of Ti onto (a) Rh(111) and (b) Ni(111) supported *h*-BN at 10 K. Individual protrusions are randomly distributed about the surface. The case of the Rh(111) substrate is an example of an early experiment where, although the Ti source had been cleaned by several degassing cycles, the pressure during Ti

³Omicron EFM 3T

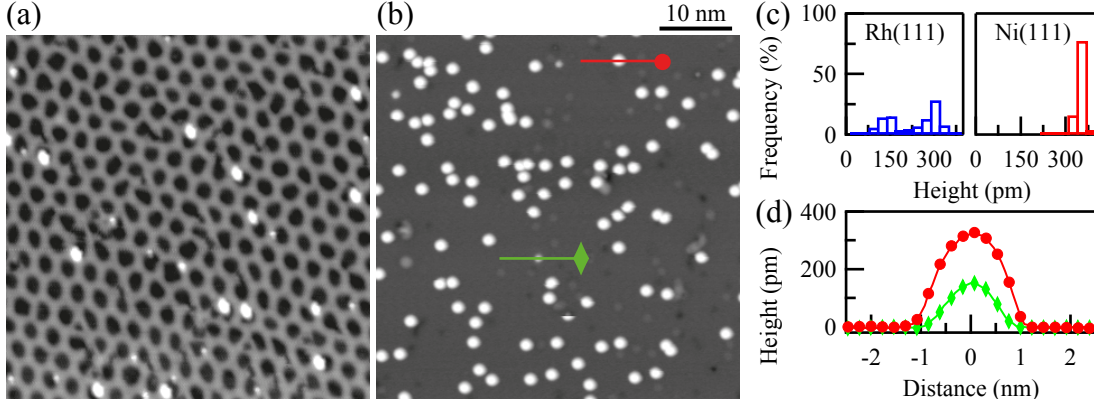


Figure 3.9: Ti deposition on Rh(111) and Ni(111) supported *h*-BN at 10 K. (a) A poorly degassed source yields two species of Ti adatoms with distinct apparent heights [$\Theta = (8.1 \pm 0.4) \times 10^{-4}$ ML]. (b) Improving the degassing routine (see text) results in a sample with almost exclusively large Ti adatoms [$\Theta = (3.4 \pm 0.1) \times 10^{-3}$ ML]. (c) An apparent height histogram shows the abundance of low and high Ti adatoms on both samples. (d) Line profile across a high (\bullet) and a low (\blacklozenge) Ti adatom. [(a) $V_t = -100$ mV and $I_t = 20$ pA, (b) $V_t = -100$ mV and $I_t = 10$ pA, $T_{STM} = 4.7$ K.]

dosing was still in the low 10^{-10} mbar and not in the usual 10^{-11} mbar range. Clearly, two species of protrusions are found located at the borders between the *h*-BN/Rh(111)-(12 \times 12) [36, 30, 74, 18, 110] moiré depressions and the wire regions [36]. The bimodal apparent height distribution of Fig. 3.9(c) reveals peaks at 150 and 300 pm. Since the depressions of the (12 \times 12) moiré pattern have been shown to readily trap and immobilize molecules [36, 18, 76, 40], rare gas atoms [39, 143], and transition metal adatoms [89], we analyze, in accordance with our previous work [89], the abundance of empty moiré unit cells in order to extract the mean cluster size per protrusion and the initial sticking coefficient.

In a first step we calibrate the deposition flux on the bare Rh(111) surface, where the initial sticking coefficient is one. With this calibration we derive a nominal coverage of $\Theta = (8.1 \pm 0.4) \times 10^{-4}$ ML for Fig. 3.9(a). This nominal coverage ought to leave the fraction $P_0 = (1 - \Theta)^n = (0.890 \pm 0.005)$ [27] of moiré unit cells with size $n = 144$ vacant. However, we observe with (0.906 ± 0.005) a slightly but significantly larger ratio of empty cells. This experimentally observed quantity of unoccupied moiré cells is obtained for a coverage of $\Theta = (6.9 \pm 0.3) \times 10^{-4}$ ML. The ratio of this real coverage to the one derived from the dose yields the initial sticking coefficient for Ti on *h*-BN/Rh(111) at 10 K of $s_0 = (0.85 \pm 0.09)$, and concomitantly a mean cluster size per protrusion of (1.05 ± 0.20) atoms in Fig. 3.9(a). We can therefore conclude that the protrusions of Fig. 3.9(a) are almost exclusively individual Ti adatoms on *h*-BN/Rh(111), and therefore the bimodal apparent height distribution is not a size effect. We note that an initial sticking coefficient below unity for transition metal adatoms on *h*-BN has previously been reported for a Rh(111) [89] and a Ni(111) [8] substrate.

By modifying the degassing routine of the Ti source one can curtail the number of low Ti adatoms to an almost negligible extent. The routine now includes, besides the thorough stan-

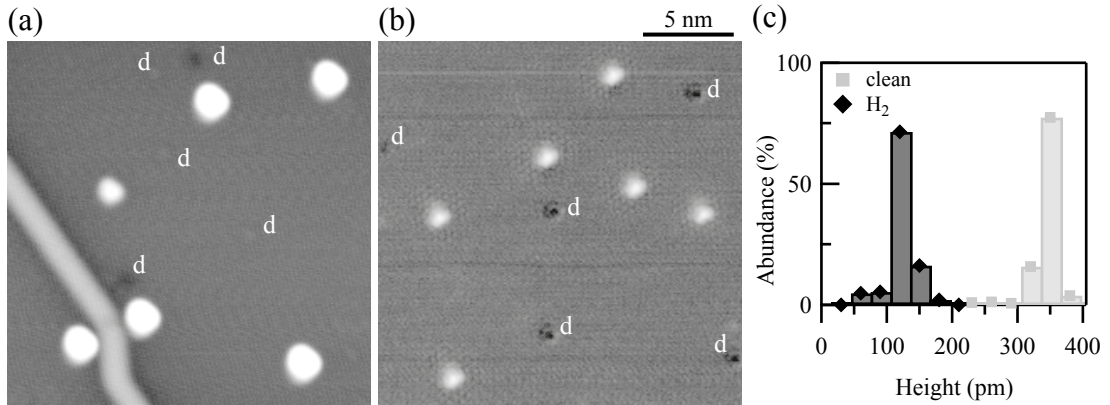


Figure 3.10: STM apparent height analysis of clean and hydrogenated Ti adatoms on *h*-BN/Ni(111). (a) Sample before hydrogen exposure. Point defects in the *h*-BN layer are labeled by the letter *d*. (b) Dosing one langmuir molecular hydrogen results in an apparent height reduction for Ti adatoms from (330 ± 16) pm to (110 ± 20) pm. (c) Superimposed apparent height histograms of the sample before and after molecular hydrogen exposure. [(a) $V_t = -100$ mV and $I_t = 10$ pA, (b) $V_t = -100$ mV, $I_t = 20$ pA, and $T_{STM} = 4.7$ K, note that a logarithmic scale was applied for the gray levels of both STM images.]

dard degassing of the evaporation material and evaporator shroud, several preliminary cycles of Ti deposition onto the closed and cooled radiation shields of the cryostat with a slightly higher flux (about 50 to 100 %) than used in the actual deposition. It was checked previously that exposing the cryostat to a directed flux of atoms or to a gas does not contaminate the sample, *i.e.*, the pressure inside the closed, and liquid helium cooled radiation shields stays well below 10^{-14} mbar [47]. The preceding deposition cycles thus clean the surface of the Ti rod without interfering with the sample. The evaporator shutter is hereby left open to guarantee that the desorbing gas is not trapped but effectively pumped from the evaporator. This approach finally creates a clean environment necessary for the shortly following actual deposition. For the actual Ti dosing the cryostat's shields are rotated so that a small aperture opens in the line-of-sight between evaporator and sample. The effect of this degassing routine is seen from inspection of Fig. 3.9(b), where the majority of Ti adatoms are now in their high (\bullet), and only 2 % are in their low apparent height state (\blacklozenge). This degassing routine has finally enabled us to dose from all transition metal sources in the cleanest fashion.

We have just ascertained that the bimodal apparent height distribution of Ti adatoms is not a size effect. It might therefore originate from a co-adsorption of, and interaction with, residual gas molecules. A potential candidate is hydrogen, which is the prevailing residual gas in common UHV systems. The inspection of the Ti adatom population after a deliberate exposure to a partial pressure of molecular hydrogen proves this hypothesis⁴. The effect of this exposure is presented in Fig. 3.10 and reflects the situation before and after dosing 1 L hydrogen at 10 K. An apparent height histogram in Fig. 3.10(c) clearly shows the abundance shift towards the

⁴The UHV chamber is backfilled with molecular hydrogen which can enter the cryostat volume through the therefore opened aperture.

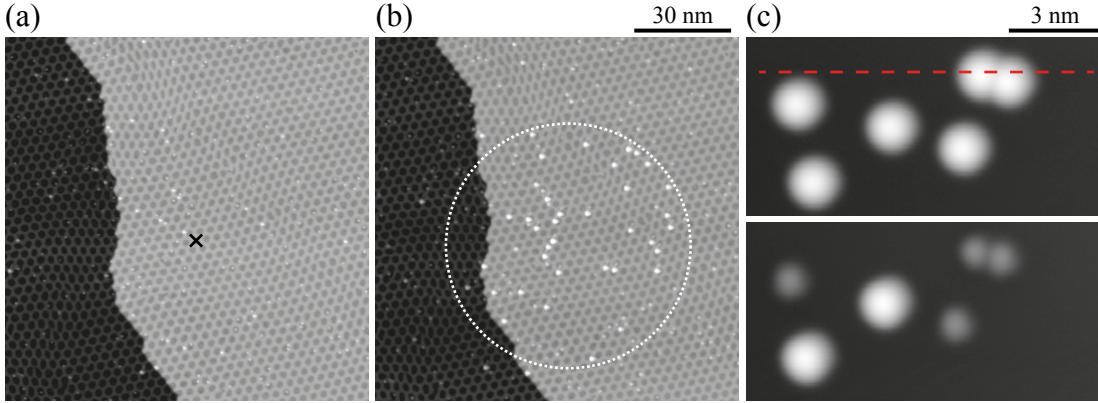


Figure 3.11: (a)-(b) Transformation of an ensemble of Ti adatoms from their low to their high apparent height state by a bias pulse of +4 V applied at the indicated position (\times). STM image (a) before and (b) after bias pulse. (c) Transformation of Ti adatoms in the high state (top) into the low state (bottom) by a 5 nA current linescan at the indicated location (dashed line). [$V_t = -100$ mV, $I_t = 20$ pA, and $\Theta = (1.36 \pm 0.06) \times 10^{-3}$ ML.]

low state as the height drops from (330 ± 16) to (110 ± 20) pm. A comparison with Fig. 3.9(c) shows the perfect matching of the two peak values to the case of a Ti adatom dosed from a commonly degassed source, and where both adatom species were numerous. We can therefore conclude that the high and low states are characteristic of clean and hydrogenated Ti adatoms, respectively. Interestingly, we also note the defect line [9] and point defects (d) of the h -BN layer in Fig. 3.10. The latter show a marked contrast inversion once the sample had been exposed to hydrogen. This might indicate that hydrogen also interacts at defect sites with the sample. The observed phenomena of the present contribution can finally be linked to a hydrogen interplay and we will interpret the experimental observations accordingly. In the following, we will use clean and high apparent height Ti adatoms synonymously, as well as low apparent height state and hydrogenated Ti adatoms.

There is a close connection between both Ti adatom species and we are able to transform a hydrogenated into a clean Ti adatom via tip manipulation. A sample with a majority of hydrogenated Ti adatoms is shown in Fig. 3.11(a). A bias pulse of +4 V with open feedback-loop transformed virtually all Ti adatoms located within a radius of 38 nm from the tip location where the pulse had been applied (\times) from the low into the high apparent height state. The larger the bias the larger the transition region. Radii of 70 nm and more were observed. In rare cases high Ti adatoms could be switched back into their low state by tip manipulation. However, this succeeded only on samples where already some hydrogenated Ti adatoms were discernible. If so, a line scan across a high Ti adatom at small tunneling resistance ($R_g = 2 \times 10^7 \Omega$) may result in a sudden drop of its apparent height to about 110 pm as can be seen in the example of Fig. 3.11(c).

In addition to the apparent height variation, the two states of the Ti atoms distinguish themselves in their differential conductance (dI/dV). Figure 3.12 shows that the STS signal of

a clean Ti adatom is basically featureless whereas the hydrogenated Ti adatom exhibits a distinct zero-bias resonance with a conductance increase of 100 %. A voltage pulse (+1.2 V, feedback-loop open) on this adatom switches it into its high state and concomitantly resets the differential conductance to the featureless one characterizing the clean Ti adatom, as can be inspected in Figs 3.12(c)-(d). The peak at the Fermi energy is attributed to a Kondo feature [61, 77]. Below the Kondo temperature (T_K), the magnetic moment of a localized magnetic impurity is screened collectively by the surrounding conduction electrons [61, 77]. The Kondo feature arises from the interference of electrons tunneling directly into this impurity state with electrons tunneling into the continuum, and can be modeled by a Fano function: [43, 77, 86]

$$\frac{dI}{dV}(V) \propto \frac{(q + \epsilon')^2}{1 + \epsilon'^2}, \epsilon' = \frac{eV - \epsilon_0}{\Gamma}. \quad (3.1)$$

The parameter Γ describes the half-width of the resonance at half-maximum (HWHM), q measures the ratio of direct tunneling into the impurity versus tunneling into the continuum, and ϵ_0 marks the position of the impurity state with respect to the Fermi level [43, 77, 78, 86]. The recorded dI/dV curve was reproduced by iteratively adjusting the Fano line-shape parameters and subsequent convolution with the function of thermal and modulation broadening [70, 106]. The sample and tip temperature were hereby assumed to be equal to 4.7 K. The result of this procedure is shown as full black line in Fig. 3.12(c). It is in excellent agreement⁵ with data, and yields $\Gamma = (2.8 \pm 0.2)$ meV and $q = (4.15 \pm 0.05)$. From these parameters we ultimately extract the intrinsic Kondo temperature of $T_K = (29 \pm 3)$ K, through $\Gamma = \sqrt{(\pi k_B T)^2 + (k_B T_K)^2}$ [86, 101], where T is the sample temperature of 4.7 K, and k_B the Boltzmann constant⁶.

As we have deduced before, we may attribute the low Ti adatom as being in contact with hydrogen. The questions remains as to whether the hydrogen is molecularly attached or dissociated. The available d holes in transition metals mediate hydrogen dissociation by a suppression or a significant reduction of the activation barrier [60]. Furthermore, it was found that the dissociation ability of a transition metal surface is seriously enhanced if step and defect densities are increased [35]. In the extreme of isolated transition metal atoms, *e.g.*, for Ni atoms, it was concluded that hydrogen attachment advances via a charge transfer from the TM host to the anti-bonding states of the molecule, which will increase the H – H separation and ultimately lead to its dissociation [67, 96]. In this sense, the present Ti adatoms and point defects constitute ideal active sites for hydrogen dissociation. One can thus view the hydrogen molecule as being dissociated at the Ti host adatom. Hitherto, the maximum amount of hydrogen per Ti host adatom remains unknown, however, we note that a close inspection of the height distribution [using a smaller bin size as opposed to Fig. 3.10(c)] reveals two peaks at

⁵The error was determined by manually varying the simulation parameters until the agreement with the measured conductance significantly worsened.

⁶The above formula is expressed for HWHM and the factor α from Ref. [101] is not obtained from a fit of the peak width evolution for different temperatures, but set equal to 2π , in agreement with Ref. [86]. We note that applying a magnetic field should result in a splitting [61, 101], and increasing the temperature in a broadening [86, 101] of the resonant peak. To test for this behavior, however, is beyond the scope of our experimental apparatus.

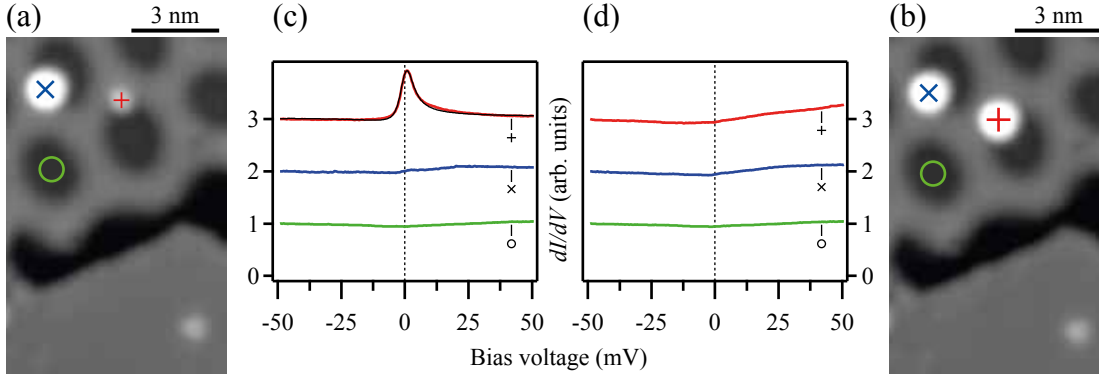


Figure 3.12: STM images (a) before and (b) after transformation of a low into a high Ti adatom via tip manipulation [+1.2 V pulse next to low Ti adatom (+), feedback-loop open]. (c) The hydrogenated (low) Ti adatom exhibits a Kondo feature in differential conductance (dI/dV) which is (d) absent for the clean Ti adatom. The full black line in (c) shows a Fano function yielding $T_K = (29.0 \pm 2.6)$ K. [$V_t = -100$ mV, $I_t = 20$ pA, setpoint before opening the feedback-loop: $V_t = -50$ mV and $I_t = 200$ pA. The spectra are normalized with the conductance at -50 mV and vertically offset by one unit.]

the low height values, one centered at 110 and the other at 150 pm. This may be a signature of a varying hydrogen occupation.

The conversion of high into low Ti adatoms and vice versa is interpreted as the attachment and removal of hydrogen to and from the Ti host adatom, respectively. A voltage pulse therefore cleans a Ti adatom by removing hydrogen. Although the transformation scheme is qualitatively equivalent to a charging, *e.g.*, as shown for NaCl supported Au adatoms by electron injection [113], it should not be confused with the latter. It shares, however, resemblance with the non-local dissociation of molecules reported in Ref. [79]. Such a large spatial liberation of hydrogen by the electrical field of an electrode could have ramifications in hydrogen storage applications. The inverted process of attaching hydrogen to Ti adatoms at low tunneling resistance was observed as well [cp. Fig. 3.11(c)]. We rationalize this transformation with a hydrogen molecule that is confined in the gap of the tunneling junction [131] and dragged from the neighborhood toward the Ti adatom.

We finish this section by stressing how this study relates to other experimental results. First of all, the strong affinity of Ti adatoms for capturing hydrogen has risen our awareness that hydrogen may act as an interfering agent in our UHV system. It has furthermore led to the implementation of the improved deposition routine described above, through which the other experiments of this contribution were scrutinized for a possible hydrogen interference. We note that physisorbed hydrogen has an almost negligible activation barrier for diffusion on the *h*-BN surface. The ramification of this high mobility is that hydrogen molecules will always find an impurity site to which they may attach, *i.e.*, in the worst case the adsorbate we intend to study. There are important consequences of this fact: A co-adsorption of even the smallest amounts of hydrogen at low temperature, will always result in a hydrogenation of

the adsorbate, irrespective of where the adsorbate or the hydrogen molecule initially adsorbs. This stresses the importance of preparing samples in the cleanliest fashion, in particular, for non local studies which average over a comparatively large surface area, and therefore over a great ensemble of adsorbates. Given the similar properties of graphene, these consequences may equally apply to samples that are covered by this carbon layer⁷. Since the mobility of hydrogen is comparatively limited on the bare metal surface⁸, we propose the preparation of a partially covered *h*-BN sample to circumvent the hydrogen diffusion issue. Recalling that we can create separated *h*-BN islands by the room temperature adsorption of borazine, a distribution of *h*-BN islands could be grown that is separated by the exposed metal substrate. In consequence, hydrogen molecules that adsorb on the metal substrate or an island cannot reach another island and leave therein located adsorbates untouched. Such separated islands were readily created for graphene by the room temperature adsorption of ethylene and subsequent dehydrogenation, as is outlined in chapter 4. Note that a sample with separated island would only alleviate the diffusion problem but not prevent co-adsorption of hydrogen coming from the residual pressure. We will address the issue of such a hydrogen co-adsorption in UHV for a sample surface held at 50 K in section 3.3.

3.2.2 Mn, Fe and Co on *h*-BN/Rh(111)

The transition metals Mn, Fe, and Co are bundled together into this section since they were found to exhibit an equivalent behavior, responsible for the main results of this contribution. We will explore how a dosing of small amounts of the latter elements can influence the bonding of the *h*-BN layer to the underlying metal substrate. It is shown that one single adatom can effectively detach the *h*-BN layer from the substrate. The so weakened layer then behaves as a soft membrane that is deformed in the presence of the tip due to tip-sample interactions competing with the *h*-BN-substrate forces. The first part of this section is dedicated to clarify experimental findings in order to understand the conclusion of the *h*-BN-substrate weakening. We therefore have to rationalize the number of atoms per adsorption complex, discuss the influence of the sticking coefficient, and demonstrate the impact of the scanning tip on the measured island densities. These factors are best exemplified for the case of cobalt, given that all essential experiments were carried out with this element. The findings also apply to iron and manganese. Later we will focus, however, on manganese, since Mn turns out to be the most robust adsorbate with respect to the bias of the scanning tunneling microscope.

Co/*h*-BN/Rh(111)

The STM image series of Fig. 3.13(a) shows the distribution of cobalt, deposited at 10 K, as a function of exposure. The exposure was iteratively increased and every deposition step investigated with STM. The partially *h*-BN covered sample carried the precise flux calibration. We determined the Co island densities on the *h*-BN covered and on the Rh exposed parts

⁷Our colleagues F. Donati and Q. Dubout encountered similar problems in their study of Co/g/Pt(111).

⁸The migration barrier for hydrogen on Rh(111) is of the order of 40 meV [117].

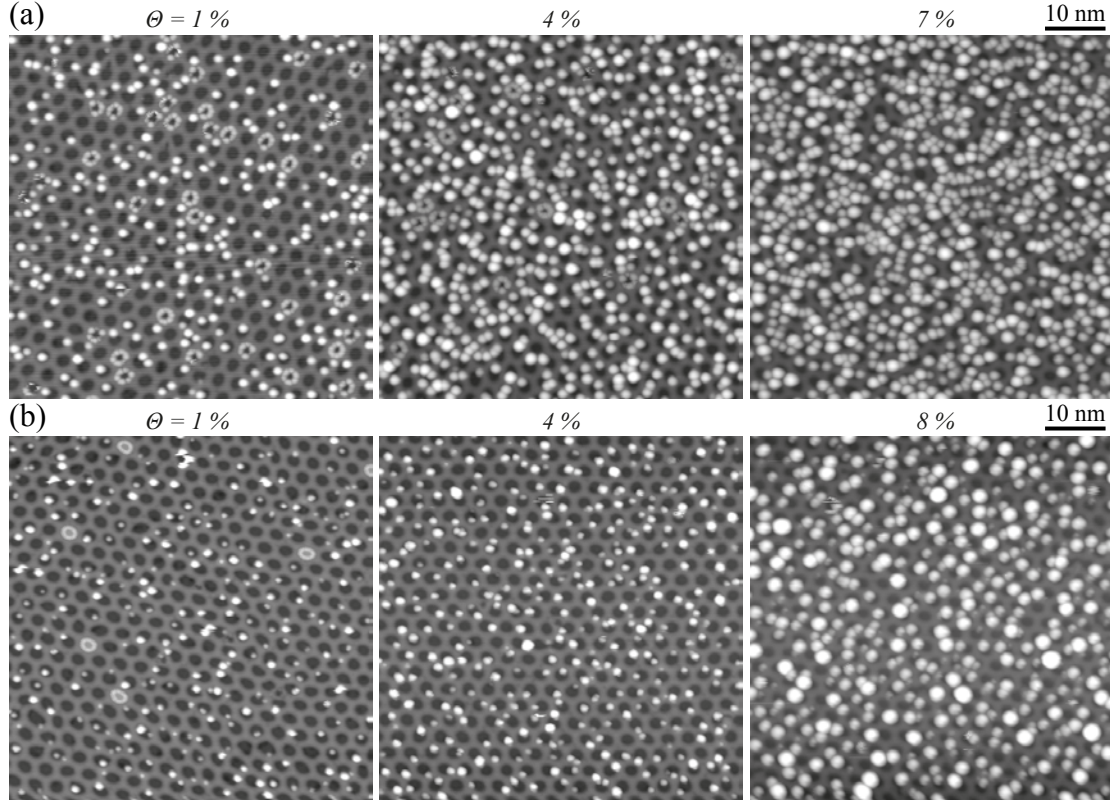


Figure 3.13: Deposition of Co/*h*-BN/Rh(111) for an exposure of (a) 0.009, 0.036, and 0.072 ML at 10K, and for an exposure of (b) 0.01, 0.04, and 0.078 ML at 50K. ($V_t = -100$ mV and $I_t = 10$ pA).

of the sample. The latter densities were compared to the initial exposure at low densities and scrutinized whether the extrapolation would correctly match the long exposure. We furthermore ensured that the deposition of the full amount of cobalt in one step yielded comparable densities as did the stepwise approach. The circular structures that can be seen in (a) constitute a bistable adsorption complex. The properties of these rings will be elucidated in section 3.2.3. The rings are taken into account in the analysis of island densities and count equally as do the other islands⁹. For the time being, we will focus on the Co island evolution as a function of exposure. The same procedure was carried out for a Co deposition at 50 K as is shown in the sequence of Fig. 3.13(b).

We have realized a large number of the mentioned cobalt deposition experiments to obtain a stable statistical insight into the adsorption behavior. The data is presented in Fig. 3.14 and (a) shows the mean Co island size evolution for two deposition temperatures of 10 and 50 K. The mean island size is derived from the Co island densities on the *h*-BN layer and on the bare Rh

⁹A surface area with rings (N_R) and Co islands (N_I) will be considered in the data analysis by the sum of both populations ($N_T = N_R + N_I$).

substrate. We calculate the mean Co island size as:

$$\langle s \rangle = \frac{\Theta_{\text{Rh}}}{\Theta_{\text{BN}}}, \quad (3.2)$$

and plot the latter as a function of exposure. Note that every data point was calculated with the mean value of several STM images and the error bars denote the standard error of the respective mean (σ/\sqrt{N}). From an extrapolation to zero exposure, we can immediately appreciate that the mean island size of $\langle s(\Theta \rightarrow 0) \rangle = (1.21 \pm 0.04)$ atoms is larger than one, but clearly less than two. In the zero exposure limit, however, mobile adsorbates should tend to larger mean island sizes values, and immobile adsorbates ought to exhibit a mean island size of one. We resolve the discrepancy by formally introducing an initial sticking coefficient

$$s_0 = \lim_{\Theta \rightarrow 0} \frac{1}{\langle s(\Theta) \rangle}. \quad (3.3)$$

The mean island size of one at zero exposure is finally found if an initial sticking coefficient for Co/*h*-BN/Rh(111) of $s_0^{\text{Co}} = (0.83 \pm 0.04)$ is assumed. We note that the method described for Ti adatoms at the beginning of this section is deduced from an independent argument, and yields a result of the same order [$s_0^{\text{Ti}} = (0.85 \pm 0.09)$]. These values join the ranks of the already established sticking coefficients below unity, *i.e.*, for Co/*h*-BN/Ni(111) [8] and Mn/*h*-BN/Rh(111) [89]. The many parallels of *h*-BN to graphene presumably entail a similar adatom sticking behavior with coefficients below unity. It would be worthwhile to determine the sticking coefficient for other TM-*h*-BN and graphene combinations. We also note that omitting the sticking coefficient in the data analysis may have a sizeable influence on derived physical quantities. For instance, the mean island size naturally deviates by the value of the sticking coefficient. We have respected the latter for Co in the presentation of our data at 10 and 50 K in Fig. 3.14(b). For the mean island size we write:

$$\langle s \rangle = s_0 \frac{\Theta_{\text{Rh}}}{\Theta_{\text{BN}}}. \quad (3.4)$$

The coverage is brought into relation with the sticking coefficient by:

$$\Theta = s_0 \Theta_{\text{Rh}} \quad (3.5)$$

We have also included the 200 K Co deposition series on *h*-BN/Rh(111) in the graph of Fig. 3.14(b), carried out by Bulushek [29]. Please note that the error bars of the latter represent the standard deviation and not the standard error of the mean. A binomial distribution (green) describes the expected Co island size evolution and is also added to Fig. 3.14. It is calculated via [27]:

$$\begin{aligned} \langle s \rangle &= \sum_{k=1}^{\infty} k \cdot P_k / (1 - P_0) \\ P_k &= \binom{n}{k} \Theta^k (1 - \Theta)^{n-k}, \end{aligned} \quad (3.6)$$

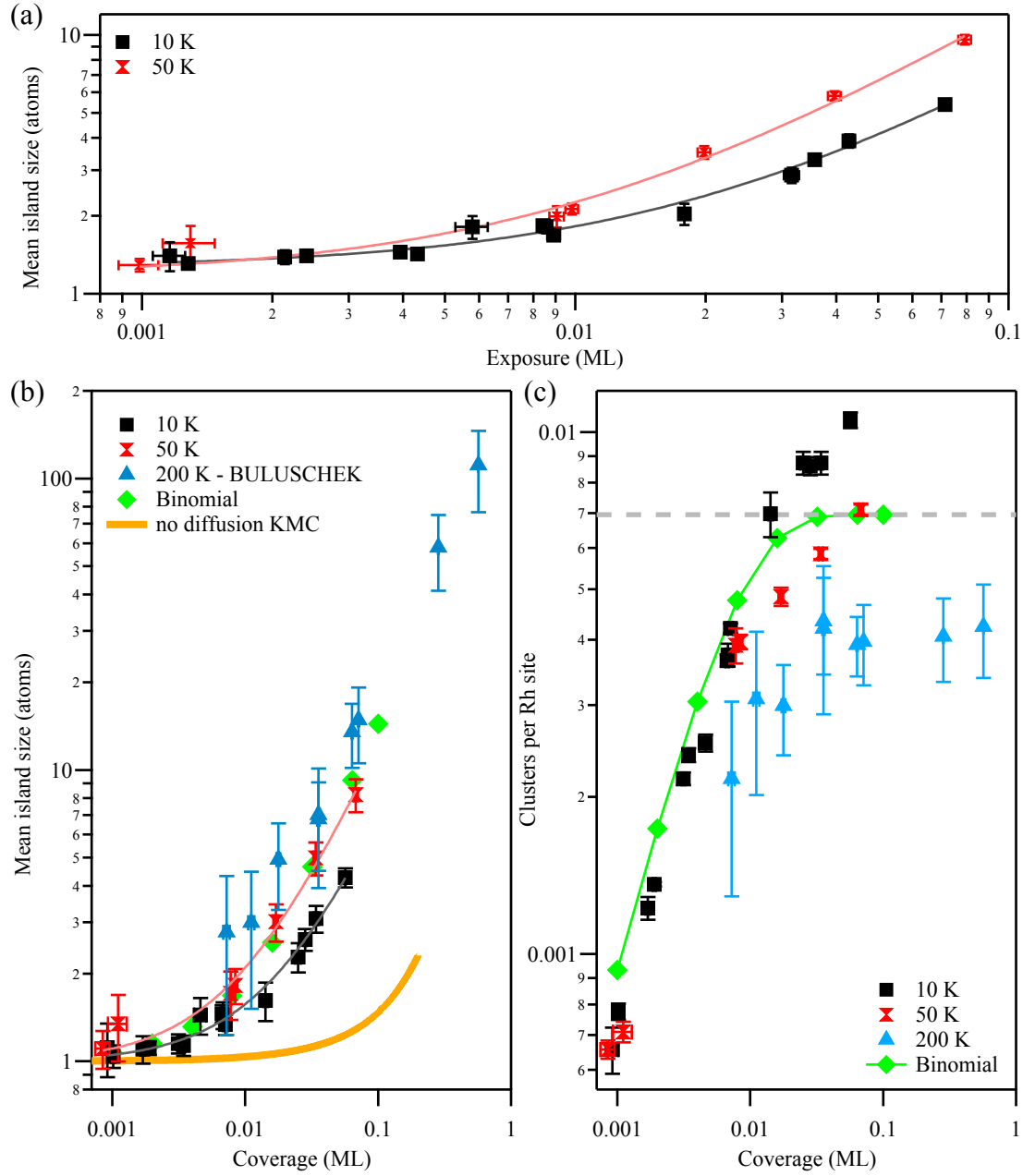


Figure 3.14: Summary of Co deposition on *h*-BN/Rh(111) for varying coverage. (a) The initial sticking coefficient for Co on *h*-BN/Rh(111) is deduced from the extrapolation of the mean island size to zero exposure and is applied in the following to the data presented in (b) and (c). (b) The mean island size for Co deposited at 50 K is equal to the calculated mean size for a binomial distribution. The evolution for statistical growth (orange) [27] and the data from Buluscek (blue) [29] are shown for comparison. We have corrected the latter data with the initial sticking coefficient. (c) Co island density per Rh site in dependence of coverage. The dashed line marks the density of one island per moiré unit cell. Note the distinction between exposure and coverage. The error bars of the Buluscek data correspond to the standard deviation.

where $n = 12 \times 12$ denotes the cell size, k the cell occupation, and Θ the coverage, respectively. We note that the close relation of the above binomial to the Poisson distribution for the present cell size, allows to conveniently express the mean island size in closed form as:

$$\begin{aligned} \langle s \rangle &= n\Theta (1 - \exp\{-n\Theta\})^{-1} \\ P_k &= \exp(-n\Theta) (n\Theta)^k / k!, \end{aligned} \quad (3.7)$$

Finally, the mean island size for a statistical growth without mobility (orange) is appended for comparison to Fig. 3.14(b) [27].

The Co island size evolution in Fig. 3.14(b) is characteristic for a distinct adsorbate diffusion on the inhomogeneous *h*-BN/Rh(111)-(12 × 12) moiré topography. Figure 3.14(c) is a different representation of the Co island data. Therein we plot the Co island densities ($\rho = \Theta / \langle s \rangle$) as a function of coverage. The green curve illustrates the calculated Co island density that allows to occupy the (12 × 12) moiré unit cell by maximally one Co island. At coverages of 2 % and above, one can view the curve as the threshold separating three different diffusion regimes. The measured mean Co island size evolution for the temperatures of 10, 50, and 200 K represent examples of these three regimes. For the case of 10 K, the island density is higher than one island per (12 × 12) moiré unit cell. It matches exactly one island per cell for a Co deposition at 50 K, and it is lower than one per cell for Co dosed at 200 K. We interpret this behavior as follows. For the case of low temperature, the inter cell diffusion is prohibited and Co adatoms cannot traverse the wire region and interact with neighboring Co adatoms. The intra cell diffusion, however, is allowed but slow, since we find several islands per moiré unit cell, but less than would be expected with no adatom mobility, *i.e.*, for the statistical growth of Fig. 3.8. At 50 K, on the other hand, the intra cell diffusion is sufficiently high that all Co adatoms within the same moiré unit cell nucleate into the same island but still no Co adatom can cross the wire region to combine with neighboring Co islands. Finally, at 200 K and the concomitant high Co adatom mobility, all present barriers can be overcome, including the ones of the wire region. We have to remark that only a negligible number of Co adatoms is found on the wires of the moiré pattern¹⁰. The absence of Co adatoms on the wire cannot be rationalized by the initial sticking coefficient, since the wires have an aerial ratio of about 70 %. A Co adatom arriving from the vapor phase and hitting a wire site has to execute some final hops in order to end up in the hole. The corresponding migration barrier for Co adatoms on the wire must be small and well below 20 meV¹¹. Two principal barriers finally describe the nucleation behavior of Co/*h*-BN/Rh(111) for the temperatures beyond 10 K. The first is the intra cell migration barrier of order $20 \leq E_M \leq 30$ meV, governing the low temperature nucleation, and responsible for Co island densities larger than one per moiré unit cell. The second barrier of order $E_{IC} \geq 120$ meV intervenes in the nucleation as it prevents the inter cell diffusion of Co adatoms.

The Arrhenius plot in Fig. 3.15(a) shows the logarithm of the island densities for a coverage of 0.07 ML in dependence of the inverse temperature in the interval of 10 to 500 K. Typically, the

¹⁰ The Co adatoms that are found on the wire regions are presumably pinned to point defects in the *h*-BN layer.

¹¹ $E_M = -k_B T \ln(1/\nu_0)$, with $T \leq 10$ K.

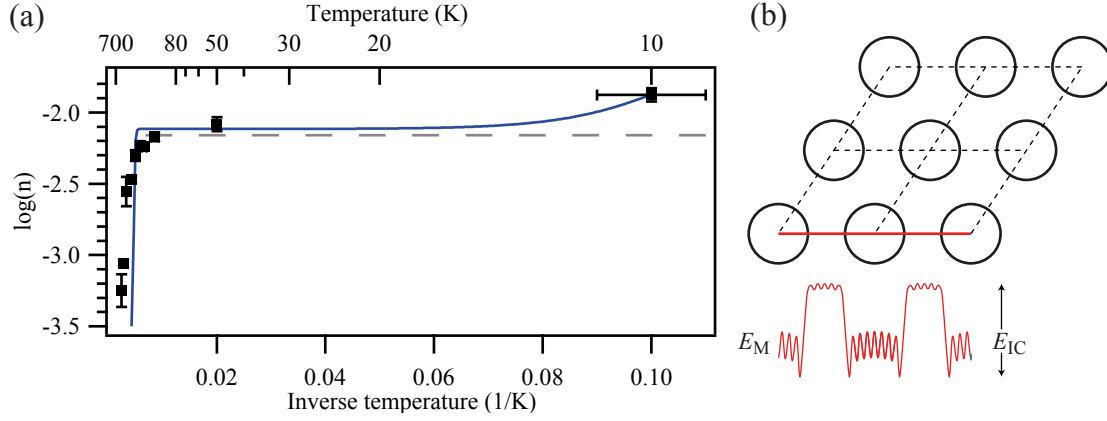


Figure 3.15: (a) Arrhenius representation of Co island densities on *h*-BN/Rh(111) for a coverage of 7 % as a function of inverse temperature. The two low temperature data points at 10 and 50 K were added in this contribution, the remaining data is from Bulushek [29]. The dashed line corresponds to the one island per (12×12) unit cell threshold and the blue line results from an inadequate rate equation description. (b) Energy profile across the moiré unit cell.

migration barrier and the attempt frequency can be extracted from such a data representation for saturation island densities on a homogeneous substrate by a linear fit. The migration barrier corresponds to the slope, and the attempt frequency to the infinite temperature intercept of the linear fit. Bulushek [29] derived a migration barrier of 23 meV for Co/*h*-BN/Rh(111), and he furthermore pointed out a significant quenching of the attempt frequency to a physically unlikely low rate of 10^5 Hz. The reduction of the attempt frequency is commonly encountered for confined diffusion on inhomogeneous substrates and was first presented in the prominent example of Ag diffusion on the (25×25) dislocation network formed by 2 ML Ag/Pt(111) [28]. The Co island densities for temperatures above 117 K are from Bulushek [29], and the data points at 10 and 50 K were added in this contribution to the Arrhenius plot. The trend from high temperature data is visibly not respected when the temperature is lowered to 117 K and below. The island density flattens out and becomes less temperature dependent in the interval of 10 to 50 K. The slope of a hypothetic linear fit at the latter temperature interval would yield a migration barrier of only 2 meV. A preliminary attempt to describe the nucleation behavior by rate equations¹² yielded $E_M = 25$ meV and $E_{IC} = 600$ meV and is shown as a blue curve in Fig. 3.15(a). We decided not to highlight these values since the model was found to be inadequate¹³. The most appropriate approach describing the nucleation behavior of Co on *h*-BN/Rh(111) would be the implementation of a kinetic Monte-Carlo (KMC) simulation in order to refine the above estimated migration barriers¹⁴. The execution of such a KMC

¹²See for instance Venables *et al.* [137] and references therein.

¹³The model deposits the fraction of adatoms landing on wire sites into the holes of new moiré cells and thereby simulates the binomial distribution. The remaining fraction of adatoms landing in the hole regions serve as a correction reservoir that augments the island density at low temperature, and suppresses the island density for high temperatures. Only the two mentioned barriers were included. No high order processes like monomer diffusion or desorption were considered. Desorption and diffusion up to the pentamer were accounted for by Bulushek [29].

¹⁴The energy profile sketched in Fig. 3.15(b) is very similar to the adsorption landscape proposed by Widmer *et*

routine uniquely dedicated to the (12×12) moiré pattern would constitute a good starting point. Given the adatom denuded wire zones, due to thereon negligible migration barriers, the structure could be renormalized to a size emulating the wire to hole areal ratio. Instead of using the (12×12) unit cell, the simulation could be carried out with a box of size (7×7) . The effective coverage would then be increased by the factor $144/49$. The realization of such a KMC simulation is at this point, however, beyond the scope of this contribution.

Table 3.1: Wipe factor reducing the Co island densities when scanning with the tip at $V_t = -1$ V and $I_t = 10$ pA. Note that multiple scans will further decrease the island density.

Coverage (ML)	10 K	50 K
0.009	1.46	1.26
0.018	1.39	1.21
0.036	1.45	1.16
0.072	1.43	1.12

We finish this section by describing one final aspect in the study of Co island densities on *h*-BN/Rh(111). In the course of our experiments we observed that the tip modified the measured Co island densities while scanning, in particular at elevated bias. To exemplify this impact, the island densities were determined for different coverage before and after scanning the same surface region at $V_t = -1$ V and $I_t = 10$ pA. For the case of low coverage, the island density is reduced by a factor of 1.46 at 10 K, and by 1.26 at 50 K. Table 3.1 summarizes the influence of the bias voltage on the Co island densities. It is seen that at higher temperatures and coverage the impact of the tip-sample interaction is reduced. This can be rationalized by the fact that Co islands are larger at 50 K than they are for Co deposited at 10 K [cp. Fig. 3.14(b)]. The modification of the observed densities is, however, striking and we note that a second scan at the high bias will continue to falsify the measured densities. We have empirically optimized the scanning parameters to avoid a sample modification by the tip, and we obtain stable conditions for $V_t = -100$ mV and $I_t = 10$ pA. At the beginning of our study, we were oblivious of this bias influence and recorded the Co island densities at $V_t = -1$ V and $I_t = 5$ pA. We therefore had to repeat the experiments. The consideration of the wipe factor and the initial sticking coefficient in the representation of the erroneously obtained data, reconciles the measurements to the above results. They are, however, not included in this contribution. Both, the tip-sample interaction as well as the effect of the initial sticking coefficient compensate another to some extent. Nonetheless, we stress the importance of scrutinizing the measured densities for a possible tip-sample interaction and to properly characterize the sticking behavior in order to correctly describe the physical process under study. A final note concerning the parameter tuning in the search for gentle scanning conditions is that it has lead to the discovery of the initially mentioned rings. These rings deserve a closer focus and are therefore the topic of the next section.

al. [143] for Xe adatoms on *h*-BN/Rh(111).

3.2.3 Ring state for Mn, Fe and Co adatoms

This section is dedicated to the major finding of this contribution. The results concerning the weakening of the *h*-BN–substrate interaction through the adsorption of single transition metal (TM) adatoms were recently published in the issue of *Physical Review Letters* **109**, 066101 (2012) [89]. The article is included within this version of the manuscript for completeness. Here, we briefly summarize the content of this work and outline the author’s contribution. The experiments were carried out in collaboration with F. Patthey. The author signs responsible for the data analysis and wrote the draft of the manuscript. The latter was subsequently refined in a concerted effort of H. Brune, F. Patthey, and F. D. Natterer.

The highlight of this work was found in the sizeable weakening of the *h*-BN–substrate interaction through the deposition of individual Mn adatoms on *h*-BN/Rh(111) at 10 K. The deposition of per mill amounts of Mn on *h*-BN/Rh(111) resulted in a distribution of two different adsorption complexes, one dot like structure, as expected for monomers, and one circular structure that was concentrically aligned in the holes of the (12×12) moiré structure. The rings exhibited a sixfold segmentation with two different maxima. In a first step, the focus was put on scrutinizing the number of adatoms per observed adsorption complex. The statistical analysis of the adsorbed Mn densities finally yielded a size of one Mn atom per adsorption complex, and a sticking coefficient for Mn on *h*-BN/Rh(111) below unity. The two different adsorption complexes, ring and dot, were found to be two distinct consequences of the same Mn adatom. We demonstrated the reversible transformation of dots into rings, and vice versa, via tip manipulation. The observed objects therefore constitute a bistable adsorption complex that can reversibly be switched between both states. The final step consisted in determining the origin of the two distinct adsorbate morphologies. Non exponential distance–current traces and $d \ln I / dz$ curves were finally the essential instrument in revealing a *h*-BN deflection in the presence of the STM tip. We introduced an empirical model based on results by Chen and Hamers [34], and found that the tunneling junction is highly deformable and almost instable for distinct positions within a Mn ring. It was shown that the interaction of the tip and sample locally deformed the *h*-BN layer. STM images recorded at low and high current finally revealed that some parts of the rings were intrinsically lifted off the substrate, while others appeared to be due to tip–sample interactions only. In a conclusion it was discussed that the doping of *h*-BN with single Mn adatoms weakened, in particular, the *h*-BN–substrate interaction in a region that is strongly hybridized with the Rh substrate. The tip mediated transformation between the ring and the dot state is interpreted as a pinning and un-pinning of the *h*-BN layer to and from the rhodium substrate.

Ring State for Single Transition Metal Atoms on Boron Nitride on Rh(111)

Fabian Donat Natterer, François Patthey, and Harald Brune

*Institute of Condensed Matter Physics (ICMP), Ecole Polytechnique Fédérale de Lausanne (EPFL),
CH-1015 Lausanne, Switzerland*

(Received 11 April 2012; revised manuscript received 15 June 2012; published 7 August 2012; publisher error corrected 13 August 2012)

The low-temperature adsorption of isolated transition metal adatoms (Mn, Co, and Fe) onto hexagonal boron nitride monolayers on Rh(111) creates a bistable adsorption complex. The first state considerably weakens the hexagonal boron nitride- (*h*-BN-) substrate bond for 60 BN unit cells, leading to a highly symmetric ring in STM images, while the second state is imaged as a conventional adatom and leaves the BN-substrate interaction intact. We demonstrate reversible switching between the two states and, thus, controlled pinning and unpinning of the *h*-BN layer from the metal substrate. $I(z)$ and $d\ln I/dz$ curves are used to reveal the BN deformation in the ring state.

DOI: 10.1103/PhysRevLett.109.066101

PACS numbers: 68.35.Np, 62.23.Kn, 68.37.Ef

Monolayers of sp^2 -hybridized honeycomb lattices, such as graphene and hexagonal boron nitride (*h*-BN), grown on close-packed single crystal surfaces are fascinating substrates, in particular in their role as novel hosts for adsorbed atoms, molecules, or nanostructures, but also due to their intrinsic electronic and structural properties. A prominent example is the moiré pattern formed by *h*-BN/Rh(111) – (12×12) [1–6]. This system is characterized by highly inhomogeneous substrate binding of the different stacking areas of the moiré unit cell. The regions where N atoms are on top of Rh atoms are strongly bound due to the hybridization of the N lone pair orbital with the Rh *d*-states [6,7]. No such chemical bond is formed where N atoms are situated on the threefold Rh hollow sites. These stacking areas are, thus, only weakly bound by van der Waals interactions [7]. Since there is only one type of on-top site and two types of hollow sites, the ratio of both stacking areas is 1:2. This gives rise to strongly bound equidistant circular regions surrounded by a connected and weakly bound area, also called wires [1].

The transition between the differently bound parts of the layer occurs on a lateral scale of only two atomic rows [7]. Therefore, the structure essentially consists of two levels, disconnected hexagonal bound areas close to the Rh, surrounded by a connected honeycomb area lifted off the substrate by 1.0 Å [7]. This abrupt transition is untypical for moiré patterns, however, since the layer doesn't exhibit holes [3], we refer to it as a moiré pattern and not as a nanomesh. The inhomogeneous binding involves a splitting of the sp^2 -derived σ and π bands by 1 eV [1,4,8] and nonuniform charge transfer from *h*-BN to Rh [7], leading to a spatial modulation of the work function [9–11] and to large lateral electric dipoles [10]. These dipoles exert electrostatic forces on polarizable adsorbates enabling the trapping of naphthalocyanine [4], of Cu-phthalocyanine [9], and of water [7,11] molecules, as well as of rare gas atoms [9,12]. Concerning metals, large Co clusters show preferred adsorption in the bound areas [13], but single

metal atoms appear less well steered as they are predominantly resting at the borders of the bound areas. Apart from a theoretical study for Au atoms revealing large binding energy differences [14], the interaction of metal atoms with the *h*-BN layer, as well as possible effects on the *h*-BN-substrate interaction, remain largely unexplored.

We report that single transition metal (TM) adatoms, namely Mn, Co, and Fe, adsorbed onto *h*-BN/Rh(111) – (12×12) , exhibit a bistable state at $T < 35$ K. The first state considerably weakens the *h*-BN substrate bond for 60 BN unit cells and is imaged in STM as a highly symmetric ring with 1.9 nm diameter that is centered in the moiré unit cell. Many rings have six symmetrically arranged protrusions, as shown in Fig. 1. The second state is imaged as a single and sharp protrusion (dot), as expected for a single adatom. We demonstrate reversible switching between the two states. Evidence for the adlayer substrate bond weakening is inferred from nonexponential current distance curves and from STM images.

The measurements were performed with a homemade STM, operating at 4.7 K and a base pressure below 5×10^{-11} mbar [15]. TM atoms were deposited from

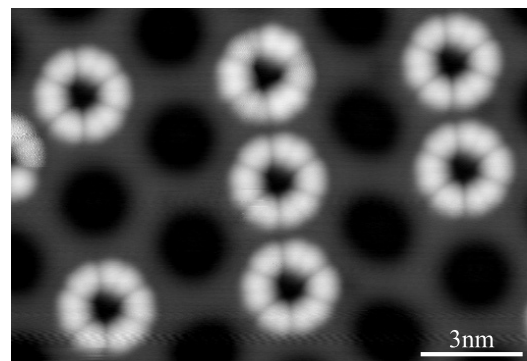


FIG. 1. STM image of highly symmetric rings centered at the apparent depressions of the *h*-BN/Rh(111) – (12×12) moiré unit cell ($V_t = -0.10$ V and $I_t = 10$ pA).

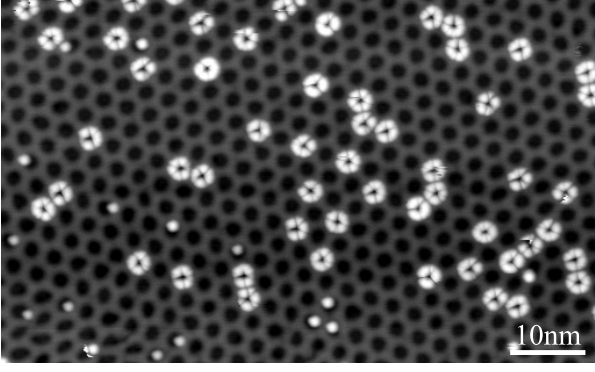


FIG. 2. STM image showing the coexistence of Mn rings with single protrusions (dots). [$\Theta = (1.71 \pm 0.03) \times 10^{-3}$ ML, $T_{\text{dep}} = 10$ K, $V_t = -0.10$ V, and $I_t = 10$ pA].

high purity rods with an *e*-beam evaporator onto the sample in the STM position and at 10 K. The *h*-BN monolayer was prepared by exposing the clean Rh(111) surface [16] at 1040 K for 100 s to a borazine partial pressure of 2×10^{-7} mbar [1]. The resulting sample exhibits large and very well ordered *h*-BN regions coexisting with the clean metal substrate. The latter serves for a precise coverage calibration. On Rh(111), Co, and Fe are immobile at $T_{\text{dep}} = 10$ K [17]. Hence, they exhibit statistical growth, leading for the low coverages used in the present study almost exclusively to single atoms; e.g., at the coverage of Fig. 2 the mean size is 1.005 [18]. Therefore, the density of adsorbates is equivalent to the coverage, given in monolayers, where one ML is defined as one adatom per Rh substrate atom. The indicated tunnel voltages V_t correspond to the sample potential. The $d \ln I / dz$ curves were measured by feeding the output of the *IV*-converter through a logarithmic amplifier into a Lock-In amplifier using a *z*-modulation of 16 pm peak-to-peak at 777 Hz.

Figure 1 shows highly symmetric rings observed after Mn deposition on *h*-BN/Rh(111) – (12×12) at 10 K. Each ring exhibits six protrusions, every other of them with slightly different appearance giving rise to threefold symmetry. All rings are concentrically arranged around the apparent moiré depressions and have a diameter of (19.2 ± 0.2) Å, which is (0.59 ± 0.01) times the moiré

period. Their apparent height with respect to the wires is 1.8 Å. Deposition of Fe and Co leads to rings with identical symmetry, diameter, and apparent height [19]. In what follows, we concentrate on Mn; however, the results are representative also for Co and Fe.

Figure 2 displays the coexistence of dot and ring state. In addition, there are asymmetric and incomplete rings. We attribute these different ring shapes to the varying TM atom position and to defects in the supporting *h*-BN. STM images of this kind are used to infer the average number of Mn atoms involved in both adsorption complexes. Deposition of a coverage Θ onto a surface with unit cells

of size n leads to a probability $P_k = \binom{n}{k} \Theta^k (1 - \Theta)^{n-k}$ of finding k atoms per unit cell [18]. For the present case of $n = 12 \times 12$ and the coverage of $\Theta = (1.71 \pm 0.03) \times 10^{-3}$ ML on the bare Rh(111) areas, we expect a fraction of $P_0 = (1 - \Theta)^n = (0.782 \pm 0.004)$ empty moiré unit cells on the *h*-BN. However, we observe with (0.833 ± 0.004) a significantly higher amount. This can either be attributed to a sticking coefficient below unity on *h*-BN, or to an adatom mobility across moiré unit cells at the deposition temperature. Sticking coefficients below one have been reported for Co/*h*-BN/Ni(111) [20]. No sign of intercell adsorbate diffusion is observed when heating the sample beyond the deposition temperature. Therefore, we attribute the larger fraction of empty cells solely to the sticking coefficient. The experimentally observed quantity of empty moiré cells is obtained for a Mn coverage on *h*-BN of $\Theta = (1.27 \pm 0.03) \times 10^{-3}$ ML. The ratio of this coverage to the one on Rh yields an initial sticking coefficient of $s_0 = (0.74 \pm 0.03)$ for Mn on *h*-BN at 10 K and concomitantly a mean size of (1.09 ± 0.02) atoms per adsorption complex. Therefore, the majority of the rings and dots originate from a single TM adatom.

We show in Fig. 3 the reversible transformation of rings into dots proving that both are different appearances and states of the same TM adatom/*h*-BN complex [21]. The transformation of a dot into a ring is achieved by applying a positive voltage pulse (+1 V, feedback-loop open) with the tip positioned on top of the dot. The back transformation is induced by a current ramp from 10 pA to 220 pA at -0.1 V with the tip centered on the former dot position [22].

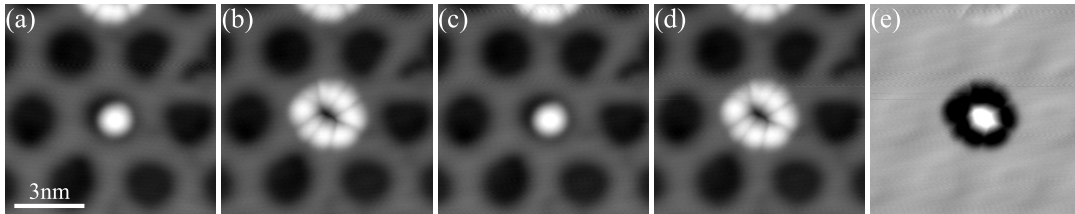


FIG. 3. Sequence of STM images, demonstrating the reversible transformation of a Mn dot into a ring and vice versa. (a)–(b) and (c)–(d) Switching a dot into a ring via a +1 V bias pulse applied at the center of the dot. (b)–(c) Transformation of a ring back into a dot via a current ramp at the former dot position ($V_t = -0.10$ V, ramp from 10 to 220 pA). Position and shape of dot and ring are unchanged. (e) Difference image of dot and ring indicates the adatom position. ($V_t = -0.10$ V and $I_t = 10$ pA).

A remarkable feature of these manipulations is that not only the dot and ring position, but also the internal ring structure are unchanged. Surprisingly, the adatom itself is hidden in STM images of the ring state. While we ignore the reason for the STM transparency of the TM atom in the ring state, we exclude the possibility that it is reversibly pushed below (ring) and pulled above the *h*-BN layer (dot), since once below, it is expected to bind much stronger to Rh.

Voltage pulses have been reported to modify the charge state and appearance of Au atoms on NaCl [23]. We, therefore, suggest the involvement of a charge difference between ring and dot state in the present study. However, the difference in appearance to the STM is much more striking in the present case. We note that 12 Xe atoms on *h*-BN/Rh(111) – (12 × 12) have been shown to form rings with similar appearance [12] and, therefore, wish to stress that the present ring state is attributed to a single TM adatom only.

The following analysis shows how the TM adatom weakens the *h*-BN–substrate bonding in the ring state. The intriguing STM appearance is due to elastic deformation of the *h*-BN layer by tip-sample interactions and due to its intrinsic detachment from the substrate. Large deformations have been reported for tip-sample interactions acting on a soft membrane, such as freestanding [24] and SiO₂ supported [25] graphene. A signature of such deformations is that the true (*s*) and apparent (*z*) tip-sample distances are different, leading to deviations from exponential *I*(*z*), respectively, constant *d*ln*I*/*dz* curves [26]. Figure 4 depicts

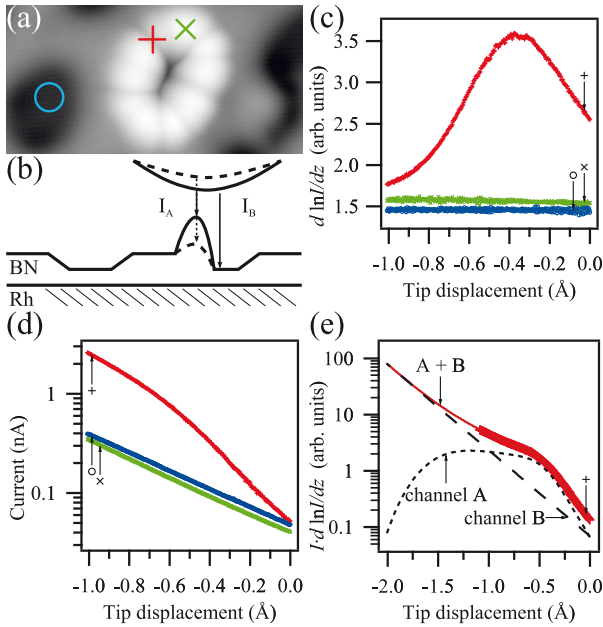


FIG. 4 (color online). (a) STM image of a Mn ring indicating the positions where (d) *I*(*z*) and (c) *d*ln*I*/*dz* curves are recorded. (b) Parallel conduction channels A and B. (e) Product of curves (+) from (c) and (d) compared to a fit produced with Eqs. (1) and (2) (*V*_t = −0.10 V and *I*_t = 20 pA).

I(*z*) and *d*ln*I*/*dz* curves recorded at three distinct positions. The current varies exponentially with tip displacement at the *h*-BN substrate (○) and at the ring maxima (×). At the ring minima, however, *I*(*z*) exhibits a change in slope and correspondingly *d*ln*I*/*dz* a large peak, see curves (+).

The exponential *I*(*z*) curve over the *h*-BN is reminiscent of the tip-sample interaction being smaller than the *h*-BN–substrate interaction, whereas we attribute the exponential *I*(*z*) signal above the ring maxima to the tip-sample interaction being stronger than the one between *h*-BN and substrate over the probed distance regime. Therefore, the *h*-BN monolayer is lifted off the substrate and attached to the tip, and the tunnel current is dominated by tunneling from this *h*-BN covered tip into Rh. Above the ring minima, the *h*-BN changes from being close to the sample at large *z* to being close to the tip at low *z*. Therefore, this regime allows us to assess the relative strength of both interactions. The current can be modeled by a superposition of two conduction channels. Channel A describes tunneling into the flexible membrane and, therefore, *s* ≠ *z*, and channel B is tunneling across the *h*-BN into the underlying metal substrate. This yields

$$-\frac{I}{2} \frac{d \ln I}{dz} = \kappa_A I_A \left(\frac{dz}{ds} \right)^{-1} + \kappa_B I_B, \quad (1)$$

where $\kappa_{A,B}$ are decay lengths of the respective wave functions [26]. *dz* and *ds* can be related by describing the tip-sample interaction with a Morse potential [26]:

$$\frac{dz}{ds} = 1 - \beta [\exp(-\kappa \Delta s) - 2 \exp(-2\kappa \Delta s)], \quad (2)$$

where Δs is the gap width relative to the point where the force between tip and sample is zero. The stability of the tunnel junction is governed by the parameter β that expresses the tip-sample stiffness [26,27]. A plot of *I**d*ln*I*/*dz* is shown in Fig. 4(e). The experimental values of curve (+) are well described by the model as indicated by the full curve. The model permits to disentangle the contributions of both conduction channels and to extract $\beta = 7.5 \pm 1.0$. This value is close to the upper limit for stability [27] and about ten times larger than in Ref. [26], where tip and sample consisted of tungsten and silicon, respectively. This scales reasonably with the Young's moduli of the respective materials of *E*_{BN} = 27 GPa [28], *E*_W = 340 GPa, and *E*_{Si} = 120 GPa [26].

The most prominent features of the ring state are the maxima. As outlined above, their appearance is caused by tip-sample interactions and an intrinsic weakening of the *h*-BN substrate bond. We now show evidence for the latter. Figure 5 compares two STM images, one recorded at a common gap resistance of *R*_g = 10⁹ Ω, and one very far from the surface at *R*_g = 2 × 10¹¹ Ω. From the line profile it is seen that one of the maxima deflects by almost 1.5 Å upon changing the tip-sample separation, whereas the apparent height of the other maximum is unaffected. This strongly suggests that the latter maximum represents an intrinsic deformation of the *h*-BN layer. Notice that the ring is located

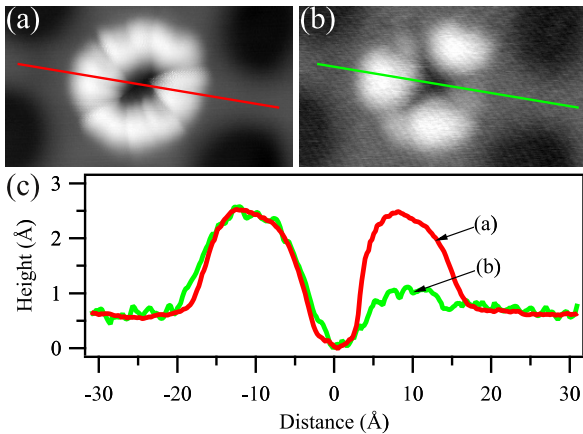


FIG. 5 (color online). STM images of the same Mn ring at (a) small and (b) large tip sample separation. While on one maximum, the *h*-BN membrane deflects by 1.5 Å between the two images, the other appears unchanged. (c) Line profiles. [$V_t = -0.10$ V, (a) $I_t = 100$ pA, and (b) $I_t = 0.5$ pA].

at the transition from the strongly to the weakly bound *h*-BN, and surprisingly, it is this transition region that gets detached in the ring state, while the weakly bound wires remain unaffected. This can be seen from the apparent heights of the wire areas between adjacent rings equaling the ones around empty moiré cells in Fig. 1. We note that a local weakening of the *h*-BN/Rh bond has been calculated for Au adsorption [14]; however, the present weakening goes far beyond in magnitude and in spatial extent.

In summary, the low-temperature deposition of small amounts of transition metal atoms (Mn, Fe, and Co) leads to a distribution of single adatoms on *h*-BN/Rh(111). Such a doping drastically influences the bonding of the *h*-BN layer to the metal substrate. A single TM adatom weakens the interaction of more than 60 surrounding *h*-BN unit cells to the underlying metal. The adsorption complex can be switched between the dot and the ring state and thereby the *h*-BN layer can be pinned to and un-pinned from the metal substrate in a reversible and controlled fashion.

We gratefully acknowledge funding from the Swiss National Science Foundation and discussions with M. Iannuzzi, P. Blaha, and F. Mittendorfer.

- [1] M. Corso, W. Auwärter, M. Muntwiler, A. Tamai, T. Greber, and J. Osterwalder, *Science* **303**, 217 (2004).
- [2] O. Bunk, M. Corso, D. Martoccia, R. Herger, P.R. Willmott, B.D. Patterson, J. Osterwalder, J.F. v.d. Veen, and T. Greber, *Surf. Sci.* **601**, L7 (2007).
- [3] R. Laskowski, P. Blaha, T. Gallauner, and K.H. Schwarz, *Phys. Rev. Lett.* **98**, 106802 (2007).
- [4] S. Berner, M. Corso, R. Widmer, O. Gröning, R. Laskowski, P. Blaha, K. Schwarz, A. Goriachko, H. Over, S. Gsell, M. Schreck, H. Sachdev, T. Greber, and J. Osterwalder, *Angew. Chem., Int. Ed.* **46**, 5115 (2007).

- [5] R. Laskowski and P. Blaha, *J. Phys. Condens. Matter* **20**, 064207 (2008).
- [6] A.B. Preobrajenski, A.S. Vinogradov, May Ling Ng, E. Čavar, R. Westerström, A. Mikkelsen, E. Lundgren, and N. Mårtensson, *Phys. Rev. B* **75**, 245412 (2007).
- [7] Y. Ding, M. Iannuzzi, and J. Hutter, *J. Phys. Chem. C* **115**, 13685 (2011).
- [8] T. Brugger, H. Ma, M. Iannuzzi, S. Berner, A. Winkler, J. Hutter, J. Osterwalder, and T. Greber, *Angew. Chem., Int. Ed.* **49**, 6120 (2010).
- [9] H. Dil, J. Lobo-Checa, R. Laskowski, P. Blaha, S. Berner, J. Osterwalder, and T. Greber, *Science* **319**, 1824 (2008).
- [10] T. Greber, M. Corso, and J. Osterwalder, *Surf. Sci.* **603**, 1373 (2009).
- [11] H. Ma, T. Brugger, S. Berner, Y. Ding, M. Iannuzzi, J. Hutter, J. Osterwalder, and T. Greber, *Chem. Phys. Chem.* **11**, 399 (2010).
- [12] R. Widmer, D. Passerone, T. Mattle, H. Sachdev, and O. Gröning, *Nanoscale* **2**, 502 (2010).
- [13] J. Zhang, V. Sessi, C.H. Michaelis, I. Brihuega, J. Honolka, K. Kern, R. Skomski, X. Chen, G. Rojas, and A. Enders, *Phys. Rev. B* **78**, 165430 (2008).
- [14] H.P. Koch, R. Laskowski, P. Blaha, and K. Schwarz, *Phys. Rev. B* **84**, 245410 (2011).
- [15] R. Gaisch, J.K. Gimzewski, B. Reihl, R.R. Schlittler, M. Tschudy, and W.D. Schneider, *Ultramicroscopy* **42–44**, 1621 (1992).
- [16] The Rh(111) single-crystal was cleaned by cycles of Ar⁺ ion sputtering (300 K, 30 min, 10 μA/cm², 1 kV), annealing in oxygen (815 K, 5 min, 2 × 10^{−7} mbar), and flashed to 1450 K.
- [17] P. Blonski, A. Lehnert, S. Dennler, S. Rusponi, M. Etzkorn, G. Moulas, P. Bencok, P. Gambardella, H. Brune, and J. Hafner, *Phys. Rev. B* **81**, 104426 (2010).
- [18] H. Brune, *Surf. Sci. Rep.* **31**, 121 (1998).
- [19] Ti, Cr, Cu, and Au do not show such a ring state.
- [20] W. Auwärter, M. Muntwiler, T. Greber, and J. Osterwalder, *Surf. Sci.* **511**, 379 (2002).
- [21] Further evidence for rings and dots being different appearances of the same entity comes from their respective densities. While the ring and dot densities strongly vary from one STM image to another, their sum is constant within the error bar.
- [22] All three adsorbates can be removed by a voltage pulse, which is element specific and independent of polarity in the ring state: $|V_{Mn}| = 1.7 \pm 0.1$ V, $|V_{Fe}| \approx 0.6$ V, $|V_{Co}| = 0.4 \pm 0.2$ V.
- [23] J. Repp, G. Meyer, F.E. Olsson, and M. Persson, *Science* **305**, 493 (2004).
- [24] C. Lee, X. Wei, J.W. Kysar, and J. Hone, *Science* **321**, 385 (2008).
- [25] T. Mashoff, M. Pratzer, V. Geringer, T.J. Echtermeyer, M.C. Lemme, M. Liebmann, and M. Morgenstern, *Nano Lett.* **10**, 461 (2010).
- [26] C.J. Chen and R.J. Hamers, *J. Vac. Sci. Technol. B* **9**, 503 (1991).
- [27] C.J. Chen, *Introduction to Scanning Tunneling Microscopy* (Oxford University Press, New York, 1993).
- [28] A. Bosak, J. Serrano, M. Krisch, K. Watanabe, T. Taniguchi, and H. Kanda, *Phys. Rev. B* **73**, 041402 (2006).

We intend to use the remaining part of this section to advance more into aspects of the work of TM adatoms on *h*-BN/Rh(111). As we have mentioned in the beginning of this section, circular structures were observed after the dosing of per mill amounts of the transition metals Mn, Fe and Co at 10 K [cp. Fig. 3.13(a)]. We originally encountered Co rings in our study of Co island densities and later expanded the findings to iron and manganese. The latter proved to be particularly convenient in the study of the ring properties, as Mn was the most stable element with regard to the scanning bias of the tip.

A comparison of three samples with per mill amounts of Mn, Fe, and Co is shown in Fig. 3.16(a)-(c). The TM adatoms were deposited onto the *h*-BN/Rh(111) surface at 10 K. In either sample, TM rings are encountered distributed about the surface as they are concentrically aligned in the center of the moiré unit cells. We also observe a number of individual protrusions referred to as dots. A superimposed line profile across a Mn, Fe, and Co ring in Fig. 3.16(e) exemplifies the similarities between the observed rings of different adsorbate species. The diameter, the apparent height and the shape are equivalent in Mn, Fe and Co rings within experimental precision. In fact, there is no way to distinguish one element from the other with the help of such a line profile alone.

There is, however, an element specific threshold bias for destruction that would allow in principle to differentiate among rings of different elements. We observe a removal of the ring from the surface when the bias voltage reaches a characteristic magnitude. In order to systematically study this threshold bias, we recorded $z - V$ traces with the tip centered on top of the ring. Hereby, the bias voltage is stepwise increased and the feedback-loop left locked so that it maintains the setpoint current. Accordingly, the tip moves away from the surface as the voltage is increased. At the mentioned threshold value, however, the tip suddenly jumps toward the sample because the ring has disappeared from the junction which renders the gap width too large for the desired current. Figure 3.17(a) shows a $z - V$ trace for the example of a Co ring. Inspecting the bias values of the respective elements reveals why we focus on manganese rather than on the other elements. The threshold biases for the respective elements are $|V_{\text{Mn}}| = 1.7 \pm 0.1$ V, $|V_{\text{Fe}}| \approx 0.6$ V, $|V_{\text{Co}}| = 0.4 \pm 0.2$ V. Note that the threshold bias for iron represents an order of magnitude, because we have no reliable statistics for this element¹⁵. Since we do not find any additional structures nearby a destroyed TM ring, it is reasonable to assume that the material is transferred from the ring to the tip. In terms of the threshold bias we recognize that manganese rings represent the most stable species. We encountered, however, the least stable Co rings first. It is for the high bias value of $V_t = -1$ V that we were oblivious to the presence of Co rings at the beginning of our Co deposition study. All then present rings were readily swept away from the scanning region. Only after we started to worry about the noise issues while scanning with the tip, did we successfully tune the scanning parameters in a way that was described in the previous section. After we had encountered iron and manganese as ring forming elements, we naturally decided to focus on the most robust candidate Mn. We have to emphasize, however, that also for the gentle scanning conditions

¹⁵Only three $z - V$ traces were recorded for Fe.

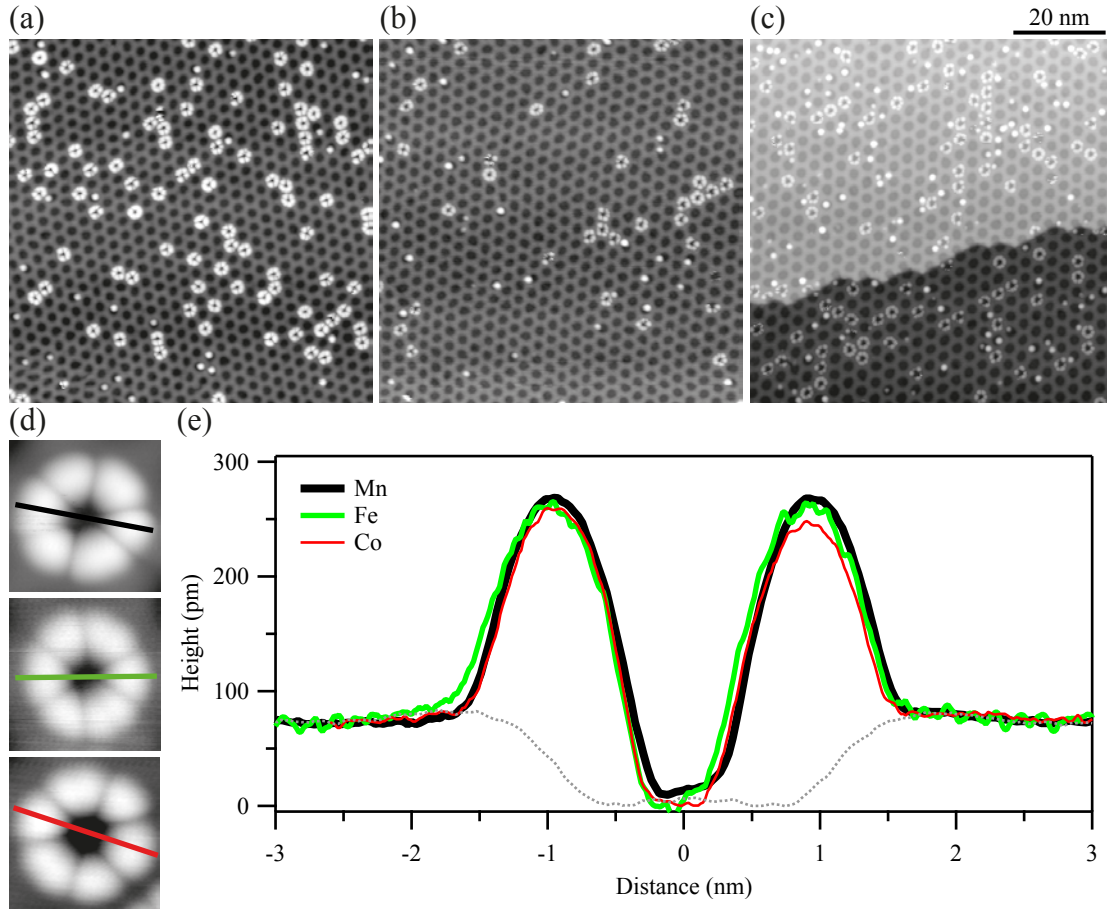


Figure 3.16: STM images of a distribution of (a) Mn, (b) Fe, and (c) Co rings and dots deposited on *h*-BN/Rh(111) at 10 K. (d) Zoom into Mn (top), Fe, and Co (bottom) rings indicating where the respective (e) line profile was recorded. ($V_t = -100$ mV and $I_t = 10$ pA).

applied, the shape of the tip can have a considerable influence on the tip–sample interaction. In some cases, the interplay was so strong that all the material was basically swept away from the scanning region. In such cases we had to treat the tip by voltage pulses or gentle collisions with the surface. Furthermore, we also observed a spontaneous removal of rings, a sudden transformation of a ring into a dot, and, very rarely, the opposite, while scanning with the optimized scanning conditions.

As we have seen for low coverages of Ti and Co, the mean island size of the observed adsorption complexes is close to one. A small deviation from unity was found to be due to an initial sticking coefficient below one. If we correct for the latter, we can attribute to almost all encountered TM complexes one individual atom. The same analysis was carried out for Mn deposited on *h*-BN/Rh(111) [89] and yielded the equivalent conclusion that the observed structures were composed of exactly one adatom. For the statistical analysis, no distinction between dots and rings was made, and both were counted with the same weight. We observed that, while the total number of structures remained constant, the individual populations

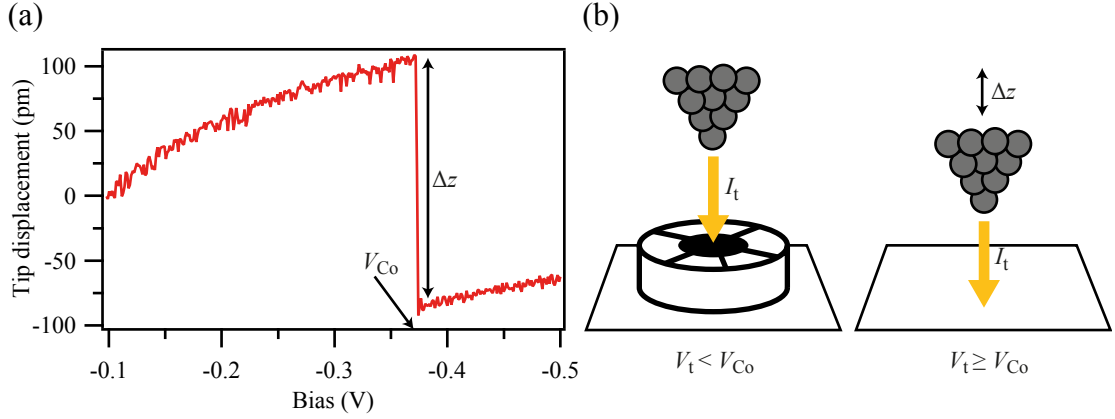


Figure 3.17: Element specific threshold bias for destruction of Mn, Fe, and Co rings. (a) Example of a $z - V$ trace for cobalt. For recording $z - V$ traces the tip is positioned on top of the ring, the bias voltage is stepwise increased, and the feedback-loop left engaged to maintain the setpoint current constant. (b) At a characteristic bias value (V_{Co}) the ring is removed from the surface and the tip jumps toward the sample in order to again reach the setpoint current.

of rings and dots strongly varied from one surface region to the next. For the Mn coverage of $\Theta = (1.22 \pm 0.03) \times 10^{-3}$ ML, an ensemble of $N = 54$ STM images was collected, and the respective densities were evaluated. The corresponding distributions ($\mu \pm \sigma$) for the total number of objects, the number of rings, and the number of dots are (93 ± 11) , (50 ± 25) , and (43 ± 25) . The width of the total distribution is visibly more narrow than of the individual ones. Figure 3.18 demonstrates the strong variation of the respective population for the same sample, recorded on distinct regions of the surface. Image Fig. 3.18(a) features a majority of rings, and Fig. 3.18(b) is an example of the opposite extreme. The total number of objects is the same for both regions. The origin of this strong variation is hitherto unknown. The quality of the *h*-BN layer had little influence whether predominantly rings or dots were measured. However, as we have established previously, the tip plays a crucial role for the effective tip-sample interaction. Some tips were particularly aggressive, and scanning with such a tip resulted in many spontaneous transformations of rings into dots with the corresponding shift of the individual populations¹⁶. Such a transformation can be seen as a partial ring that, from one scanning line to the next, suddenly appears as a dot. A manganese ring that spontaneously transforms into a dot is marked by a dashed circle in Fig. 3.19(b). It may well be that rings are also transformed into dots before parts of them are actually imaged. This may indicate that the TM rings constitute the true ground state of the bistable TM adsorption complex.

From the statistical analysis of the respective ring and dot densities it was concluded that both constitute distinct characteristics of the same TM adatom [89]. A further proof of this conclusion was found in the possibility to transform dots into rings, and vice versa, via tip manipulation. Figure 3.19 shows a collection of dots before and after applying a +1 V bias

¹⁶Note that all stated object densities should always be regarded as equal or higher than the actually measured one, since the tip was found to readily remove particles from the surface and to never add them.

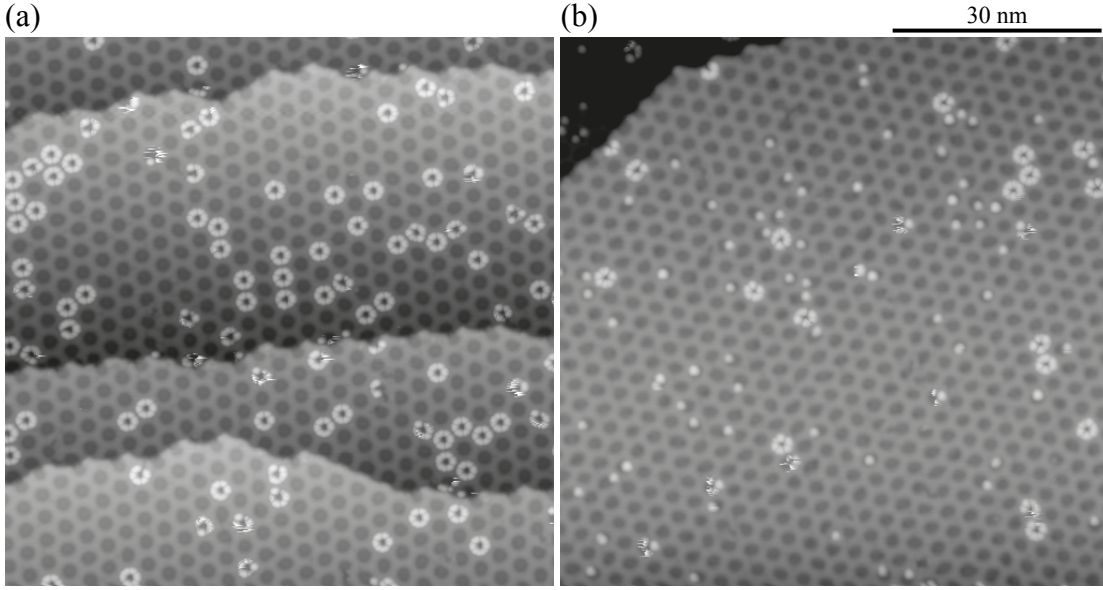


Figure 3.18: STM images of the same sample showing two extremes of the a majority of (a) rings and (b) dots for a Mn coverage of $\Theta = (1.22 \pm 0.03) \times 10^{-3}$ ML deposited at 10 K. ($V_t = -100$ mV and $I_t = 10$ pA).

pulse with the tip positioned on either dot. One appreciates the successful switching of several dots into rings. Other dots are displaced, some disappear, and one is observed to form a ring in a neighboring moiré unit cell.

Figure 3.20 directs the attention at the highlighted ring of Fig. 3.19. This structure exhibited a spontaneous switching from one state into the other upon scanning past a threshold position. A voltage pulse was consequently applied to force the dot back into the ring state. It was impossible to capture the ring as a whole. However, when scanning from four perpendicular directions, starting from an initially prepared ring state, it was feasible to record either side until the tip reached the position where the spontaneous transformation occurred. The so collected STM images were glued together, as is shown in the collage of Fig. 3.20(a). Interestingly, the overlap of the individual image fragments reflect the same internal ring structure. This constitutes another proof that the position and ring structure are preserved in between transformations. Within the region marked by the black rectangle, the ring state was particularly instable and almost instantaneously switched back to the dot state, if a voltage pulse had been applied before [cp. Fig. 3.20(b)]. The switching behavior is a beautiful example of the reversibility of the ring-dot transformation. A more controlled shift from the ring into the dot state was reported in our contribution [89], where a current ramp induced the transformation (10–220 pA, at $V_t = -1$ V).

Several experimental observations pointed toward a weakening of the *h*-BN layer–substrate interaction in the ring state. These conclusions stem from non-exponential distance–current traces and STM images recorded at different tip–sample separations. If the tip–sample in-

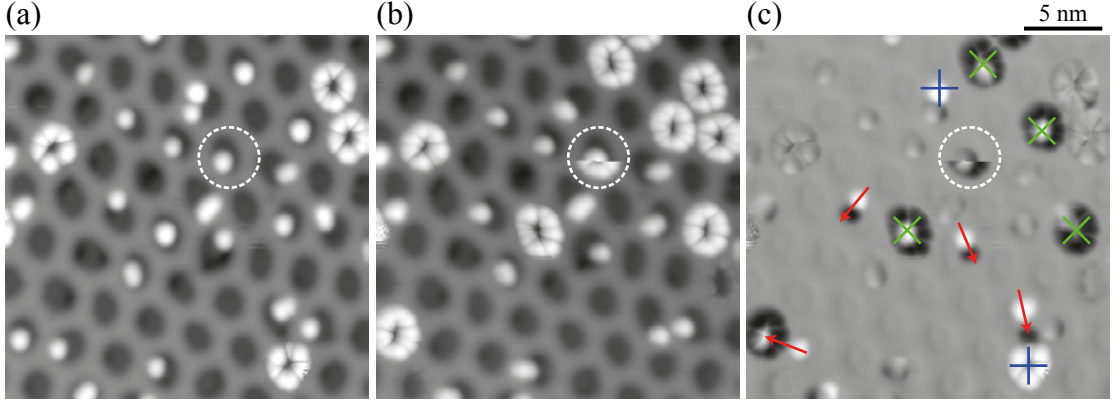


Figure 3.19: STM image (a) before, and (b) after applying a +1 V voltage pulse with the tip positioned on either dot. The difference image in (c) reveals the successful transformations of dots into rings (\times). Some dots jump to a new adsorption site (arrow) and other dots and rings disappear (+). The dashed circle highlights a particularly instable ring. ($V_t = -100$ mV and $I_t = 10$ pA).

teraction competes with the forces exerted between *h*-BN–substrate, the tunneling junction ceases to be rigid, *i.e.*, the sample is deformed in the presence of the tip, and the gap width is concomitantly modified. In this regard, we have to distinguish between true (s) and apparent (z) gap width. The latter denotes the experimentally accessible parameter. Figure 3.21(b) illustrates the sample deformation (Δh) upon shifting the tip toward the sample. If the sample deforms in the presence of the tip, the experimentally imposed tip displacement (Δz) will result in a non-exponential response of the tunneling current. Examples of such $I - z$ curves are presented in Fig. 3.21(c). Simultaneously recorded $d \ln I / dz$ curves in Fig. 3.21(d) exhibit pronounced peaks with tip displacement for flexible, and are constant for rigid parts of the sample. In order to describe the experimental data, we followed Chen and Hamers [34], but slightly modified their model [cp. Eq. 2.4] to include two parallel conducting channels [cp. Fig. 3.21(b)]. One channel (I_A) is the tunneling into the flexible *h*-BN layer ($s \neq z$), and the other (I_B) describes tunneling into the rigid substrate ($s = z$). We use the product of current and $d \ln I / dz$ for our fit procedure through the set of equations [89]:

$$\begin{aligned}
 I_t(z) \frac{d \ln I_t(z)}{dz} &\propto \left(\kappa_A I_A(s(z)) \left(\frac{dz}{ds} \right)^{-1} + \kappa_B I_B(z) \right) \\
 z &= s + \alpha F \\
 F &= -\frac{\beta}{\alpha \kappa} [\exp\{-\kappa(s - s_e)\} - \exp\{-2\kappa(s - s_e)\}] \\
 \frac{dz}{ds} &= 1 - \beta [\exp\{-\kappa(s - s_e)\} - 2 \exp\{-2\kappa(s - s_e)\}].
 \end{aligned} \tag{3.8}$$

The parameters κ , s_e , β , and α , denote the decay length, the equilibrium distance, the stiffness parameter, and the elastic constant, respectively. In order to reduce the number of fit parameters, we have made the assumption that $\kappa = \frac{1}{2}(\kappa_A + \kappa_B)$. Furthermore, we have applied the total tunneling current constraint, $I_t(z) = I_A(s(z)) + I_B(z)$. The $I d \ln I / dz$ curves are shown

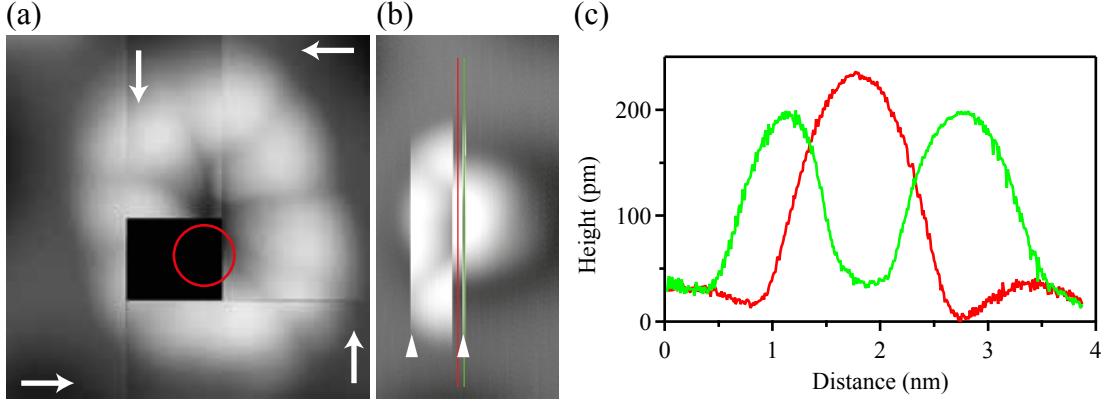


Figure 3.20: Highlight of the fragile ring of Fig. 3.19 that repeatedly switched into the dot state when the scan reached a distinct position. (a) STM image collage composed of individual scans from the four directions (arrows) across the Mn ring until it spontaneously switched to the dot state. The red circle marks the position of the Mn adatom. (b) Scan from bottom to top (image is rotated by 90°), first +1 V pulse (at scan line marked by triangle) switching it to the ring state, spontaneous change to dot after some scan lines, second pulse (triangle) back to ring, and back to dot after a few scan lines. (c) Line profile of respective dot and ring state. ($V_t = -100$ mV and $I_t = 10$ pA).

with their corresponding fit in Fig. 3.21(e). The fit parameters for the positions (1)–(5) are given in table 3.2. The general agreement between experimental data and model is good. The model

Table 3.2: Fit parameters deduced from Fig. 3.21(e) as obtained by Eq. 3.8. Values without error bars are synonymous to an imposed constraint.

Position	κ_A (1/Å)	κ_A (1/Å)	β	s_e (Å)
(1)	0	1.027	0	0
(2)	0	1.085	0	0
(3)	1.56 ± 0.14	1.027	5.3 ± 0.5	-1.78 ± 0.10
(4)	1.48 ± 0.10	1.31 ± 0.01	7.2 ± 0.1	-1.30 ± 0.05
(5)	1.52 ± 0.07	1.62 ± 0.02	6.6 ± 0.1	-1.30 ± 0.03

naturally recuperates the decay length of the *h*-BN layer (1) that was found from measuring the slope of the $I - z$ trace. For the curves measured along the radius of the Mn ring, the fit values characterize the *h*-BN layer as being highly flexible, in particular, the parameters β assume large magnitudes close to the upper limit for stability [33]. There is a minor deviation at small tip displacement for the cases (4) and (5), which might occur due to an offset error of the logarithmic amplifier. Note that the latter is optically enhanced by the logarithmic representation of the y -axis. The three traces (3)–(5) have their equilibrium position in the sampled region of this measurement. This implies that upon approaching the tip toward the sample, the *h*-BN layer is first attracted to the tip until, at a certain threshold separation, it

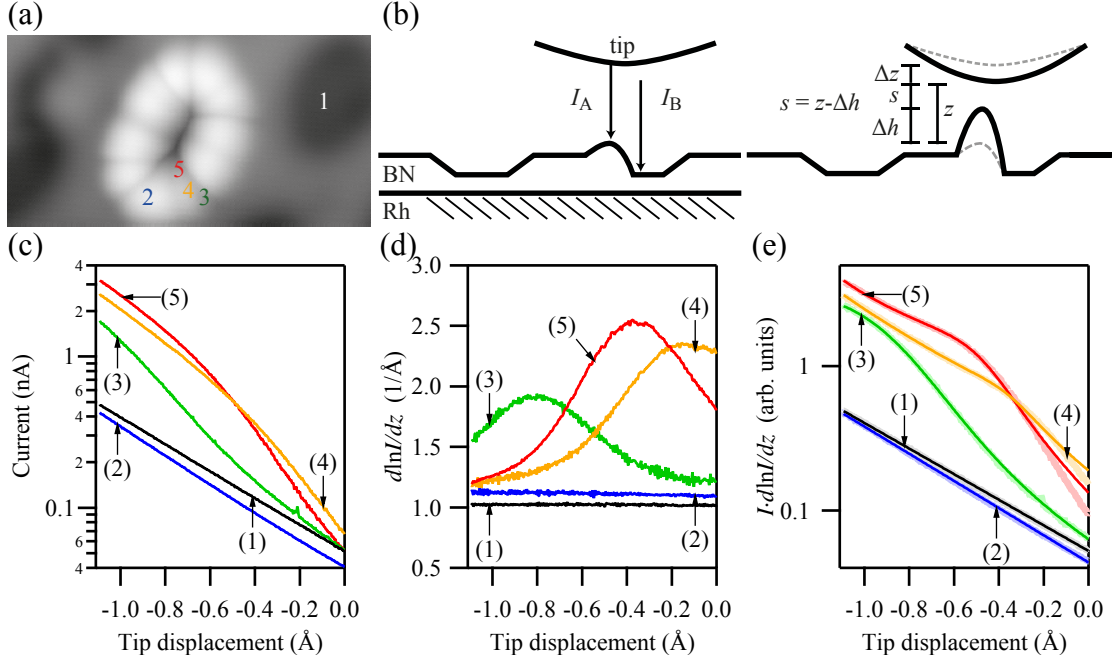


Figure 3.21: (a) STM image of a Mn ring indicating where the respective spectroscopy was recorded. (b) Illustration of the two parallel conduction channels and the *h*-BN layer deflection (Δh). Note the distinction between the true (s) and the apparent (z) gap width. Simultaneously recorded (c) $I - z$, (d) $d \ln I / dz$, and (e) $I d \ln I / dz$ curves. (setpoint before opening the feedback-loop: $V_t = -100$ mV and $I_t = 5$ pA.)

is commensurate with the tip displacement¹⁷. In the latter situation, the current–distance dependence is exponential again due to the second conduction channel. This tendency is indicated in traces (4) and (5) as both asymptotically tend to a value of about 1.085 \AA^{-1} in $d \ln I / dz$ for small tip–sample separation. The asymptotic value is coherent with the one deduced from the Mn ring maximum position (2). At the ring maximum, the *h*-BN layer is assumed to follow the tip displacement. The peak heights in Fig. 3.21(d) have to be critically viewed. Measuring the $d \ln I / dz$ signal at the tip–sample separation of the peak could lead to an erroneous assignment of physically unlikely barriers of 40 eV and beyond. It is therefore essential to inspect the current–distance, and especially the $d \ln I / dz$ behavior for a variety of tip–sample separations. We remark that the deflection of the *h*-BN layer toward the tip results in a markedly lower current rise as opposed to the similar case of graphene, when the latter jumps into contact [83]. This may be interpreted in terms of a recuperation of the *h*-BN intrinsic dielectric properties, since we recall that the *h*-BN layer is strongly hybridized with the metal support before the weakening of the *h*-BN–substrate interaction.

The above measurements indicate a *h*-BN deflection toward the sample upon reducing the gap width of the tunneling junction. The maxima were interpreted as being in permanent contact with the tip, or, in other words, commensurate with tip displacement. At very large

¹⁷The first channel is suppressed because $(dz/ds)^{-1} = 0$.

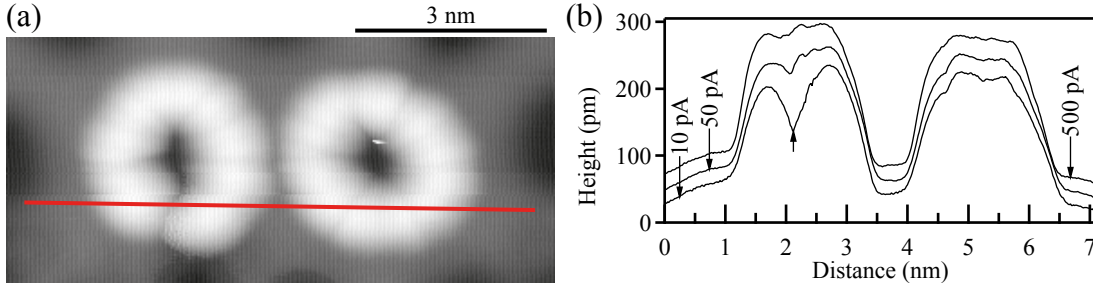


Figure 3.22: (a) STM image indicating where the (b) line scan at varying current was recorded. It is seen that the *h*-BN layer deflects toward the tip (arrow) as the tip-sample separation is reduced. ($V_t = -100$ mV and $I_t = 10$ pA).

tip-sample separation, it was shown that every second maximum appeared as a minimum and the corresponding parts of the *h*-BN layer were showing a deflection of about 1.5 \AA [89]. For the opposite extreme of very small tip-sample separations, we observe the deflection of a minimum toward the tip that is subsequently measured with the same apparent height as the neighboring maxima. Figure 3.22 shows the corresponding experiment. We recorded the Mn ring at the indicated position in the line-scan mode at stepwise increasing tunneling current. The 10 pA trace denotes the starting point and the ring exhibits the known segmentation into maxima and minima. However, if the gap width is reduced, the minimum starts to fade away and gradually assumes the same apparent height as the neighboring maxima at 500 pA¹⁸. The interpretation is the same as in the large gap width scenario. The minima have their equilibrium position in the very proximity of the surface and are therefore only attracted if the tip is brought sufficiently close to the sample. It would be interesting to test whether the remaining maxima are intrinsically lifted off the sample when the gap width is further increased, or whether the maxima are due to a tip-sample interaction. Physical limitations of the STM, however, render this test inaccessible with this technique since the effective current would be close to zero¹⁹. The employment of an AFM would constitute an ideal alternative technique.

Differential conductance measurements at the distinct parts of the Mn ring and dot did not reveal any characteristic features. Figure 3.23(b) shows the equivalent spectra for dI/dV traces on a dot (1), ring maxima and minima (2), and the *h*-BN layer (3), respectively. The dip at the Fermi energy persists at all point spectroscopy locations and is therefore a remainder of some tip structure. Turning to the differential conductance of a Mn ring at the bias of ± 100 mV that is typically used for recording topographic STM images. We immediately recognize that the dI/dV is totally flat and no DOS anomaly emerges at these energies. The respective spectra are particularly valuable in that they exclude drastic changes in the LDOS to be responsible for the intriguing maximum/minimum structure of a TM ring. Such a conclusion could

¹⁸It was impossible to measure the Mn ring as a whole at 500 pA, presumably because the tip was too close and therefore removed the TM adatom.

¹⁹Note the exponential current-distance dependence. The inspection of the Mn ring at the largest gap width relied on a current as low as 0.5 pA.

erroneously be made from dI/dV maps as is discussed in the following. It is important to remind that the point spectroscopy measurements just described, were recorded with the lateral tip position held fixed. In point STS, the tip is stabilized with respect to the sample and the vertical tip-sample separation is constant. The *h*-BN layer therefore assumes a position based on the forces acting in the tunneling junction but otherwise remains in its relative position with respect to the sample during the dI/dV measurement. In a dynamic approach of recording dI/dV and $d\ln I/dz$ maps, the tip-sample separation permanently changes and concomitantly the tip-sample interaction always varies. This means that the *h*-BN layer is always exposed to different forces. Ring regions that have their equilibrium position in the range of the probed tip-sample separation are consequently permanently attracted or repelled from and to the passing tip. If one solely relied on the inspection of the dI/dV map in Fig. 3.23(c), one would be tempted to interpret the sizeable dI/dV increase at the ring minima as being due to variations of the LDOS between ring minima and maxima. However, the point spectra in Fig. 3.23(b) are clearly devoid of any such LDOS characteristic. A comparison with $d\ln I/dz$ maps indicates anomalies at the identical positions, *i.e.*, the ring minima, as in the dI/dV maps before. The former, however, were shown to be a consequence of a deflecting *h*-BN layer in the presence of the tip. The tip in dI/dV maps can therefore be seen as traversing regimes of attraction and repulsion that were likewise responsible for the peaks in $d\ln I/dz$ point spectra, seen in Fig. 3.21(d). It is essential to keep a potentially flexible sample in mind. If one was to illustrate local variations of the apparent barrier height by recording $d\ln I/dz$ maps, he or she would erroneously ascribe physically unlikely high barriers to the flexible parts of the *h*-BN layer²⁰. The combination of point spectroscopy and spectroscopic maps is the key in the analysis of flexible tunneling junctions. Note that spectroscopy was carried out between ± 100 mV and cannot exclude the existence of characteristic DOS features at higher energies. The measurement of such states, if they existed, would be challenging. We showed that the rings could spontaneously switch between the dot and the ring state, and that they were removed from the tunneling junction at a certain threshold bias that naturally limits the useful energy interval for performing spectroscopy.

In summary, we could show that the observed ring structures were a consequence of a pronounced weakening of the *h*-BN layer-substrate interaction that arises upon adsorption of individual adatoms of Mn, Fe, or Co in the center of the moiré unit cell. Some parts of the ring were shown to deflect in the presence of the tip, and some ring maxima appeared to be intrinsically lifted off the substrate, as they persisted at the largest measured gap widths. No topographic distinction could be made between rings resulting from different TM adatoms. The intriguing ring structure is therefore based on the same origin for all measured rings. The experiments highlight that the actually depicted topography in STM images is the deformed *h*-BN layer. The reason why the TM adatom remains invisible in the ring state is hitherto unknown. The increased apparent barrier height at the center of the ring in point $d\ln I/dz$ spectra could, however, hint toward a charge contribution, *i.e.*, the TM adatom might

²⁰Note that parts of the Mn ring appearing flexible at intermediate gap width, *i.e.*, ring minima at $V_t = -100$ mV and $I_t = 20$ pA, might be in a different regime of attraction for larger gap width.

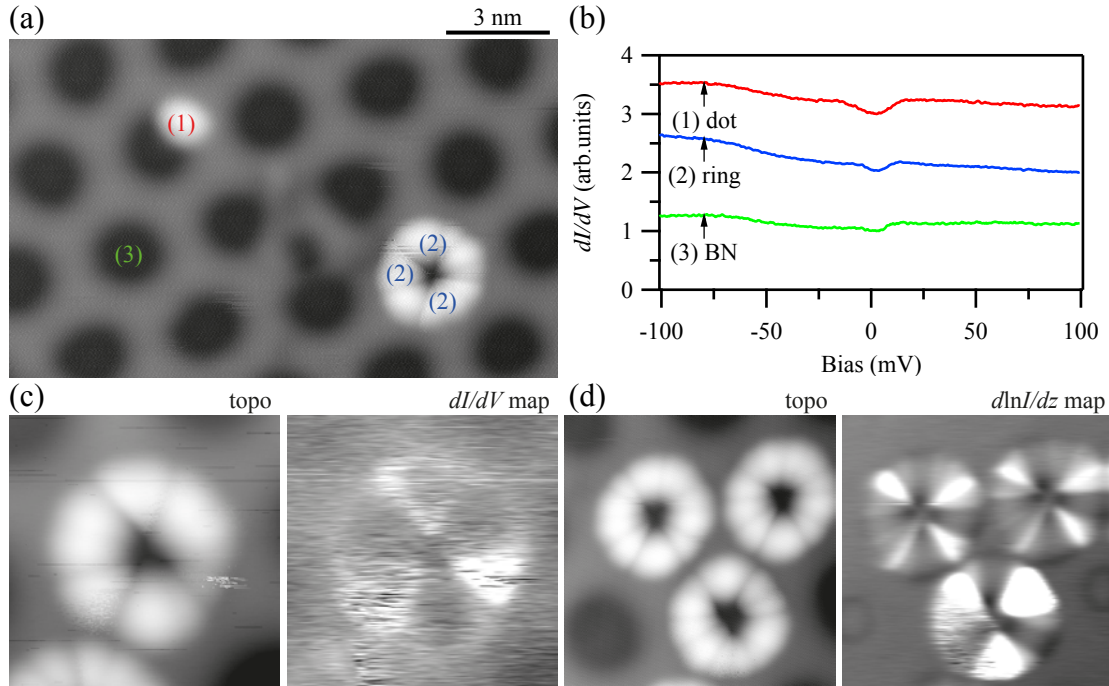


Figure 3.23: Spectroscopy on Mn ring and dot state. (a) STM image indicating where the point spectra of (b) were recorded. (b) No characteristic signature for either ring or dot state is visible in differential conductance. The highlights in (c) dI/dV and (d) $d\ln I/dz$ maps are reminiscent of a moving h -BN layer in the presence of the passing tip and do not represent regions with distinct spectral signature. [(a) $V_t = -100$ mV and $I_t = 50$ pA, (c) $V_t = -500$ mV and $I_t = 50$ pA, (d) $V_t = -100$ mV and $I_t = 20$ pA].

carry a negative partial charge, resulting in an increased dipole moment at the ring center. It would be worthwhile to also theoretically investigate the influence of a Mn adatom on the h -BN–substrate bonding²¹.

3.2.4 Xe on h -BN/Rh(111)

As mentioned in the introduction of this section, the h -BN/Rh(111)–(12×12) moiré pattern was shown to exhibit interesting trapping capabilities for a whole family of polarizable molecules and atoms. Among these were rare gas atoms of Xe [39, 143]. Dil *et al.* [39] predicted that 12 Xe atoms would form rings along the circumference of the holes of the moiré pattern. Later, Widmer *et al.* [143] confirmed the existence of such Xe rings with STM. The topographic similarities between Xe and Mn rings stimulated the experimental confrontation of both structures.

For a direct comparison, a sample with Mn rings was prepared by the deposition of 5×10^{-4} ML manganese on h -BN/Rh(111) at 10 K. The so arranged surface was then exposed to a

²¹Preliminary DFT studies of H.-P. Koch showed unexpected conversion problems for Mn/ h -BN/Rh(111). Unfortunately, these studies were abandoned before shedding a significant insight into the system.

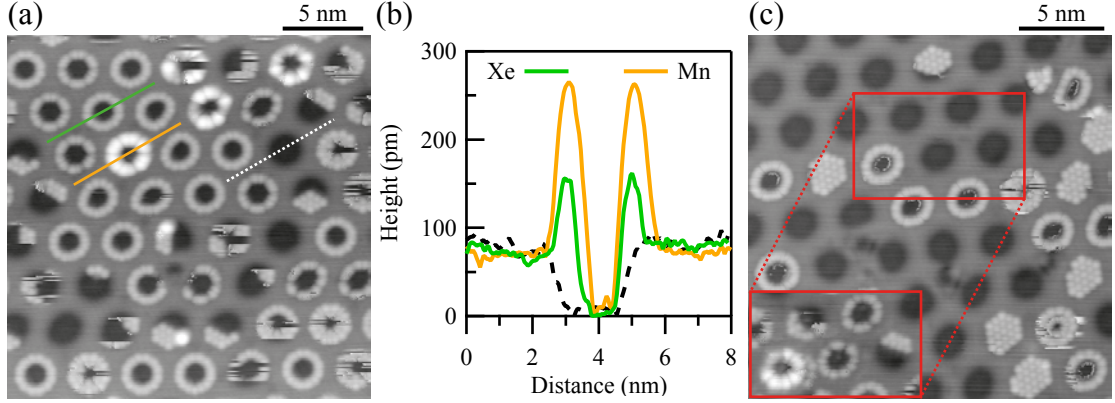


Figure 3.24: Comparison of Mn and Xe rings after the exposure of a Mn/*h*-BN/Rh(111) sample to a partial pressure of Xe at 10 K. (a) STM image showing the coexistence of Mn, Xe, and mixed rings. (b) Height profile across Mn and Xe rings. (c) STM image of a similar region after a scan with 1 nA that resulted in the collapse of Xe rings into distinct Xe crystallites. The frame highlights a mixed Mn–Xe ring before and after it is deprived of its Mn atom and replaced by a pure Xe ring due to the high current scan. [(a) $V_t = -100$ mV and $I_t = 10$ pA, (c) $V_t = -20$ mV and $I_t = 10$ pA.

xenon dose of about 10 L at 10 K²². Figure 3.24(a) shows the resulting topography. Virtually all holes of the moiré pattern are occupied by Xe rings. We can immediately appreciate the apparent height difference of 100 pm between Mn and Xe rings, as the inspection of the line profile in Fig. 3.24(b) suggests. It is, however, difficult to satisfyingly conclude from our STM data whether the Xe ring occupation of 12 atoms is respected or not. Given that the centers of many Xe rings exhibit a noise when scanning, Xe adatoms appear to remain highly mobile, even at 4.7 K. This mobility could obscure the Xe number determination. The inspection of Xe rings with $I - z$ and $d \ln I / dz$ spectroscopy did not show any gap width dependency, in contrast to the neighboring Mn rings, that showed the known peaks in $d \ln I / dz$ traces at the ring minima. Note that some structures seem to be mixed Xe and Mn rings. This may well be the case, since we recall the distinction between the intrinsic *h*-BN detachment and the one caused by tip-sample interaction. The latter regions could therefore be occupied by Xe atoms. Interestingly, the mixed ring can be forced into a pure Xe ring by scanning the surface at a high current that is known to remove Mn from the surface. Figure 3.24(c) shows the sample after such a scan with a tunneling current of 1 nA. The mixed Mn–Xe ring of the highlighted frame was deprived of the Mn adatom what resulted in a pure Xe ring. Many other Xe rings, however, collapsed into Xe crystallites or were removed in the course of the latter scan. The Xe–Xe distance in the crystallites is (4.4 ± 0.1) Å, in agreement with the nearest neighbor separation in bulk Xe. In summary, although Xe rings appear similar to Mn rings at first sight, they are, after close inspection, the result of different phenomena. While Xe rings are truly composed of several atoms, the Mn and TM rings are the result of a single atom. In the latter case, the *h*-BN–substrate interaction is strongly perturbed, while it remains intact for Xe adsorbates.

²²Note that this Xe dose is an approximate figure, since neither a correction for the ion gauge sensitivity, nor for geometric effects were made.

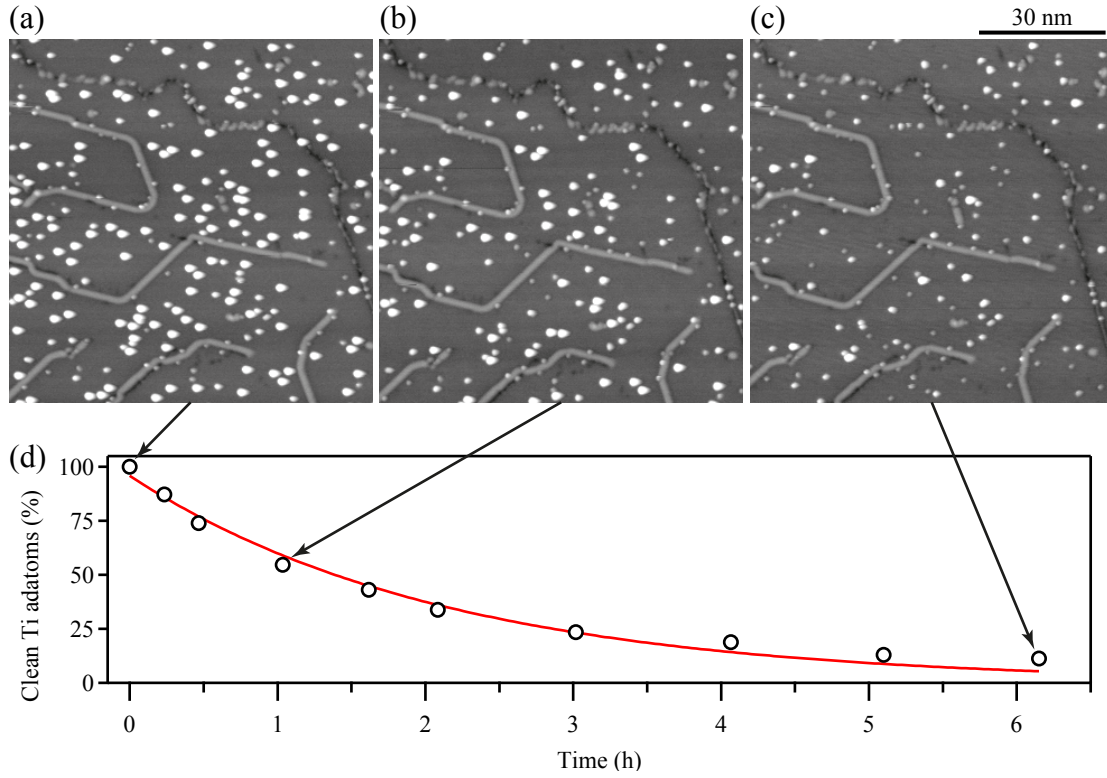


Figure 3.25: Partial pressure determination by recording the abundance of high Ti adatoms at 50 K versus time. (a) Most Ti adatoms are clean after deposition on *h*-BN/Ni(111). Situation after (b) 1 h and (c) 6 h. The total pressure during the time evolution is constant and about 5×10^{-11} mbar. (d) Fraction of clean Ti adatoms versus time. [$V_t = -100$ mV, $I_t = 10$ pA, and $\Theta = (4.1 \pm 0.2) \times 10^{-3}$ ML.]

3.3 Hydrogen related observations for Ti and Co adatoms

In this section we will briefly present and discuss hydrogen related phenomena that were encountered while measuring at elevated temperatures. In the first part we shall demonstrate the long time effect of measuring a sample at 50 K. We observe a curious surface dynamics that we were able to relate to the hydrogen partial pressure of the residual gas of our UHV system. Seemingly clean Ti adatoms were gradually hydrogenated. In the second part we will inspect a surface dynamics that emerged when the sample was heated beyond the boiling point of liquid helium. Finally, the here presented findings underline the importance of scrutinizing the UHV system for a possible hydrogen interplay, and advocates for the use of low temperatures in order to avoid a hydrogen interference.

The temporal evolution of Ti adatoms at 50 K is shown in Fig. 3.25. It depicts an ensemble of Ti adatoms on *h*-BN/Ni(111) shortly after dosing with the improved routine described in section 3.2.1. Consequently, most Ti adatoms are clean and imaged as 300 pm high protrusions, in agreement with the experiment at 4.7 K. With elapsing time a clear surface dynamics can be observed. We monitor the same surface region for six hours and plot the abundance of high Ti

adatoms versus time. After only one hour almost 50 % of the Ti adatoms are hydrogenated. Five more hours later one encounters only traces of high Ti adatoms. We recall the good residual pressure of the encircling UHV chamber of 5×10^{-11} mbar. Working under these conditions is generally assumed to be sufficiently good for observation times of a few hours for a sample in its clean state, and a co-adsorption of residual gas is often disregarded. However, the following analysis relates the temporal evolution to residual pressure. The corresponding particle impingement rate per unit area is:

$$\nu = \frac{p}{\sqrt{2\pi m k_B T}}, \quad (3.9)$$

where m , k_B , and T denote the molecular mass, the Boltzmann constant, and the residual gas temperature, respectively. By substituting the unit area with the number of Ni sites, we obtain the impingement rate per adsorption site and time of $R = \nu n_{\text{Ni}(111)} = 7.1 \times 10^{-5} \text{ s}^{-1}$, for $p = 5 \times 10^{-11}$ mbar, $n_{\text{Ni}(111)} = 5.377 \times 10^{-20} \text{ m}^2$ per site, $T = 50 \text{ K}$, and hydrogen molecules, respectively. In a second step we analyze the exponential reduction of clean Ti adatoms over time in Fig. 3.25(d), and obtain a decay constant of $\tau = (1.30 \pm 0.08) \times 10^{-4} \text{ s}^{-1}$. We can view the latter as a hitting probability per site and unit time via²³ $a = 1 - \exp(-\tau) = (1.30 \pm 0.08) \times 10^{-4} \text{ s}^{-1}$. The parameters R and a can both be interpreted as an impingement rate per site and unit time. If we now substitute R with the value of a , we can calculate the corresponding residual pressure that is responsible for the Ti adatom transformation with Eqn. 3.9 as $p = (9.2 \pm 0.6) \times 10^{-11}$ mbar. This pressure can be compared to the readout of our ionization gauge, if the hydrogen ionization gauge sensitivity factor of about 0.5 [41, 3] is considered. This is because the pressure readout of a nitrogen calibrated ionization gauge underestimates the true hydrogen pressure by this factor. The pressure derived from the evolution of clean Ti adatoms and the pressure readout of the ionization gauge are thus comparable. In this analysis, however, two more issues should be alluded. The first is the thermal transpiration factor between the poorly connected volumina of the surrounding UHV chamber and the inner volume of the cryostat. The pressure values of both volumina could actually differ by the factor $\sqrt{T_{\text{in}}/T_{\text{out}}}$, where T_{in} and T_{out} denote the gas temperature inside the cryostat and at the ionization gauge, respectively. The second issue is the hydrogen dissociation at the Ti host adatom. While one atom is clearly attached to the Ti adatom, the destiny of the other is less well known. The latter H atom might migrate about the surface and stick to an unoccupied Ti adatom. This mechanism would reduce the effective impingement rate by a factor of two. If all the above considerations were respected, an ionization gauge readout of $(5.6 \pm 0.4) \times 10^{-11}$ mbar would be deduced from the exponential decay of clean Ti adatoms over time, and the following numeric values: $R = a/2 = 6.5 \times 10^{-5} \text{ s}^{-1}$, $\sqrt{T_{\text{in}}/T_{\text{out}}} = \sqrt{6}$, and 0.5 for the ionization gauge sensitivity. One can therefore reconcile the reduction of the clean Ti adatom species over time by assuming that one hydrogen molecule arriving directly on a Ti atom dissociates and leaves one H atom on the Ti and the other flies off, *i.e.*, the latter is migrating about the *h*-BN surface until it is captured by a neighboring Ti adatom. We note that hydrogen molecules directly hitting the *h*-BN layer are scattered back into the vacuum without

²³Note that for small values of the decay constant $a \approx \tau$.

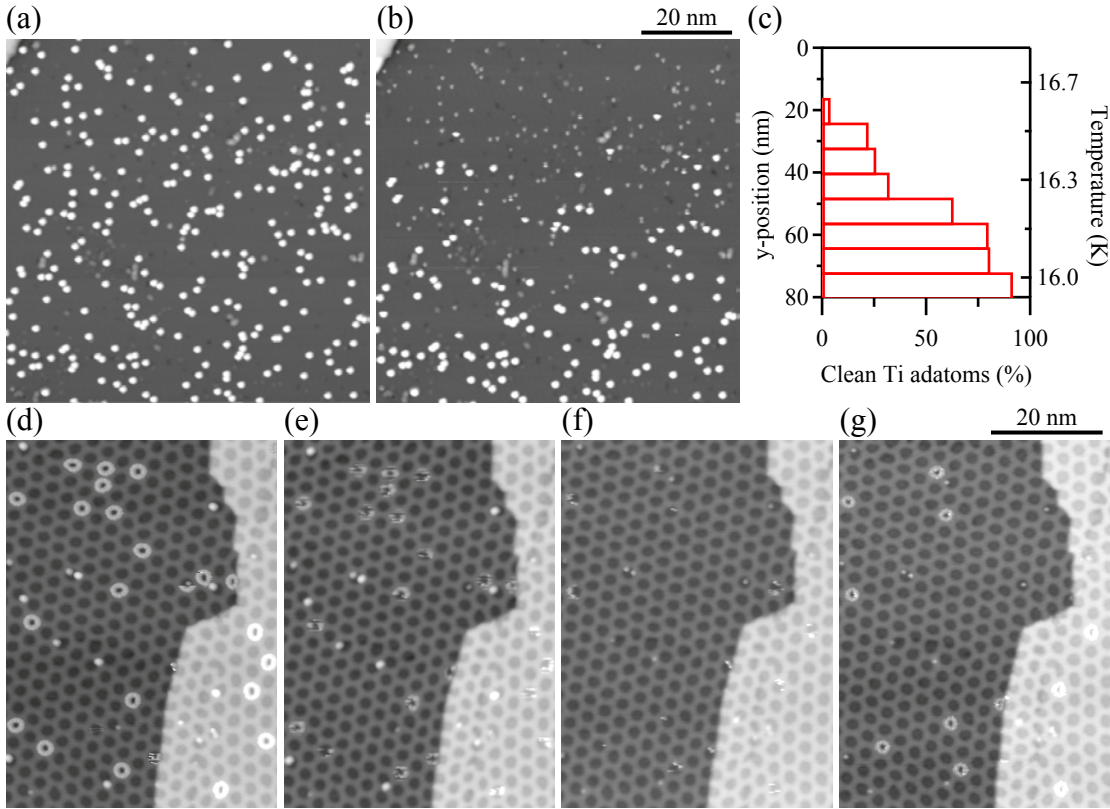


Figure 3.26: (a) A sample with mostly clean Ti adatoms on *h*-BN/Ni(111) measured at 4.7 K. (b) The same surface region measured at a transition temperature of 16.3 K that turns Ti adatoms into the low apparent height, *i.e.*, hydrogenated state. (c) Evolution of the fraction of clean Ti adatoms as a function of the *y* position of the scan and temperature, respectively. (d)-(g) Co ring and dot evolution on *h*-BN/Rh(111) as a function of temperature measured at (d) 4.7, (e) 15, (f) 23, and (g) 38 K. Co rings start to wiggle, disappear, re-appear and are finally re-stabilized with increasing temperature. Figure 3.27 shows the corresponding pressure evolution with temperature. [(a)-(b) $V_t = -100$ mV, $I_t = 20$ pA, and $\Theta = (3.4 \pm 0.1) \times 10^{-3}$ ML, (d)-(g) $V_t = -100$ mV and $I_t = 10$ pA].

interfering with clean Ti atoms. Only for sample temperatures as low as 10 K will physisorbed hydrogen be observed. The related $(\sqrt{3} \times \sqrt{3})R30^\circ$ hydrogen superstructure shows fascinating properties and is presented in the outlook of section 5.2.

The temperature dependence of clean Ti adatoms, deposited at 10 K, was studied starting at liquid helium temperature. Once the cryogen is completely boiled off, the temperature raises with 2.3 mKs^{-1} , which is sufficiently slow to enable drift-compensation and therefore to stay on the same microscopic surface spot in a temperature range of 4.7–43 K. Note that the temperature is measured at the cryostat and that the sample temperature is slightly lower due to finite thermal contact between the cryostat and the STM. The temperature evolution of the number of clean versus hydrogenated Ti atoms is shown in Fig. 3.26. In the initial state 98 % of the atoms are clean Ti and only 2 % are hydrogenated, see Fig. 3.26(a). For temperatures

that hydrogen is responsible for the observed Ti adatom behavior. Other gases ought to desorb at a different temperature. The warming up of the cryostat ultimately leads to the pressure evolution reminiscent of a temperature programmed desorption spectroscopy (TDS) [112, 69]. The surface under test is here, however, the gold plated copper wall of the cryostat. Since the latter is not a single crystal surface, as typically investigated by TDS, a distribution of adsorption sites with different adsorption energies is expected. We therefore apply the method of Barrie [15] to our pressure data by fitting the latter to a normal distribution with parameters $(\mu \pm \sigma) = (18 \pm 4)$ K that ultimately yield the desorption energy distribution of (52 ± 11) meV, if the simplified assumptions of a constant attempt frequency of 10^{13} Hz, and a coverage independent adsorption energy are made. In the view of the available TDS resolution and the slow heating rate β , that may allow for hydrogen re-adsorption, this low mean adsorption energy has to be treated cautiously. Nonetheless, such a low adsorption energy reflects the weak bonding nature of hydrogen to the Au plating and is suggestive of a physisorbed molecular state. In the limits of the available resolution, we note the approximately constant peak temperature which is independent of the coverage. This would indicate a first order desorption process [112, 69], in agreement with the assumption of physisorbed hydrogen molecules. In the aforementioned analysis a first order desorption was assumed.

As the desorbing hydrogen increases the pressure inside the cryostat volume, a steadily growing number of molecules hit and interact with the sample surface as is observable with STM [cp. Fig. 3.26]. This dose can be calculated by integrating the surface impingement rate $R(T)$ [cp. Eq. 3.9] in the considered temperature interval $[T_0, T_E]$:

$$D = \int_{t_0}^{t_E} R(t) dt = \beta \int_{T_0}^{T_E} R(T) dT, \quad (3.10)$$

where the D is expressed in langmuir equivalents. With the expression $1 - \exp(-D)$ one can finally estimate the fraction of hit surfaces sites in the course of dosing D L hydrogen. The integration of curve □, for instance, yields a dose of 2.6 L and concomitantly 93% of all surface sites have been hit during the temperature rise from 5 to 35 K. For the fast switching of Ti adatoms at 16 K, an equal or larger amount has to hit the sample within only 0.5 K [cp. Fig. 3.26(b)]. We recall that the above analysis is, of course, strictly valid only for the external part of the cryostat and does not adequately describe the conditions the sample is subject to. In fact, owing to the bad connection to the surrounding UHV vessel, a hydrogen desorption will necessarily result in a higher pressure inside the cryostat. A simple estimate shows that the pressure difference can amount to several orders of magnitude when considering the physical dimensions of the cryostat. By way of example, pre-covering the internal cryostat walls (500 cm^2) by 1/100 ML hydrogen can amount to a partial pressure inside the 1 l volume of the cryostat of 2.6×10^{-5} mbar, if a gas temperature of 20 K and no leaking out to the UHV vessel was assumed. The fast switching thus already occurs at the leading edge of desorption and explains why the transition temperature slightly shifts from one experiment to another.

4 Graphene

The realization of a carbon based field effect transistor by Novoselov, Geim, and co-workers [97] initiated a tremendous increase in research activities in the study of this two dimensional (2D) material, and stimulated the development of growth recipes for large areal quantities of high quality graphene (g). One of the essential breakthroughs was the realization of a truly two dimensional crystal with distinct transport properties that could only be described by 2D theories. Soon after this initial achievement, a whole series of related 2D materials could be exfoliated and equally cleaved down to the thickness of one atomic sheet with adhesive tape [98]. Among these were hexagonal boron nitride and molybdenite [98]. The latter material earned a lot of attention as it could soon have important applications due to its direct bandgap that allowed the realization of a MoS₂ based transistor [111]. Although graphene has high charge carrier mobilities, it is devoid of a sizeable band gap that would permit the fabrication of integrated circuits analogous to silicon based devices. A whole branch of research therefore strives to detect ways of modifying this zero band gap semiconductor, in a field of research referred to as band gap engineering. An interesting method to introduce a band gap consists in creating graphene nano ribbons (GNR) that inherit semi conducting properties through edge effects and lateral confinement [14, 145, 59]. An example of a bottom-up approach realization of such GNR is the assembly of molecular precursors into one dimensional linear chains in a work by Cai *et al.* [31]. Among the alternative methods of band gap engineering are, the introduction of a periodic potential through the adsorption of graphene on a lattice mismatched surface [136, 105, 24], and the adsorption, respectively, intercalation of elements [135, 57]. The graphene band gap of the former approach can be reinforced by the adsorption of a metal island superlattice [115], and can further be enhanced by sodium adsorption on this metal island superlattice [104, 91].

Our works concerning mono and double layers of graphene recently appeared in the issues of *J. Phys.: Condens. Matter* **24**, 314203 (2012) [91], and in *ACS Nano* **6**, 9299 (2012) [103]. The former is included in this version of the manuscript for completeness. Here, we will summarize the highlights and outline the author's contribution to this work.

Disregarding the popular approach of mechanically exfoliating graphene from highly oriented

pyrolytic graphite (HOPG) with adhesive tape [97, 98], the methods to grow graphene now rather include the exposure of hydrocarbon containing precursor molecules to a catalytically active surface at high temperature. We have reviewed in our contribution [90, 91] four growth methods for single crystals of ruthenium that rely on segregation of bulk dissolved C impurities and ethylene precursors as a carbon source. We scrutinized the individual methods for their resulting layer quality [90, 91]. On Ru(0001), the *g* sheet adopts the characteristic *g*/Ru(0001)-(23 × 23) moiré pattern [82, 81, 84]. The moiré structure arises from the beating of the two superimposed lattice planes of Ru(0001) and of graphite that produce a moiré periodicity of about 3 nm [80, 136, 140]. For the case of *g*/Ru(0001) one orientational domain is predominant and emerges due to the rotation of the lattice planes by 0.5 ° [23]. The moiré structure is not only an optical effect but also reflected in the electronic [136, 64, 23] and geometric properties of the structure. Notably, the vertical corrugation of around 1 Å [81, 64] follows the moiré periodicity and is furthermore also partially transferred to the underlying Ru substrate with a lateral shift of one half moiré period [81]. Minute deviations of the local lattice parameters or in their orientation entail strong variations in the resulting moiré pattern [93] with an immediate impact on the respective STM topography. The perfection of the moiré pattern can therefore serve as a fingerprint of its constituting lattice quality. The moiré patterns of the inspected samples were tested with respect to their moiré long-range order in the present contribution [90, 91]. The figure characterizing the long-range order was extracted from the decay length of the two dimensional autocorrelation function that was calculated for every sample surface. The 2D autocorrelation was determined with the software *ImageJ* [1]. Missing ripples in the moiré pattern, or wrong alignment due to a relative translation of coalescing graphene patches will hamper the resulting long-range order and consequently suppress the corresponding decay length. The best long-range order for graphene was found for a combination of chemical vapor deposition (CVD) and segregation.

The hydrocarbon precursor was ethylene (C₂H₄), either exposed to the hot sample in a CVD, or at room temperature in a temperature programmed growth (TPG) approach. In the CVD case, a partial pressure of ethylene was dehydrogenated at the Ru surface held at 1100 or 1650 K. The latter temperature yielded particularly high *g* qualities with a decay length of 130 Å, as compared to 70 Å for the lower temperature [91]. The accompanying high temperatures, however, resulted in a gradual loading of the Ru bulk with interstitial carbon [128] owing to the increased C solubility at these high temperatures [5]. By way of example, the C solubility in Ru is six times higher at 1540 K than it is at 1000 K [5]. Segregation and CVD were combined [128] and yielded the best *g* qualities with a decay length of 240 Å [91]. The approach was to expose the Ru crystal at high temperatures to an ethylene partial pressure and thereby to load the crystal, followed by a very slow cooling that drives the interstitial carbon back to the surface as a result of the steadily reduced solubility at decreasing temperature [5]. We need to recall that the bulk of a commercially purchased Ru crystal is sufficiently enriched by C impurities that *g* can be grown by simply heating the sample [142]. However, since other impurities than carbon co-segregate, the resulting *g* quality will be reduced. Furthermore, great efforts are made in order to deplete a newly bought crystal from impurities by extended cycles of

sputtering, annealing in oxygen, and flash to high temperature. If such a sample is loaded with C, only this impurity can segregate to the surface with the concomitant superior qualities just described. However, the coverage control of the latter method is more elaborate, since multiple layers are easily nucleated by segregation [127, 103].

A further interesting approach is TPG, in which the room temperature exposure of ethylene molecules is followed by a dehydrogenating flash [13, 95, 63, 71, 136]. In this growth mode, small separated graphene islands will be nucleated with a total aerial ratio corresponding to the saturation coverage of the respective precursor molecule. For ethylene, one room temperature deposition and flash cycle will result in a graphene coverage of approximately 25 % [95, 62, 71, 72, 55]. Note that the sticking coefficient for molecules is low at the graphene interface, and the catalytic activity reduced by orders of magnitude, *i.e.*, an analogous effect as prevailing on the surface of HOPG. This recipe is particularly valuable, since it allows to asymptotically grow a complete layer of graphene by repeated TPG cycles. An accompanying disadvantage of this method is, however, the high abundance of defects that evolve from coalescing graphene patches if numerous TPG cycles are employed, owing to the many translational domains present. Nonetheless, the TPG approach is powerful in that sequential growth is limiting the co-segregation of bulk dissolved carbon impurities that accompanies extended high temperature treatments with slow cooling of the sample [128]. The latter tends to nucleate second layer graphene which is not always a desired effect. The practical use of the room temperature deposition and flash recipe is that the graphene islands are separated with the bare substrate exposed, which is in the present case Ru. For the case of highly reactive adsorbates, such as Ti, we have discussed in section 3.2.1 the potential use of a sample with islands that are separated by the exposed metal substrate. For the therein proposed scenario, the substrate would hinder a potential hydrogen diffusion from one graphene island to the next and thus prevent the hydrogenation of the Ti adsorbates located on top of an island.

The boundary dislocations were mentioned above as a drawback of the TPG method. We recall that they arise due to the translational misfit of neighboring graphene islands upon coalescence. A recent development is the engineering of graphene defects to investigate the emerging and intriguing transport properties caused by line and point defects, as was reviewed by Banhart and co-workers [11]. The aforementioned downside of TPG could thus turn out to be an effective advantage, and may allow the convenient creation of g defect lines.

Two distinct STM were used in the study of graphene growth. The first is an STM at the EPFL [75], and the second an STM at the APE beamline [102] at the ELETTRA synchrotron facility. The latter allowed to carry out angle resolved photo electron spectroscopy (ARPES) measurements and STM characterization of the very same sample. The sample could be permanently kept in UHV, since the transfer from the ARPES to the STM chamber can be realized without breaking the UHV. This implies that no additional sample treatment¹ had to be carried out in between ARPES and STM measurements. It is essential to dwell on the true implications of measuring the very same sample by ARPES and STM. The Ru crystal

¹Since the sample was not exposed to air, no flash desorption was required.

is particularly sensitive to preceding graphene growth cycles, *i.e.*, the preparation history influences the resulting graphene layer [91]. This means that a developed growth recipe for one Ru crystal is poorly transferable to another sample. The reason is the participation of bulk dissolved carbon impurities in the process of graphene growth. The hydrocarbon precursor molecules are dehydrogenated in CVD at the catalytically active surface and enrich not only the latter but also the Ru bulk with carbon [128] as was mentioned above. The resulting graphene layer might not only have a different quality than the initially intended CVD recipe, but also have nucleated an undesired second layer graphene [127, 103]. Applying the apparently same growth recipe on two distinct crystals, with their different preparation histories, can therefore result in graphene surfaces that have little to none in common. A critical situation occurs, if two crystals are prepared at two geographically separated labs, and the experimental properties of both samples are treated as if they were related. To a smaller extent, the same holds for a sample that is prepared in lab A and subsequently transferred to lab B for a complimentary inspection. In this case, the sample had typically been exposed to ambient conditions and needed to undergo a heat treatment to clear the surface of adsorbates before the measurement could be carried out. The heat treatment, however, might modify the sample properties as mentioned above, and the following characterization is consequently again realized for a different sample. One of the few possibilities to truly correlate topographic features, deduced with STM, to ARPES data, is to carry out both types of measurements on the very same sample. We have done the latter in the study of the two distinct bilayer phases of graphene on Ru(0001) [103].

The author performed the experiments for $g/\text{Ru}(0001)$, analyzed the data, and wrote the corresponding part of the manuscript of Refs. [90, 91]. For the recent contribution of Ref. [103] he performed the STM measurements at the ELETTRA synchrotron facility in collaboration with J. Fujii, and determined the areal quantity of second layer graphene for the respective sample preparations.

Optimizing long-range order, band gap, and group velocities for graphene on close-packed metal surfaces

F D Natterer¹, S Rusponi¹, M Papagno², C Carbone² and H Brune¹

¹ Institute of Condensed Matter Physics (ICMP), Ecole Polytechnique Fédérale de Lausanne (EPFL), CH-1015 Lausanne, Switzerland

² Istituto di Struttura della Materia, Consiglio Nazionale delle Ricerche, Basovizza, Trieste, Italy

Received 24 December 2011, in final form 6 February 2012

Published 20 July 2012

Online at stacks.iop.org/JPhysCM/24/314203

Abstract

We compare different growth methods with the aim of optimizing the long-range order of a graphene layer grown on Ru(0001). Combining chemical vapor deposition with carbon loading and segregation of the surface layer leads to autocorrelation lengths of 240 Å. We present several routes to band gap and charge carrier mobility engineering for the example of graphene on Ir(111). Ir cluster superlattices self-assembled onto the graphene moiré pattern produce a strong renormalization of the electron group velocity close to the Dirac point, leading to highly anisotropic Dirac cones and the enlargement of the gap from 140 to 340 meV. This gap can further be enhanced to 740 meV by Na co-adsorption onto the Ir cluster superlattice at room temperature. This value is close to that of Ge, and the high group velocity of the charge carriers is fully preserved. We also present data for Na adsorbed without the Ir clusters. In both cases we find that the Na is on top of the graphene layer.

(Some figures may appear in colour only in the online journal)

1. Introduction

Graphene (g) is a 2D honeycomb lattice made of carbon atoms with the conduction electrons in sp^2 -hybridized Bloch states. Its exceptional charge carrier mobility and optical transparency of 98% make graphene an ideal material for fast transistors [1], and for top electrodes for solar cells. These exciting and potentially useful properties of graphene are delicate functions of the structural and chemical defect density [2] and thus strongly depend on the quality of the graphene layer. On the other hand, for the creation and implementation of reliable devices, a reproducible graphene production process for large areal quantities is required [3–5]. A major effort is therefore devoted to simultaneously satisfying the two fundamental key issues: the production of defect free graphene and the scalability and transferability of the chosen preparation process. In this sense, albeit high quality, the popular method of mechanically exfoliating graphene sheets from highly oriented pyrolytic graphite with adhesive tape [6] has to be disregarded due to its impracticality beyond prototyping. The alternative

and scalable approaches rely on a supporting substrate that catalyzes and seeds graphene growth. One often considered method consists in exposing an atomically clean single crystal surface to a hydrocarbon gas partial pressure and heat treatment to induce pyrolysis of the molecules in temperature programmed growth (TPG) or chemical vapor deposition (CVD). While low temperature chemisorption of hydrocarbon molecules is followed by flash annealing [7–14] in the first case, the latter approach involves high temperature exposure of hydrocarbon molecules to the catalytically active substrate [3–5, 15–18]. The pyrolysis of the hydrocarbon molecules enriches the substrate surface with carbon adatoms to finally yield graphene. Alternatively, surface segregation of bulk dissolved carbon impurities [18–23] or molecular beam epitaxy from high purity carbon rods at elevated temperatures [24] can also be employed. We discuss four of these growth techniques for the case of a Ru(0001) substrate [25] with special focus on the resulting long-range order, expressed in terms of the autocorrelation length that is a finger-print of the structural quality of graphene. ⁶¹

A related, and for applications equally relevant, issue is the ability to engineer the graphene electronic properties. Close to the K-points of the Brillouin zone, the bands have a linear dispersion that is well described by the relativistic Dirac equation for massless neutrinos. The resulting Dirac cones of the conduction and valence bands touch each other at the Dirac point located at the Fermi level E_F . Therefore free-standing graphene is a zero-gap semiconductor. However, most electronic device applications require a band gap. Theory has suggested that a gap may derive from an external long-range periodic potential [13, 26, 27]. Such a potential is created when adsorbing graphene onto a lattice mismatched close-packed metal surface. The resulting moiré structures exhibit periodic stacking alternations where either one of the two C atoms in the unit cell is localized on top of a metal atom, or both C atoms are adsorbed on substrate hollow sites. The binding of graphene to the substrate has a significant van der Waals contribution; however, in the on-top stacking areas a hybridization of graphene π and metal d states can be established. This inhomogeneous binding induces a weak corrugation in the electron potential with the period of the moiré pattern which is manifested in a small band gap. This corrugation can be reinforced by adsorbing metal clusters on top. For Ir clusters on g/Ir(111) an sp^3 hybridization with the metal has been reported [28]. This re-hybridization is localized at the graphene areas covered by clusters, since only there can one of the two C atoms of the unit cell hybridize with a cluster Ir atom above and the other with a substrate Ir atom below. We show the experimental realization of this concept of band gap engineering for equidistant Ir clusters grown on g/Ir(111) [29]. Alternative methods of inducing band gaps in graphene layers ranging from a few tens to a few hundreds of meV are patterning [30–33], adsorption [34–36] and intercalation of suitable elements [37, 38], strain [39] or substrate induced symmetry breaking [40, 41]. However, most of these methods have the drawback of producing a flattening of the Dirac cone and thus a reduction of the electron group velocity, an effect which should be minimized for graphene applications in electronic circuits since a high group velocity is the necessary condition for high carrier mobilities. We further show the ability of tuning the graphene electronic band gap by adsorbing alkali metals on top of graphene [42]. Sodium adsorption on bare graphene (Na/g) and on a well ordered superlattice of Ir clusters on graphene (Na/Ir/g) on Ir(111) produces very large band gaps while preserving the shape of the Dirac cone and thereby the high electron group velocity.

2. Experiment

The presented measurements were performed with a homemade scanning tunneling microscope (STM), operating at room temperature and at a base pressure below 5×10^{-11} mbar [43]. All listed pressure values state the readout of a N_2 calibrated cold-cathode gauge without correcting for the respective hydrocarbon or process gas sensitivity. The STM images were acquired in the constant current mode and with an electrochemically etched W tip.

The indicated tunnel voltages V_t correspond to the sample potential. Our Ru(0001) single crystal was cleaned by repeated cycles of Ar^+ ion sputtering (first 300 K, 30 min, then 1030 K, 15 min, $1.5 \mu A cm^{-2}$, 1.2 kV), annealing in oxygen (1030 K, 8 min, 8×10^{-8} mbar) and flash to 1650 K. Cleanliness of the Ru surface was checked with STM and the stated cleaning routine repeated if required. The carbon source was either ethylene (C_2H_4) introduced into the UHV system via a leak-valve or dissolved bulk carbon impurities as will be detailed later.

The Ir(111) crystal was prepared by repeated cycles of Ar^+ ion sputtering at room temperature and at 1000 K, followed by annealing to 1500 K. The graphene layer was grown by exposing the Ir(111) surface at 1300 K to ethylene [15, 16]. For the ethylene pressures and exposures used CVD growth is self-limiting and only a single graphene layer forms, which we confirmed by angle-resolved photoelectron spectroscopy (ARPES). The Ir cluster superlattice was grown by evaporating 0.15 ML Ir (one monolayer, ML, is defined as one atom per Ir substrate atom) at a substrate temperature of (375 ± 25) K. Under these conditions, exactly one Ir cluster with a mean cluster size of 13 atoms is formed per hcp region of the g/Ir(111)– (9.32×9.32) moiré [12, 16]. Ir was evaporated from a current heated thin film plate with a cross section of $0.5 mm \times 0.1 mm$. The deposition flux was adjusted to $2.0 \times 10^{-4} ML s^{-1}$ and calibrated by the core level intensity measured for Ir deposition on a Ag(111) crystal. This calibration was cross-checked with STM in a different UHV chamber. Sodium was evaporated from a commercial getter source (SAES) onto the sample held at room temperature. ARPES data were collected at the VUV beam line of the ELETTRA synchrotron radiation facility in Trieste with a photon energy of 120 eV. This energy is close to the Cooper minimum of the photoionization cross section of the Ir 5d states and thereby minimizes the Ir background photoemission signal with respect to the graphene states. ARPES spectra were recorded at a sample temperature of 100 K with a Scienta R-4000 hemispherical electron analyzer which allows spectra to be recorded simultaneously within an angular aperture of 30° .

3. g/Ru(0001)

The chemisorption of a saturated monolayer (ML) of ethylene onto Ru(0001) at room temperature, followed by thermal dehydrogenation at 1100 K, gives rise to the graphene islands visible on the atomic substrate terraces in figure 1(a). The periodic pattern resolved in the islands is the (23×23) moiré structure [44–46] caused by the lattice mismatch between the Ru substrate and the graphene layer. On Pt(111), the chemisorption of a saturated layer of ethylene at 300 K leads, after pyrolysis, to a coverage of 0.25 ML [8, 10, 47, 48]. On Ru(0001) we measured after one chemisorption and annealing cycle a graphene coverage of $\Theta = (0.23 \pm 0.05)$ ML, in agreement with this value. A second TPG cycle leads to a coverage of (0.43 ± 0.05) ML and triggers coalescence of graphene islands, as seen in figure 1(b).

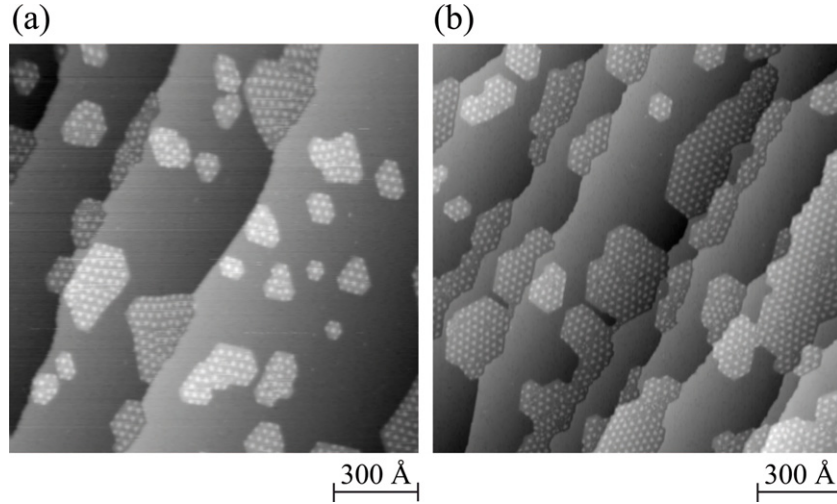


Figure 1. Graphene growth by chemisorption and dissociation cycles of ethylene on Ru(0001). (a) STM constant current image after the first cycle, leading to a $\Theta = 0.23$ ML. (b) STM image after the second step, showing $\Theta = 0.43$ ML (one cycle consists of exposure to 5 L C_2H_4 at $T_{\text{ads}} = 300$ K, dissociation and H_2 desorption at $T_{\text{diss}} = 1100$ K, STM parameters $V_t = -1.0$ V, $I_t = 316$ pA, $T = 300$ K).

Since there are many translational domains of the moiré structure, island coalescence leads with a high probability to domain walls. In contrast to g/Ir(111), where the domain walls can be removed by annealing [15], we observe that they stay on Ru(0001). This is attributed to the stronger binding of g to Ru(0001) [44, 49, 50] than to Ir(111) [51], where the weaker substrate interaction enables diffusion of entire islands in a Smoluchowski ripening process [15]. A third TPG cycle leads to (0.54 ± 0.05) ML. Therefore the coverage as a function of the number of cycles n is described by $\Theta = 1 - (1 - 0.24)^n$. This is the expected behavior for selective ethylene dehydrogenation on the catalytically active transition metal surface, whereas graphene has a low sticking coefficient to hydrocarbons and a negligible dehydrogenation activity [17]. As a consequence, graphene growth by sequential chemisorption and decomposition has the advantage of being self-limiting. One asymptotically approaches a single layer graphene and no second layer will grow. However, it suffers from the many domain walls limiting the long-range order. For Ru(0001) these domain walls cannot be removed by annealing.

In CVD graphene growth the Ru(0001) surface is exposed to ethylene at $T_{\text{CVD}} \geq 1000$ K. However, C dissolves into the Ru bulk, and, in addition, the solubility of interstitial carbon in ruthenium shows a strong temperature dependence—it is six times higher at 1540 K than at 1000 K [19]. In order to prevent diffusion into the bulk, as well as surface segregation of already dissolved C, CVD growth has to be performed at not too high a temperature and the sample temperature has to be rapidly quenched afterwards. Both requirements are somewhat in contradiction with best order. For the quench the best compromise is $\dot{T} = -7$ K s^{-1} , and the influence of the growth temperature is illustrated in figure 2. In both cases there is a single monolayer of graphene and it is evident from visual inspection that the higher exposure temperature leads to better long-range order. This is quantified by determining

the exponential decay lengths of the 2D autocorrelation functions³. We find an autocorrelation length of $\Lambda = (131 \pm 8)$ Å for $T_{\text{CVD}} = 1650$ K, while $T_{\text{CVD}} = 1100$ K leads to $\Lambda = (68 \pm 12)$ Å. When disregarding the bulk solubility, CVD is also self-limiting since we find that growth of the second monolayer requires significantly higher exposures. The delicate issue with CVD growth is the bulk solubility at the temperature giving best order. This can be turned into an advantage, as shown below; however, it renders control on the graphene coverage more difficult.

The third growth method combines CVD surface growth with deliberate loading of the surface region with carbon which is then segregated by a very slow cool down [22]. By optimizing the parameters, we achieved very well ordered graphene layers, as seen in figure 3(a), with an autocorrelation length of $\Lambda = (238 \pm 12)$ Å. The superior long-range order is the most prominent argument for this technique. However, one needs to keep track of the coverage as multiple layers may be nucleated if sufficient interstitial carbon has been created before [52].

The fourth growth technique is the mere segregation of Ru bulk dissolved carbon impurities. The amount of C present in commercial Ru crystals suffices to create relatively well ordered graphene layers for a large number of experiments by a flash to $T = 2000$ K [20]. However, in comparison to the third method, one encounters the complication of co-segregation of elements other than C, which may lead to structural imperfections in the graphene layer, such as point or substitutional defects [53]. After many sputter, oxygen glowing and flash cycles, the Ru becomes entirely clean [20] and then one may load it with only C in the way described above. When a sample is frequently used for CVD some of the C is dissolved and gradually accumulated in the bulk such

³ The spatial 2D autocorrelation is defined as $ac_{i,j} = \sum_{k,l=1}^n z_{kl} \cdot z_{k+i,l+j}$, i.e., it multiplies the pixels of the image translated by i, k with the ones of the non-translated image.

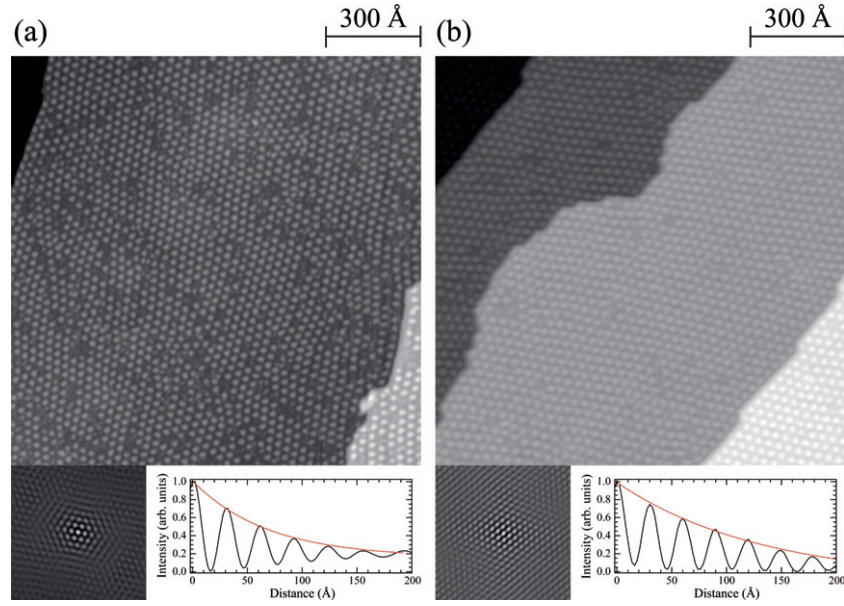


Figure 2. The temperature-dependent long-range order of graphene grown by ethylene CVD at (a) $T_{\text{CVD}} = 1100$ K (20 L) and (b) $T_{\text{CVD}} = 1670$ K (80 l). After exposure the temperature is held for 2 min and then lowered to room temperature with $\dot{T} = -7$ K s $^{-1}$. The lower left panels are 2D autocorrelation images and the lower right cuts through them show the exponential decay defining the autocorrelation length ($V_t = -1.0$ V, $I_t = 316$ pA).

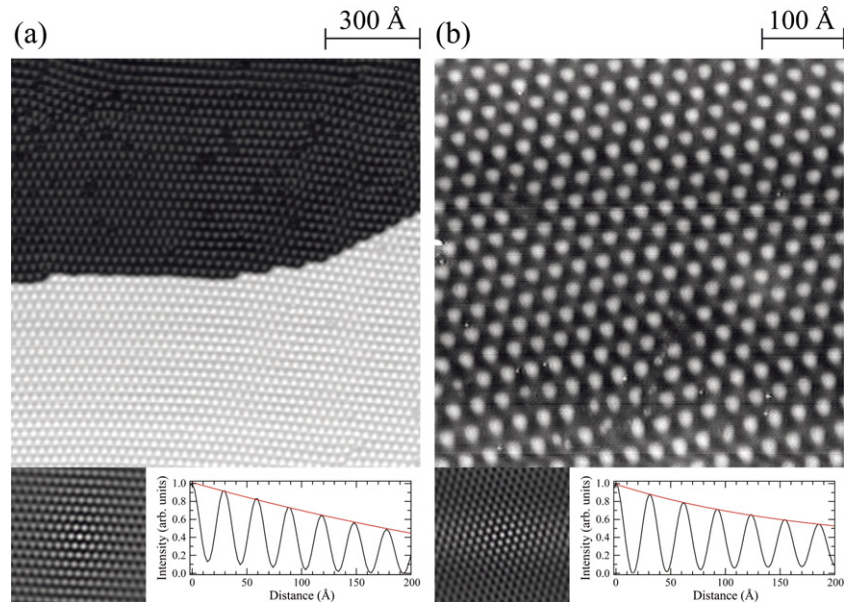


Figure 3. (a) The graphene layer with an autocorrelation length of $\Lambda = 238 \pm 12$ Å obtained from intentionally dissolving carbon into the bulk during CVD and its subsequent controlled surface segregation during slow cooling (127 L C $_2$ H $_4$ at $T_{\text{CVD}} = 1540$ K, $\dot{T} = -0.1$ K s $^{-1}$, $V_t = -1$ V, $I_t = 316$ pA). (b) Graphene growth during a short flash to $T = 1570$ K of a freshly prepared Ru surface due to surface segregation of the residual bulk dissolved carbon from previous graphene preparation cycles ($V_t = -0.88$ V, $I_t = 150$ pA).

that a flash might reveal the preparation history of the Ru crystal. Such a sample is shown in figure 3(b) exhibiting with $\Lambda = (174 \pm 10)$ Å very good long-range order. In table 1,⁴ various preparation methods are compared with respect to

their autocorrelation lengths for this and published work [13, 21, 52]. The best growth method for order is to combine CVD, carbon loading and segregation of the surface layer. This assessment can be rationalized as follows.

Concerted experimental [14, 17, 23, 24] and theoretical [54–56] effort has been devoted to addressing the graphene growth mechanism on transition metal surfaces. Once the thermal decomposition of the hydrocarbon molecule is complete, which happens at around $450 \text{ K} \leq T \leq 700 \text{ K}$

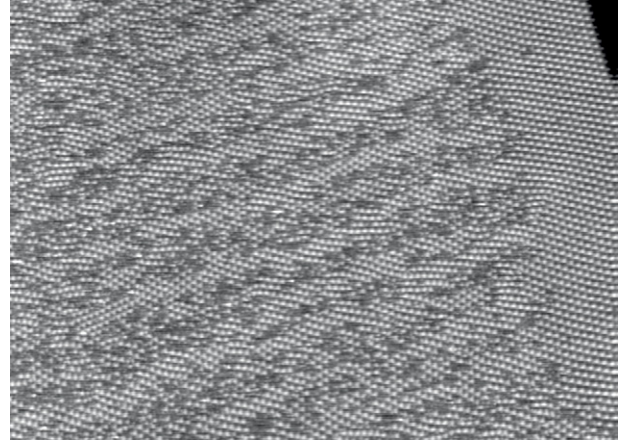
⁴ The literature autocorrelation lengths (Λ) have been determined for the largest terraces in the STM images of the respective publication. The gray-scale has been used as the z -value and it has been verified with our own data that this makes no difference within the error bars with respect to taking the real z -values, even if non-linear gray-scale tables have been applied.

Table 1. Comparison of autocorrelation lengths (Λ) obtained with different growth methods for graphene on Ru(0001) (see footnote 4).

Reference	Λ (Å)	Method
[13]	(59 ± 5)	TPG cycles
[21]	(76 ± 4)	Segregation
[52]	(157 ± 43)	CVD plus segregation
This work	(68 ± 12)	Low temperature CVD
This work	(131 ± 8)	High temperature CVD
This work	(238 ± 12)	CVD plus segregation
This work	(174 ± 10)	Long term preparation

[7, 8, 47], small carbon clusters reside on the surface. Only if the temperature is sufficiently high, $T \geq 700$ K [7, 47], will these carbon clusters start to form graphene islands [7, 47, 54, 55], given that a critical C adatom concentration is reached [17, 23, 24, 56]. Furthermore, it is now understood that graphene formation proceeds not via monomer attachment but rather through incorporation of a five carbon atom precursor molecule [17, 24, 56]. The stability of a graphene island is a complicated function of its size [55, 57]; particular cluster dimensions have an increased life-time [14] and exhibit varying electronic properties due to quantum confinement [58].

Interestingly, once larger graphene islands have nucleated, the structural quality of the resulting sheet is also determined by the speed of growth, i.e., the C adatom density [17, 23]. An example is shown in figure 4. This sample was prepared by keeping it for three more minutes after terminating the CVD growth at the growth temperature of 1100 K. In agreement with figure 2(a), the center of the graphene patch is poorly ordered; however, it is bound by a very well ordered stripe of 40 nm width. The ethylene partial pressure gradually decreases after closing the leak-valve and so does the C adatom density. The resulting lower growth speed leads to higher graphene quality. In the end, it is the delicate balance between the C adatom density, the formation of precursor C clusters, their attachment to existing graphene patches, the purity of the C source, as well as the rearrangement between growing graphene islands upon coalescence that decides the resulting graphene quality [17, 56]. The superior structural quality of the third growth method (CVD plus segregation) can now be rationalized. On the one hand, it relies on the cleanliness of the approach, which avoids co-segregation of bulk dissolved impurities other than carbon. On the other hand, the low C supersaturation at high temperature leads to a slow carbon attachment to existing graphene patches with the concomitant excellent structural quality. We finally note that graphene formation may through the high growth temperatures also lead to substrate faceting [59, 60]. Interestingly, the faceted regions provide especially well ordered graphene patches [7, 60], which could open a new route for more efficient growth of high quality graphene. The present results show the best long-range order for a combination of CVD growth and segregation.

**Figure 4.** The ordered stripe at the border of a disordered graphene patch grown on Ru(0001) by ethylene CVD at low temperature with 3 min post-annealing (1100 K, 20 L, $p_{C_2H_4} = 3.5 \times 10^{-7}$ mbar, 200×146 nm², $V_t = -1.0$ V, $I_t = 150$ pA).

4. g/Ir(111)

We now describe the effect of a periodic potential on the electronic band structure of graphene resulting from the moiré structure of g/Ir(111)– (9.25×9.25) [12, 15] and from its reinforcement by self-assembled Ir clusters grown on top [29]. For the first system mostly unperturbed Dirac cones at the K-points of the Brillouin zone, except for the opening of minigaps at the boundaries of the mini-Brillouin zone, have been reported [51]. Figure 5 shows STM images and ARPES intensities comparing both systems, revealing that the cluster superlattice potential induces a strong group velocity anisotropy together with a significant band gap opening [29]. We focus on the energy region close to the apex of the Dirac cone, and, since the linear dispersion of the π band is modified close to the Bragg planes, we restrict our analysis to energies $E - E_F > -0.5$ eV. In the presence of the superlattice the group velocities in the two directions are $v_{\Gamma K} = (4.90 \pm 0.06)$ eV Å and $v_{p\Gamma K} = (2.90 \pm 0.05)$ eV Å, corresponding to an anisotropy of $\Delta v/v_{p\Gamma K} = (70 \pm 5)\%$. This value is 12 times larger than the anisotropy expected for unperturbed graphene due to its trigonal warping. The tight-binding approximation up to third nearest neighbors (TB3 model) for free-standing graphene gives $\Delta v/v_{p\Gamma K} = 5\%$ [61]. The anisotropy for g/Ir(111) is, with $\Delta v/v_{p\Gamma K} = (16 \pm 2)\%$, larger than this, showing the small effect of the periodic potential resulting from the moiré alone. The group velocity renormalization is expected to be more effective for charge carriers moving perpendicular to the largest corrugation of the potential [26, 27]. In agreement, we find the strongest reduction for $p\Gamma K$.

The superlattice induced band gap opening can be derived by comparing the positions of the Dirac cone summits for both cases, and by making reasonable assumptions on the position of the Dirac point derived by carefully checking for charge neutrality. For g/Ir we find $E_\pi = (-70 \pm 20)$ meV, in good agreement with previous results [35]. The Ir cluster superlattice shifts the π summit down to $E_\pi = (-200 \pm 20)$ meV, while the π^* band stays above E_F . Following the

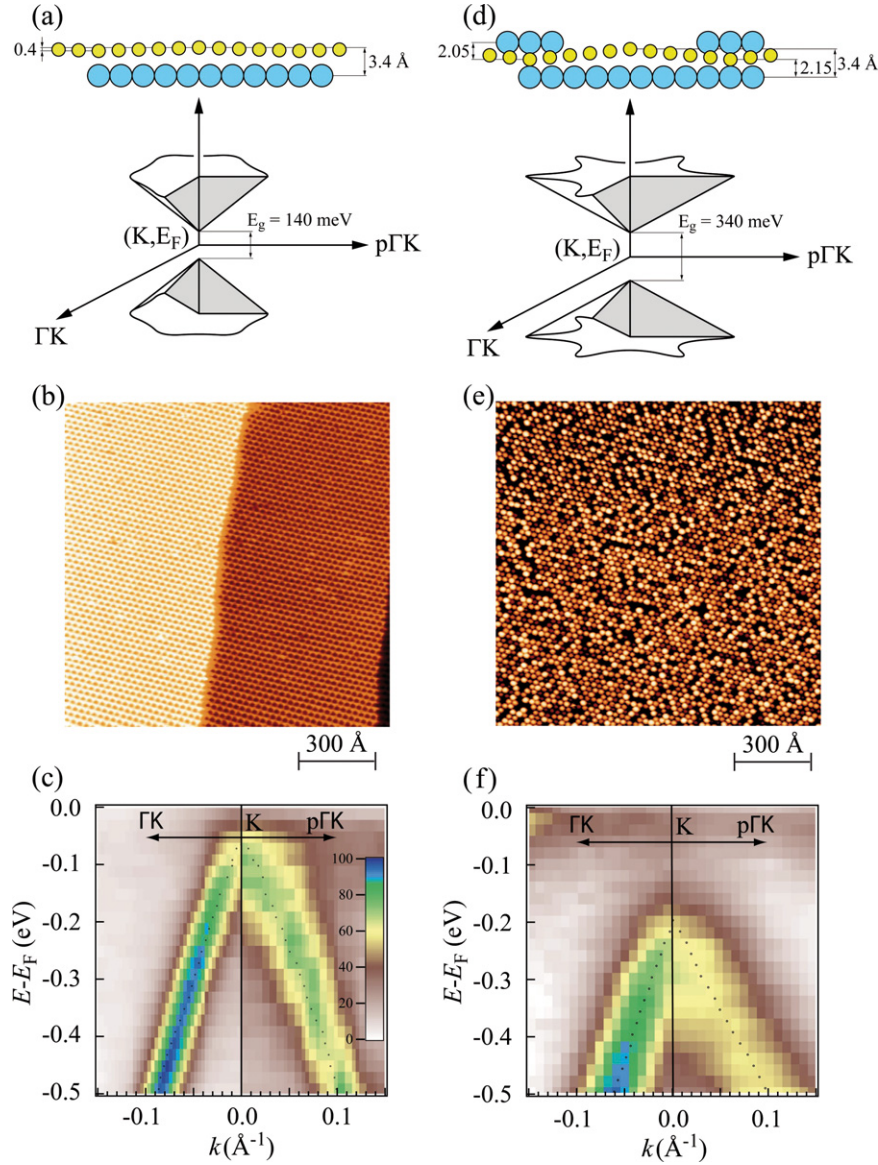


Figure 5. (a) Sketch of the $\pi(\pi^*)$ band for $g/\text{Ir}(111)$ close to the K-point and E_F . The Dirac cones are almost symmetric and only a small gap opens at the K-point. (b) STM image of the moiré structure of $g/\text{Ir}(111)$. (c) ARPES intensity of the π band of $g/\text{Ir}(111)$ around the K-point and along the ΓK direction and perpendicular to it. (d) Sketch of the $\pi(\pi^*)$ band for $\text{Ir}/g/\text{Ir}(111)$. The cluster superlattice induces a strong anisotropy in the Dirac cones and the opening of a large gap at the K-point. (e) STM image of an Ir cluster superlattice grown on $g/\text{Ir}(111)$ ($\theta = 0.15$ ML, $T_{\text{dep}} = 375$ K). (f) ARPES intensity of the π band for $\text{Ir}/g/\text{Ir}(111)$ around the K-point and along the ΓK direction and perpendicular to it. In (c) and (f) the dots represent the peak positions of the momentum distribution curves.

literature [28, 35], we assume charge neutrality for $g/\text{Ir}(111)$ and find $E_{g,g/\text{Ir}} = (140 \pm 40)$ meV. For the cluster lattice a possible charge transfer can be estimated from the core level and conduction band shifts. We find that these shifts are very small. The C 1s level shifts down by (30 ± 30) meV and the top of the σ band at the M-point of the second Brillouin zone by the same amount. With $E_D = -30$ meV we find $E_{g,\text{Ir}/g/\text{Ir}} = 340$ meV.

Further tuning of the graphene electronic bands can be achieved by chemisorption of alkali metals at room temperature. For Na adsorption on bare graphene (Na/g) we observe a band gap of $E_{g,\text{Na}/g/\text{Ir}} = 320$ meV, whereas in the case of Na adsorption on the Ir cluster superlattice the band gap reaches $E_{g,\text{Na}/\text{Ir}/g/\text{Ir}} = 740$ meV (see figure 6(a)) [42],

which is very close to the band gap of conventional semiconductors. Remarkably, the formation of these very large band gaps preserves the shape of the Dirac cone and the high electron group velocity. Due to strong electron charge transfer from Na to graphene, the π^* state is shifted below E_F as compared with bare graphene on $\text{Ir}(111)$. From the constant dE/dk gradient of the band dispersion of the π^* states we evaluate the electron group velocities to $v_{\text{Na}/g/\text{Ir}} \approx 5.5$ eV Å and $v_{\text{Na}/\text{Ir}/g/\text{Ir}} \approx 5.2$ eV Å, respectively. These values are very close to the ones obtained by third nearest neighbor tight-binding calculations [61] and in magneto-transport measurements of free-standing graphene.

Figure 6(b) shows a schematic summary of the evolution of the graphene band gap as a function of the applied

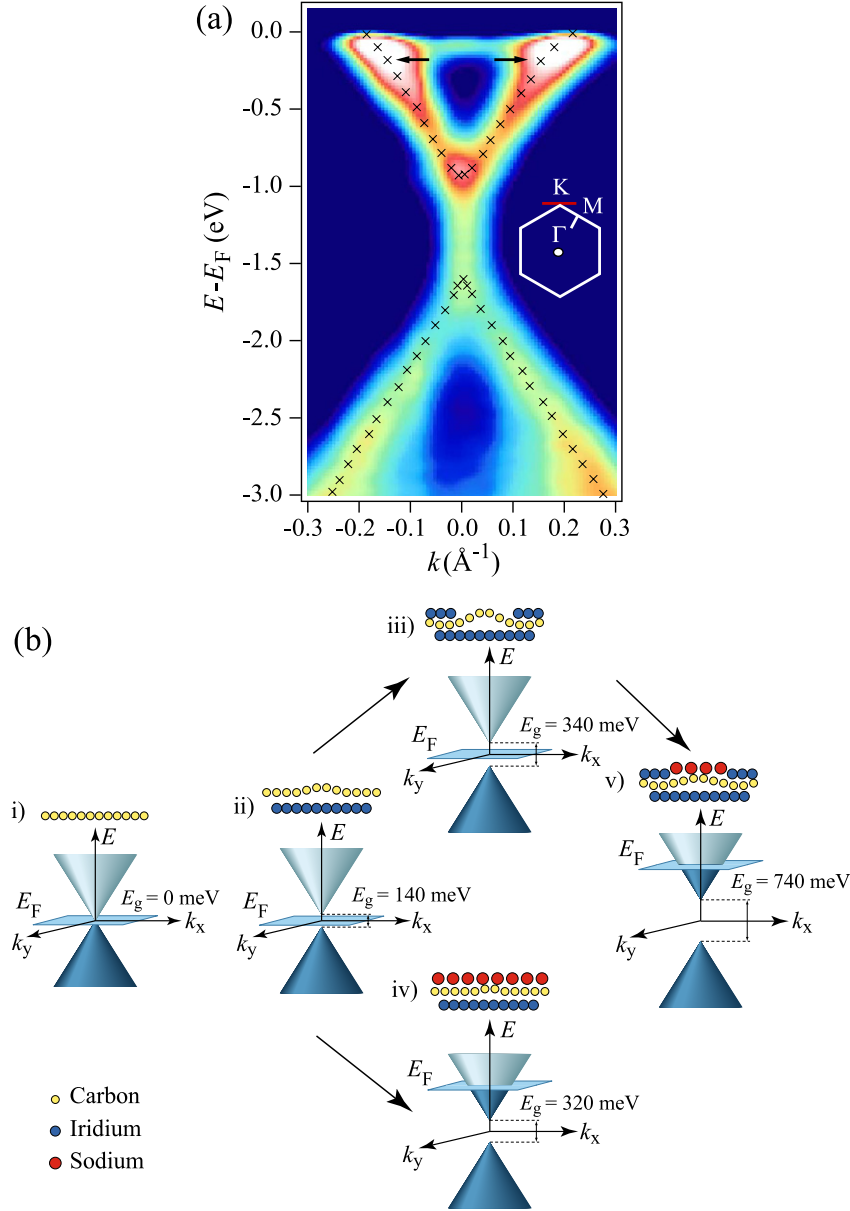


Figure 6. (a) ARPES map along the $p\Gamma K$ direction for Na/Ir/g/Ir(111). The inset shows the 2D Brillouin zone of graphene. The red line indicates the $p\Gamma K$ direction. The black crosses overlaid on the ARPES maps mark the maximum of the photoemission spectral-weight intensity whereas the arrows highlight kinks in the electronic band dispersion generated by the electron–phonon interaction. (b) Side view sketch of the atomic structure and of the π and π^* bands close to the K-point of the graphene Brillouin zone and at E_F for (i) free-standing graphene, (ii) g/Ir, (iii) Ir/g/Ir, (iv) Na/g/Ir and (v) Na/Ir/g/Ir.

perturbation. In order to give a possible explanation for the Na induced band gap we note that the STM data show the adsorption of Na on top of graphene, most likely in a (2×2) phase, and rule out intercalation at room temperature [42]. Although a (2×2) reconstruction is not expected to remove the degeneracy between graphene states at the K-point, a band gap may be induced by hybridization between the electron wavefunctions with wavevectors K and K' promoted by the translation symmetry breaking of the combined Na–graphene–Ir(111) lattice. We attribute the wide gap to Na and Ir jointly breaking the degeneracy of the two graphene sublattices.

5. Conclusions

We have reviewed and presented growth techniques for graphene on Ru(0001) leading to large autocorrelation lengths of up to 240 Å. The electronic properties of graphene on Ir(111) could be tailored while preserving high charge carrier group velocities, a necessary condition for high mobilities.

Acknowledgments

We gratefully acknowledge the contributions of P. Moras, S. Vlačić, M. Etzkorn, P. M. Sheverdyaeva, and D. Pacilé to

this work. We acknowledge support from the Swiss National Science Foundation, from the European Science Foundation under the EUROCORES Program EuroGRAPHENE, and from the Italian Ministry of Education, University and Research (FIRB Futuro in Ricerca, PLASMOGRAPH Project).

References

- [1] Lin Y M, Dimitrakopoulos C, Jenkins K A, Farmer D B, Chiu H Y, Grill A and Avouris P 2010 *Science* **327** 662
- [2] Chen J-H, Cullen W G, Jang C, Fuhrer M S and Williams E D 2009 *Phys. Rev. Lett.* **102** 236805
- [3] Li X *et al* 2009 *Science* **324** 1312
- [4] Bae S *et al* 2010 *Nature Nanotechnol.* **5** 574
- [5] Iwasaki T, Park H J, Konuma M, Lee D S, Smet J H and Starke U 2011 *Nano Lett.* **11** 79
- [6] Novoselov K S, Geim A K, Morozov S V, Jiang D, Zhang Y, Dubonos S V, Grigorieva I V and Firsov A A 2004 *Science* **306** 666
- [7] Baron K, Blakely D and Somorjai G 1974 *Surf. Sci.* **41** 45
- [8] Nieuwenhuys B, Hagen D, Rovida G and Somorjai G 1976 *Surf. Sci.* **59** 155
- [9] Hrbek J 1986 *J. Vac. Sci. Technol. A* **4** 86
- [10] Land T A, Michely T, Behm R J, Hemminger J C and Comsa G 1991 *Appl. Phys. A* **53** 414
- [11] Livneh T and Asscher M 2000 *J. Phys. Chem. B* **104** 3355
- [12] N'Diaye A T, Bleikamp S, Feibelman P J and Michely T 2006 *Phys. Rev. Lett.* **97** 215501
- [13] Vazquez de Parga A L, Calleja F, Borca B, Passeggi M C G, Hinarejos J J, Guinea F and Miranda R 2008 *Phys. Rev. Lett.* **100** 056807
- [14] Wang B, Ma X, Caffio M, Schaub R and Li W-X 2011 *Nano Lett.* **11** 424
- [15] Coraux J, N'Diaye A T, Busse C and Michely T 2008 *Nano Lett.* **8** 565
- [16] N'Diaye A T, Coraux J, Plasa T N, Busse C and Michely T 2008 *New J. Phys.* **10** 043033
- [17] Loginova E, Bartelt N C, Feibelman P J and McCarty K F 2009 *New J. Phys.* **11** 063046
- [18] Yoshii S, Nozawa K, Toyoda K, Matsukawa N, Odagawa A and Tsujimura A 2011 *Nano Lett.* **11** 2628
- [19] Arnoult W J and McLellan R B 1972 *Scr. Metall.* **6** 1013
- [20] Weiss N 2004 *PhD Thesis* EPFL
- [21] Marchini S, Günther S and Wintterlin J 2007 *Phys. Rev. B* **76** 075429
- [22] Sutter P W, Flege J-I and Sutter E A 2008 *Nature Mater.* **7** 406
- [23] McCarty K F, Feibelman P J, Loginova E and Bartelt N C 2009 *Carbon* **47** 1806
- [24] Loginova E, Bartelt N C, Feibelman P J and McCarty K F 2008 *New J. Phys.* **10** 093026
- [25] Natterer F D, Rusponi S and Brune H 2011 *SPG Mitt.* **34** 31
- [26] Park C H, Son Y W, Yang L, Cohen M L and Louie S G 2009 *Phys. Rev. Lett.* **103** 046808
- [27] Brey L and Fertig H A 2009 *Phys. Rev. Lett.* **103** 046809
- [28] Feibelman P J 2008 *Phys. Rev. B* **77** 165419
- [29] Rusponi S, Papagno M, Moras P, Vlaic S, Etzkorn M, Sheverdyaeva P M, Pacile D, Brune H and Carbone C 2010 *Phys. Rev. Lett.* **105** 246803
- [30] Yang L, Park C H, Son Y W, Cohen M L and Louie S G 2007 *Phys. Rev. Lett.* **99** 186801
- [31] Cai J *et al* 2010 *Nature* **466** 470
- [32] Bai J, Zhong X, Jiang S, Huang Y and Duan X 2010 *Nature Nanotechnol.* **5** 190
- [33] Liang X, Jung Y-S, Wu S, Ismach A, Olynick D L, Cabrini S and Borok J 2010 *Nano Lett.* **10** 2454
- [34] Yavari F, Kritzing C, Gaire C, Song L, Gulapalli H, Borca-Tasciuc T, Ajayan P M and Koratkar N 2010 *Small* **6** 2535
- [35] Balog R *et al* 2010 *Nature Mater.* **9** 315
- [36] Starodub E, Bostwick A, Moreschini L, Nie S, Gabaly F E, McCarty K F and Rotenberg E 2011 *Phys. Rev. B* **83** 125428
- [37] Varykhalov A, Scholz M R, Kim T K and Rader O 2010 *Phys. Rev. B* **82** 121101(R)
- [38] Haberer D *et al* 2010 *Nano Lett.* **10** 3360
- [39] Guinea F, Katsnelson M I and Geim A K 2010 *Nature Phys.* **6** 30
- [40] Ohta T, Bostwick A, Seyller T, Horn K and Rotenberg E 2006 *Science* **313** 951
- [41] Zhou S Y, Gweon G H, Fedorov A V, First P N, Heer W A D, Lee D H, Guinea F, Neto A H C and Lanzara A 2007 *Nature Mater.* **6** 770
- [42] Papagno M, Rusponi S, Sheverdyaeva P M, Vlaic S, Etzkorn M, Pacilé D, Moras P, Carbone C and Brune H 2012 *ACS Nano* **6** 199
- [43] Lehnert A, Bulushek P, Weiss N, Giesecke J, Treier M, Rusponi S and Brune H 2009 *Rev. Sci. Instrum.* **80** 023902
- [44] Martoccia D *et al* 2008 *Phys. Rev. Lett.* **101** 126102
- [45] Martoccia D, Björck M, Schlepütz C M, Brugger T, Pauli S A, Patterson B D, Greber T and Willmott P R 2010 *New J. Phys.* **12** 043028
- [46] Moritz W, Wang B, Bocquet M L, Brugger T, Greber T, Wintterlin J and Günther S 2010 *Phys. Rev. Lett.* **104** 136102
- [47] Land T A, Michely T, Behm R J, Hemminger J C and Comsa G 1992 *Surf. Sci.* **264** 261
- [48] Griffiths K, Lennard W, Mitchell I, Norton P, Pirug G and Bonzel H 1993 *Surf. Sci. Lett.* **284** L389
- [49] Wang B, Bocquet M-L, Marchini S, Gunther S and Wintterlin J 2008 *Phys. Chem. Chem. Phys.* **10** 3530
- [50] Iannuzzi M and Hutter J 2011 *Surf. Sci.* **605** 1360
- [51] Pletikosic I, Kralj M, Pervan P, Brako R, Coraux J, N'Diaye A T, Busse C and Michely T 2009 *Phys. Rev. Lett.* **102** 056808
- [52] Sutter E, Acharya D P, Sadowski J T and Sutter P 2009 *Appl. Phys. Lett.* **94** 133101
- [53] Banhart F, Kotakoski J and Krasheninnikov A V 2011 *ACS Nano* **5** 26
- [54] Chen H, Zhu W and Zhang Z 2010 *Phys. Rev. Lett.* **104** 186101
- [55] Gao J, Yuan Q, Hu H, Zhao J and Ding F 2011 *J. Phys. Chem. C* **115** 17695
- [56] Zangwill A and Vvedensky D D 2011 *Nano Lett.* **11** 2092
- [57] Yuan Q, Gao J, Shu H, Zhao J, Chen X and Ding F 2012 *J. Am. Chem. Soc.* **134** 2970
- [58] Phark S H, Borne J, Vanegas A L, Corbetta M, Sander D and Kirschner J 2011 *ACS Nano* **5** 8162
- [59] Starodub E, Maier S, Stass I, Bartelt N C, Feibelman P J, Salmeron M and McCarty K F 2009 *Phys. Rev. B* **80** 235422
- [60] Günther S, Dünhardt S, Wang B, Bocquet M-L, Schmitt S and Wintterlin J 2011 *Nano Lett.* **11** 1895
- [61] Reich S, Maultzsch J, Thomsen C and Ordejón P 2002 *Phys. Rev. B* **66** 035412

5 Outlook and perspective

In our experiments we touched a series of subjects that could be further developed. For instance, the intercalation of Au underneath the *h*-BN layer, the generalization of the observed ring structures to other substrates, as well as a curious interplay with molecular hydrogen. Some of these preliminary results are presented in the following and may apply in a more general context. We therefore intend to give a brief outlook on possible future experiments that are based on, and extend the already established results.

5.1 Au intercalation

The detachment of the boron nitride layer from the metal substrate in the course of transition metal doping has been found to extend to other BN-substrate combinations, notably to *h*-BN/Ni(111), as we will expose subsequently to a presentation of our initial intention to explore this system. As we have seen in chapter 3, the *h*-BN/Ni(111) sample is characterized by a commensurate (1×1) structure and no moiré pattern is formed. The BN layer is almost completely flat and strongly hybridized with the underlying substrate. In order to electronically decouple the layer from the substrate, we have intercalated Au underneath the *h*-BN in a similar fashion as was carried out for graphene/Ni(111) [119, 134]. For the example of a graphene/metal interface the strong hybridization could be successfully lifted by one layer of Au intercalated in between the graphene sheet and the Ni substrate, and concomitantly the properties of a free standing graphene layer were restored, which is now referred to as *quasi* freestanding graphene [134]. In our attempts to intercalate gold at elevated temperature, we have discovered three Au related structures, whereof two are intercalated underneath the *h*-BN layer. The first are compact intercalated Au islands with a characteristic (10×10) superstructure of triangular misfit dislocations [66], and the second are intercalated Au wires pointing away from Au islands and from steps into the open terrace. The Au wires are frequently connected and form honeycomb structures of varying pore size. Figure 5.1 shows an example of intercalated Au on *h*-BN/Ni(111). We note that gold was dosed on *h*-BN/Ni(111) in Fig. 5.1(a) at room temperature and a subsequent annealing was carried out for 10 min at 770 K. Lowering the annealing temperature, and reducing the annealing

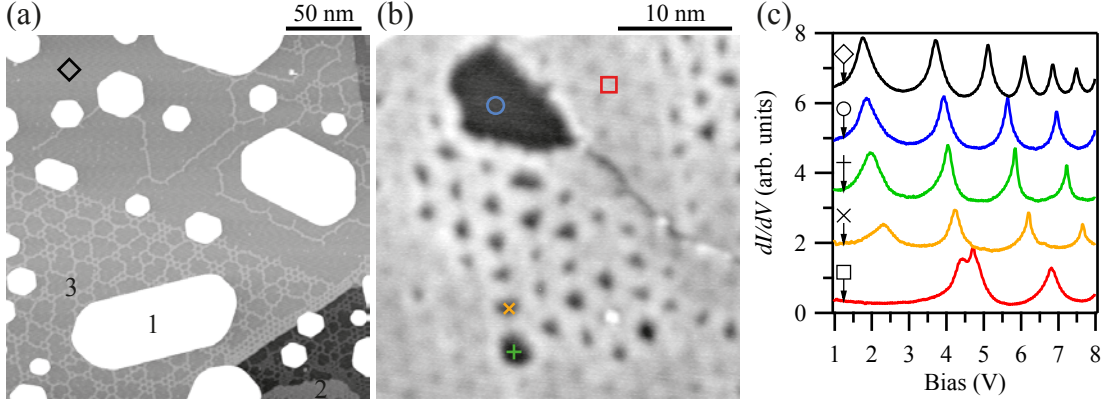


Figure 5.1: Intercalation of Au underneath *h*-BN/Ni(111). (a) Large scale STM image showing coexistence of multilayer Au islands (1), intercalated Au islands (2), intercalated Au wires (3), and empty *h*-BN/Ni(111) (◇). (b) Zoom into coexistence region of intercalated Au (□) and intercalated Au vacancy islands (○, ×, and +). (c) Field emission resonances (FER) can be used to identify the respective phase. [(a) $V_t = -1.0$ V and $I_t = 110$ pA, (b) $V_t = 1.0$ V and $I_t = 20$ pA, (c) FER spectra recorded at constant current with the parameters: $I_t = 100$ pA, $V_{\text{mod}} = 10$ mVpp, and $\nu = 1387$ Hz].

time will augment the ratio of intercalated Au islands and less Au wires will be found, as can be seen in Fig. 5.1(b). Field emission resonances (FER) [16, 19] can be used to identify the respective phases, as was demonstrated in chapter 3, and the corresponding FER spectra are shown in Fig. 5.1(c). The FER traces on empty *h*-BN/Ni(111) (◇) hereby serve as a reference. In particular, one observes a slight shift toward higher energy and a quench of the 1.7 V peak as the lateral dimension of the empty *h*-BN layer is reduced, *i.e.*, by recording FER spectra inside intercalated honeycomb pores of gradually decreasing size. This analysis strongly suggests that the honeycomb pores are actually covered with *h*-BN. The shift of the resonant peaks toward higher energies for the FER in curve □ reflects an increasing work function for intercalated Au as compared to the regions with *h*-BN covering only Ni. As we have shown for the FER on *h*-BN/Rh(111) in chapter 3, the quenching of the first resonant peak is a fingerprint of the decreasing interaction between the *h*-BN layer and the substrate. We recall, that the holes of the (12×12) moiré pattern were characterized by a strong hybridization, and the wires by mere van der Waals interaction between the *h*-BN layer and the substrate, respectively. The *h*-BN sheet is therefore assumed to be only weakly bound to the intercalated Au layer, in accordance with *h*-BN/Cu(111) [108] and *h*-BN/Ag(111) [85].

It is curious to remark that the development of the triangular misfit dislocation seems to be virtually unaffected by the covering *h*-BN layer. The intercalated Au layer appears indistinguishable from the known Au/Ni(111) system [66], and shows the equivalent features of the the (10×10) superstructure [cp. Fig. 5.2(a)]. For the case of intercalated Au wires, we are unaware of a corresponding open (non *h*-BN covered) one-dimensional Au phase on Ni(111), and the latter is highly unlikely to exist. A close inspection of the intercalated honeycomb structure reveals a correlation between the triangular misfit dislocation and the honeycomb

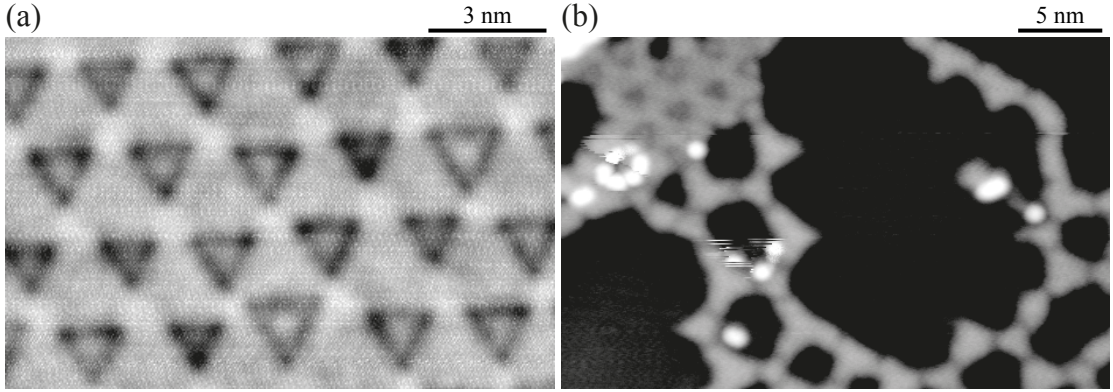


Figure 5.2: Details of intercalated Au structures on h -BN/Au/Ni(111). (a) The STM image of the intercalated (10×10) superstructure features the same characteristics as the open Au/Ni(111) [66]. (b) The transition region between the (10×10) superstructure and the honeycomb structure shows how Au wires originate from the sides of the misfit dislocation triangles. Mn rings centered around the pores of the honeycomb structure are equally present (see text). [(a) $V_t = -50$ mV and $I_t = 200$ pA, (b) $V_t = -100$ mV and $I_t = 10$ pA.]

structure. Encountering wires appear to be joined at the sides of the misfit dislocation triangle. Furthermore, it is seen that the wires are periodically interrupted by segments of a distinct size. Figure 5.2(b) gives an account of the latter two points.

It might be worthwhile to further elaborate on the intercalated wire and honeycomb structures. In particular, the varying pore size could open an interesting route towards the creation of a highly versatile template surface. Metal-organic honeycomb structures have also been investigated in this regard [116], as they allow to prepare a pore size depending on the length of the constructing molecule. The drawbacks of the latter approach, however, are the small accessible temperature range and the exposed substrate surface in the pore center that is prone to contamination. These two limitations might be lifted by using the h -BN/Au/Ni(111) system. The preparation temperature of more than 700 K accounts for the first, and the protective h -BN cover on top of the intercalated Au honeycomb structure for the latter drawback.

Although the present pores share resemblance with the moiré pattern of the h -BN/Rh(111) system, they are of a different origin. We recall that the moiré pattern reflects an 1 \AA vertical geometric corrugation with respect to the flat Rh(111) substrate, *i.e.*, the wires around the moiré holes are not filled with substrate atoms. In the case of the intercalated Au, on the other hand, the wires are composed of Au and covered by a monolayer h -BN. Nonetheless, an interesting parallel is established between the two systems upon dosing small amounts of manganese on the intercalated Au honeycomb structure at 10 K. Figure 5.3 shows one complete and one partial Mn ring centered around the pores of the honeycomb structure [cp. also Fig. 5.2(b)]. The similarity between the present Mn rings and the ones found on h -BN/Rh(111) is striking. In this spirit, we have recorded current-distance traces and $d \ln I / dz$ spectra at the indicated positions [cp. Fig. 5.3(b)], and found the same non-exponential distance-current behavior in the first, and a pronounced peak in the latter case. The peak

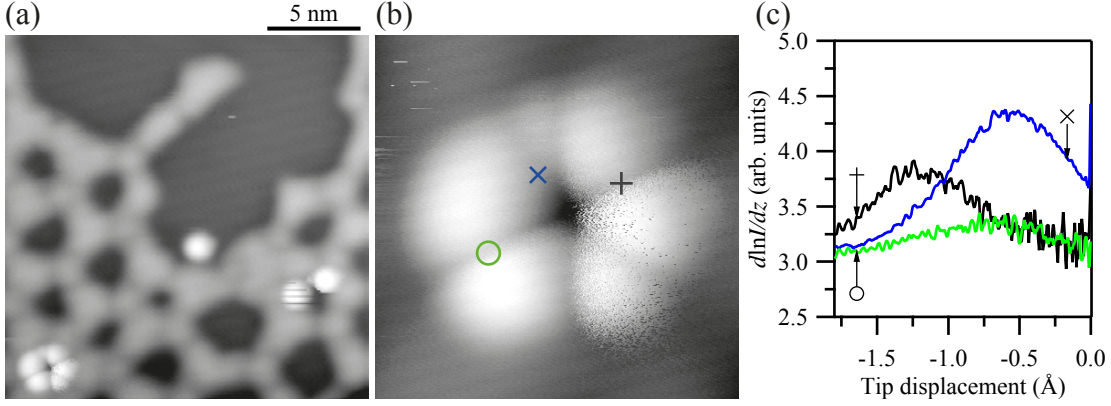


Figure 5.3: Mn rings on intercalated Au on *h*-BN/Ni(111). (a) STM overview image exhibiting two Mn rings centered around the pores of the intercalated Au honeycomb structure. (b) Mn ring and markers indicating the positions where $d \ln I / dz$ spectra were recorded. (c) The spectra reveal the deformation of the *h*-BN layer due to an increasing tip-sample interaction when reducing the gap width of the tunneling junction. [(a) $V_t = -100$ mV and $I_t = 10$ pA, (b) $V_t = -100$ mV and $I_t = 10$ pA, (c) STM parameters prior to opening the feedback-loop: $V_t = -100$ mV, $I_t = 20$ pA, $z_{\text{mod}} = 16$ pm peak-to-peak, and $\nu = 777$ Hz].

in $d \ln I / dz$ spectra is a characteristic of a deformable tunnel junction [34]. As we have established for *h*-BN/Rh(111) [89], the deformation of the tunnel junction is due to a detached *h*-BN layer that is lifted off the substrate and deflecting toward the STM tip upon approaching the latter to the sample surface. The peak in the $d \ln I / dz$ spectra separates the distance where the regimes of attraction and repulsion are interchanged. In conclusion, the Mn adatom is able to weaken the interaction of the *h*-BN layer inside the pore of the honeycomb in the same way as it was demonstrated to weaken the interaction in the holes of the moiré pattern of *h*-BN/Rh(111)-(12 × 12). More details about the latter system can be examined in chapter 3 and in Ref. [89].

This short analogy demonstrates that the doping of strained hexagonal sp^2 hybridized monolayers of boron nitride, and presumably also graphene, with transition metal atoms might allow to locally detach the layer from the supporting substrate in a more general fashion. It would be worthwhile to apply complimentary experimental techniques to measure the properties of these systems. In this spirit, near edge X-ray adsorption spectroscopy (NEX-AFS) [126] is a surface sensitive tool that probes the local bonding environment of a distinct atomic species and has thus revealed a characteristic signature for the degree of hybridization between the *h*-BN layer and the metal substrate [110]. Implementing NEXAFS studies could therefore help to understand how the bonding between the layer and substrate is modified by the addition of a transition metal adatom. This would represent an alternative method to test our hypothesis of a weakened layer-substrate interaction. If our assumption applied, one could imagine that the detached parts of the monolayers behave as oscillating membranes and act as high frequency mechanical nano-scale oscillators. In fact, many transition metal rings were observed to be constantly switching between the ring and the dot state while scanning

with STM. Given the physical dimensions of these hypothetical oscillators, the resonance frequencies ought to be in the THz range and beyond [83]. The phonon dispersion relation and the vibration modes of a *h*-BN layer on Ni(111) have been studied with high resolution electron energy loss spectroscopy (HREELS) [114]. The HREELS technique is clearly a powerful tool and sufficiently sensitive to measure the vibrational properties of metal supported *h*-BN. It would be an interesting experiment to probe the vibrational energies of the detached membranes with HREELS. Furthermore, the use of an atomic force microscope (AFM) could offer a direct insight into the forces acting between the detached membrane and the substrate. In particular, the recent advances in the technique of combined STM and tuning fork AFM (qPlus) [49, 50] would present an interesting method for the investigation of these detached monolayers of *h*-BN and graphene. Moving the focus from close-packed surface to more open substrates would finally allow to extend the study to membranes of different dimensionality. For instance, it would be interesting to investigate whether and how transition metal adatoms modify the interaction with the substrate for the 1D structures of Fe(110) supported graphene [138] and *h*-BN [139].

5.2 Hydrogen superstructure - molecular rotations

The interaction of hydrogen with the sample has been described in section 3.2.1 and 3.3 in terms of a disturbance and has therein been regarded as a nuisance/contamination. Here we want judge hydrogen by alternative criteria and wish to explore a different path in order to highlight some of the exciting aspects of hydrogen adsorbed at low temperature.

Hydrogen has been found to be responsible for the strong apparent height reduction of Ti adatoms on metal supported *h*-BN. We have scrutinized the latter by exposing our Ti adatoms to a partial pressure of hydrogen and by recording the concomitant changes in topography. The scenario is well described in section 3.2.1 and we will not further dwell on the properties of Ti adatoms. In the course of these experiments, however, we have also observed interesting features that are independent of the transition metal adsorbate. One example is found in the circular patches of a hydrogen superstructure, stabilized around Ti adatoms and point defects, that are visible after deliberately exposing the sample to a partial pressure of molecular hydrogen at 10 K. Figure 5.4 gives an account of this hydrogen related superstructure. The hydrogen patches have a peak-to-peak corrugation of (14.3 ± 0.5) pm, while the *h*-BN layer is corrugated by (12.3 ± 0.2) pm. We note that the enhanced resolution in the STM images of *h*-BN, despite the moderate tunneling conditions, may be attributed to a trapped hydrogen molecule in the gap of the tunneling junction [131]. The periodicity ratios of superstructure and *h*-BN are with $q_{\text{STM}} = (1.74 \pm 0.02)$, and $q_{\text{FFT}} = (1.72 \pm 0.01)$ very close to $\sqrt{3}$, and the relative orientation is $(30 \pm 1)^\circ$, *i.e.*, the superstructure is described by $(\sqrt{3} \times \sqrt{3})R30^\circ$. If the maxima of the superstructure coincided with the hydrogen adsorption site, the molecule would be resting in the *h*-BN hollow site, which can either be fcc or hcp relatively to the Ni(111) surface, depending on the respective *h*-BN phase [52, 9]. We note that such a superstructure has been reported for physisorbed hydrogen on graphite [118] which is but one element of an

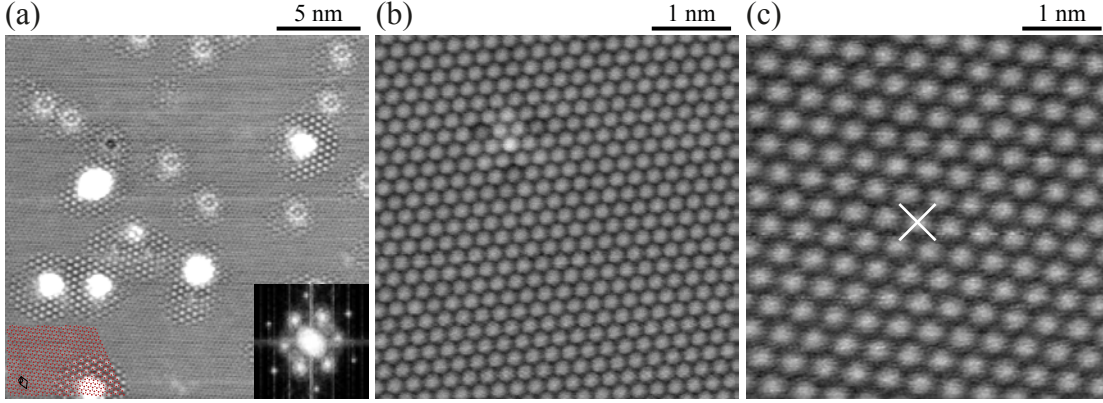


Figure 5.4: Hydrogen superstructure on *h*-BN/Ni(111). (a) Overview image showing hydrogenated Ti adatoms and point defects surrounded by circular patches of a $(\sqrt{3} \times \sqrt{3})R30^\circ$ hydrogen superstructure. The inset shows the corresponding FFT image. (b) Atomic resolution of *h*-BN layer and (c) hydrogen superstructure. The (×) indicates where dI/dV spectra of Fig. 5.5 were recorded. [(a) $V_t = -10$ mV and $I_t = 20$ pA, (b) $V_t = -50$ mV and $I_t = 20$ pA, (c) $V_t = -20$ mV and $I_t = 20$ pA.]

intriguingly rich phase diagram of 2D hydrogen at low temperature [44, 45].

Tuning the controllable parameters, *i.e.*, by changing the density of adsorbed hydrogen or varying the sample temperature, would allow to explore the phase space of this two dimensional quantum material. The phase diagram of adsorbed hydrogen on graphite has been sketched with data from neutron and electron diffraction studies [118, 44, 45], and numerous phases and their connecting transitions were discovered. For instance, a commensurate-incommensurate and a solid-2D gas/liquid phase transition were identified. A related study showed that the pronounced isotope effect of the hydrogen molecule results in a distinct phase diagram for adsorbed deuterium [46]. We note that a neutron diffraction study has been carried out for adsorbed hydrogen on a *h*-BN powder sample [42]. It was furthermore established that hydrogen behaves in a similar fashion on BN as it does on graphite substrates [42, 144]. The employed techniques probe a macroscopic sample area/volume and interesting details, for instance the evolution of the phase boundaries, might be missed. This drawback could be overcome with an STM as it offers the possibility to locally inspect the sample. Given that we are able to detect the commensurate $(\sqrt{3} \times \sqrt{3})R30^\circ$ superstructure with STM, we might also be capable of measuring the complimentary 2D phases and the connecting transitions for adsorbed hydrogen and its isotopes.

The remaining part of this outlook is an early view on the first STM observation of nuclear disparate configurations of hydrogen and deuterium. These are preliminary conclusions and sketch the current state of our work.

Symmetry requirements for the exchange of protons within the molecule entail two nuclear distinct forms of hydrogen [122]. In the so called para configuration (*p*-H₂), the nuclear spins of both protons are aligned antiparallel, and the total molecular nuclear spin is zero.

Contrariwise, ortho hydrogen ($o\text{-H}_2$) is characterized by two parallel proton spins and a total molecular nuclear spin of 1. Although $p\text{-H}_2$ is the ground state configuration, the ratio between the ortho and para population is 3:1 in thermodynamic equilibrium at room temperature. Since the transition from $o\text{-H}_2$ to $p\text{-H}_2$ is forbidden for the free molecule, an out of equilibrium population can be created when cooling the hydrogen gas to low temperatures. The conversion from $o\text{-H}_2$ to $p\text{-H}_2$ is very slow but significantly accelerated, for instance, in the presence of paramagnetic impurities [65, 122]. Efficient $o \rightarrow p$ conversion catalysts have technical relevance in hydrogen liquefaction. The rotational quanta of the two hydrogen states and the corresponding states for deuterium are tabulated in table 5.1. The first rotational quantum for $p\text{-H}_2$ ($J = 0 \rightarrow J = 2$) is 43.9 meV and 72.8 meV for $o\text{-H}_2$ ($J = 1 \rightarrow J = 3$) [122]. These excitations are referred to as 3D rigid rotors and have been measured with HREELS for adsorbed hydrogen on Ag(111) [10] and Cu(100) [4] surfaces. The measurements of these studies were carried out at cryogenic temperatures where all hydrogen molecules are in their vibrational ground state ($\nu = 0$). These HREELS studies [4, 10] could therefore also capture combinations of vibrational and rotational excitations, for instance around the loss peak of 516 meV ($\nu = 0 \rightarrow \nu = 1$) [122]. A related HREELS study on a Cu(510) surface showed excitations corresponding to ortho and para hydrogen constraint at steps edges in a 2D rotational excitation [129]. In this case the rotational quanta are 29.4 meV ($J = 0 \rightarrow J = 2$) and 58.8 meV ($J = 1 \rightarrow J = 3$) for $p\text{-H}_2$ and $o\text{-H}_2$, respectively [129, 130]. It is interesting to note that all the mentioned energy levels are well within the energy range conveniently accessible with STM [cp. table 5.1].

Table 5.1: Summary of 2D and 3D rotational, and vibrational energy quanta for nuclear disparate spin configurations of hydrogen and deuterium. Energies are given in meV and taken from Silvera [122], and Bengtsson [17].

	state	$E_{J+2}^{2D} - E_J^{2D}$	$E_{J+2}^{3D} - E_J^{3D}$	vibration ($\nu = 0 \rightarrow \nu = 1$)
Hydrogen	$p\text{-H}_2$ ($J = 0$)	29.4	43.9	516
	$o\text{-H}_2$ ($J = 1$)	58.8	72.8	+ rot. satellites
Deuterium	$o\text{-D}_2$ ($J = 0, 2$)	14.8	22.2	371
	$p\text{-D}_2$ ($J = 1$)	29.6	36.9	+ rot. satellites

We measured the differential conductance at the equivalent positions indicated by (\times) in Fig. 5.4(c) of the superstructure for hydrogen and deuterium. The dI/dV spectra in Fig. 5.5 reveal sudden conductance changes at the energies of ± 44 meV and ± 21 meV, for hydrogen and deuterium, respectively. Abrupt conductance jumps are characteristic for the activation of a new inelastic conductance channel [125]. We attribute these energies to an excitation of a 3D rotation of para-hydrogen and ortho-deuterium (from $J = 0 \rightarrow J = 2$), respectively. The energy ratio between the hydrogen and the deuterium features is clearly incompatible with a vibrational excitation, since the latter ought to scale with $\sqrt{2}$. Rotational quanta, on the other hand, scale with the moment of inertia and thus perfectly match the factor 2 of the above energy ratio. Note that we observed slight variations of the energy position of order 1 meV. These can be ascribed to subtle dilations of the molecular axis [10]. The dip at the

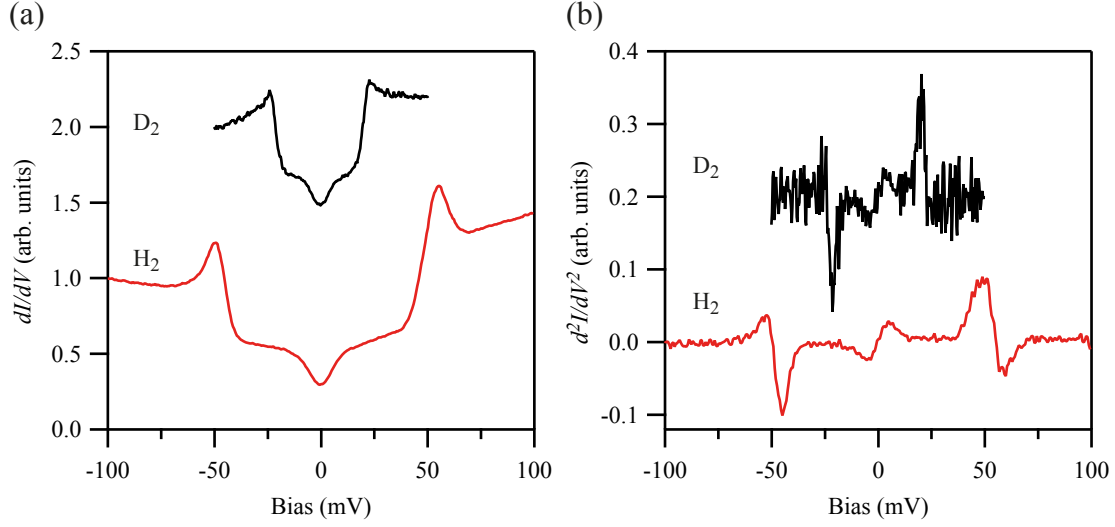


Figure 5.5: Differential conductance of hydrogen and deuterium molecules in the respective $(\sqrt{3} \times \sqrt{3})R30^\circ$ superstructure. The tip was positioned at the indicated locations equivalent to (x) in Fig. 5.4(c). (Setpoint before opening the feedback-loop: For hydrogen, $V_t = -100$ mV, $I_t = 50$ pA, $V_{\text{mod}} = 5$ mVpp, mean of 21 spectra. For deuterium, $V_t = -50$ mV, $I_t = 50$ pA, $V_{\text{mod}} = 2$ mVpp, mean of 8 spectra. The dI/dV traces were normalized to the starting conductance and vertically offset by one unit. The d^2I/dV^2 was numerically differentiated from dI/dV spectra and vertically offset.)

Fermi energy is not yet fully grasped but tentatively explained in terms of a vertical molecular vibration with respect to the h -BN layer [94]. For an harmonic oscillator, the width of the feature should scale with $\sqrt{2}$ as mentioned before, however, since hydrogen and deuterium are seriously modified by inharmonic effects, deviations from this scaling are expected. Although the width appears slightly more narrow for deuterium, we need to be extra careful in the analysis because the influence of modulation and thermal broadening should adequately be accounted for. From the deconvolution of the latter effects, the inspection of the intrinsic excitation energies and widths will require the correct consideration of the hydrogen and deuterium zero-point motion (ZPM). The ZPM can entail a slight modification of the expected $\sqrt{2}$ ratio between the respective vibrational features of H₂ and D₂.

Inspection of energies beyond 100 meV yielded no satisfying response as to whether higher order rotations could be activated. Neither were we able to observe inelastic features at energies in the expected energy window for vibration ($\nu = 0 \rightarrow \nu = 1$). This could be due to the electrical field that forces the molecule out of the junction, what might explain the instabilities in the tunneling junction at certain threshold bias values. Another possibility could be the reduced excitation cross section for these processes. Note the strong magnification in HREELS measurements of H₂ and D₂ that had to be applied in order to visualize the respective excitations [10, 4, 129].

We finish by remarking that a study with adsorbed acetylene molecules demonstrated that

an STM offers in principle the possibility to excite and detect molecular rotations [124]. The present case would represent the ultimate limit of a rigid rotor and would constitute the smallest diatomic rotor observable with STM. For Ni(111) supported *h*-BN the conversion from *o*-H₂ to *p*-H₂ appears to be too fast to also capture the ortho hydrogen $J = 1 \rightarrow J = 3$ transition with inelastic tunneling spectroscopy (IETS). In sporadic cases, spectra showed inelastic features at energies close to 70–80 meV. The statistics, however, is not reliable and no conclusions about the abundance of ortho hydrogen can be made. The choice of an adequate substrate seems to be the delicate issue. It appears as if many unsuccessful attempts have been made to measure such excitations with STM on Cu [56, 120, 121], Ag(111) [131], Ag(110) [131], and on Au(111) [131, 141]. Although IETS features were observed in the latter list of contributions, these IETS characteristics exhibited varying energies that were believed to be incompatible with the rotational quanta mentioned in table 5.1. Given that *h*-BN can be prepared on numerous substrates [cp. chapter 3], and that we are able to observe the ground state of hydrogen and deuterium on *h*-BN/Ni(111), metal supported *h*-BN might be the better choice than the mere metal surface. We stress that it would be an exciting task to scrutinize whether also the ortho hydrogen $J = 1 \rightarrow J = 3$ transition could be excited with STM. If this was the case, we would have a formidable tool on hand that would allow to distinguish between nuclear disparate hydrogen molecules using an STM. From this perspective a whole range of opportunities arise. The unmatched spatial resolution of an STM could allow the direct mapping of nuclear spins with sub nanometer precision. One could think about locally inspecting the *o*-H₂ to *p*-H₂ conversion, and extract the magnetic moment of a nearby structure from the conversion rates [65]. Another aspect could be the study of the rich ordering phenomena for ortho hydrogen on boron nitride at low temperatures [68, 42]. In particular, it would be interesting to examine the intriguing pinwheel *o*-H₂ and related phases. However, for the latter study an STM with an effective temperature range below the boiling point of helium would be required.

A Appendix

In this appendix we will briefly outline our contribution to the assembly of a dedicated UHV system, initially designed by U. Schlickum and M. Kobas. The author set-up the lab, assembled the vacuum chambers, mounted the Auger electron spectroscopy, and performed initial cooling tests for the sample holder system. At a later stage, the project was handed to S. Fedrigo, who first improved the heating system and now signs responsible for the latest development, which includes the drawing and assembly of the scanning tunneling microscope.

Since an STM heavily suffers from vibrational noise that limits the mechanical stability of the tip-sample tunnel junction, special care has to be taken to prevent the coupling of vibrations into the system. While building vibrations above 30 Hz can readily be damped by pneumatic isolator legs (Newport I-2000), the low frequency underground cannot be effectively suppressed by such a system, in particular, the part close to the eigenfrequency of the leg-UHV chamber are not damped at all or are even amplified. The STM performance is thus strongly determined by the low frequency underground of its sheltering lab. We have therefore chosen lab H0482 according to its promising low vibrational underground (cf. Figure A.1) which is achieved by a concrete baseplate that is decoupled from the building and that rests on a sand bed. When the building was constructed, this room had been foreseen for the sheltering of an electron microscope. We have assembled the framework that supports the UHV chamber. It has been forged out of nonmagnetic stainless steel and its head space has furthermore been filled with sand [cf. Figure A.2(a)] to increase weight and to improve damping. Prior to filling, the sand was dried in a low pressure furnace for several hours.

Figure A.2 illustrates the temporal evolution of the assembly process of the UHV system in lab H0482. The individual components, namely, preparation chamber [cp. Fig. A.2(b)], measurement chamber [cp. Fig. A.2(c)], load lock, sample manipulator, and the cryostat [cp. Fig. A.2(d)] have been mounted and connected. Later, we have added the pneumatic legs and the sample manipulator [cp. Fig. A.2(e)]. Figure A.2(f) shows the *status quo* of lab H0482. The individual chambers are separated by gate valves and can maintain their vacuum independently through their dedicated pumping system. The vacuum is generated and preserved by three turbo-molecular pumps that are backed by primary rotary pumps. The

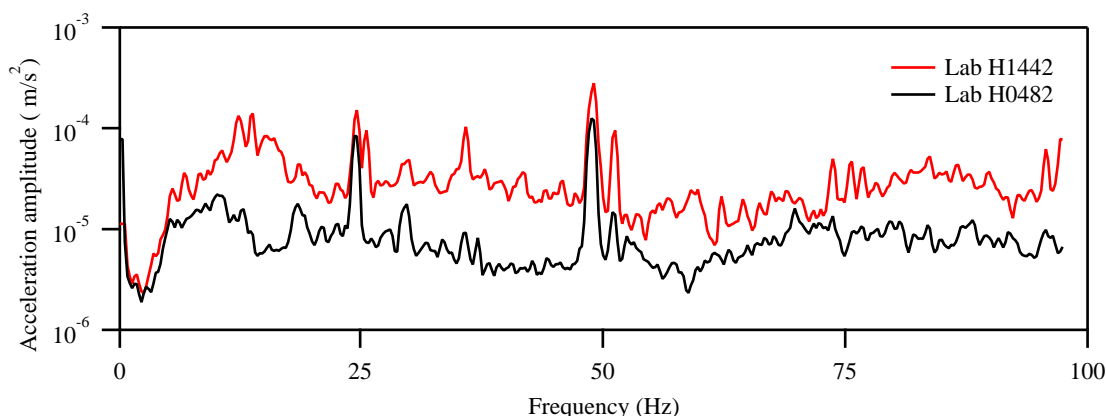


Figure A.1: Comparison of vibrational underground (acceleration amplitudes) of two different labs. Laboratory H0482 shows a way better low frequency underground than lab H1442.

preparation chamber and the STM chamber are both equipped with ion pumps. In the former, a gate valve is introduced between the ion pump and the preparation chamber, to reduce the effective volume and to avoid a filling of the ion pump with argon during sputtering. The sample manipulator is equipped with a flow cryostat that can either be cooled by LN2 or liquid helium. The latter is preferred as it allows to cool the sample to 30 K and below within half an hour. The separation of our device into a dedicated preparation and a measurement chamber has the advantage that sample preparation cycles and the involved high pressures have no detrimental effect on the measurement chamber. The latter is essential as we have seen in chapter 3 for the case of a hydrogen interplay with Ti adatoms. A turbo molecular pump with a particular high compression ratio for hydrogen¹ is installed at the cryostat chamber to levitate the hydrogen issue. We have also added a vacuum reservoir made out of a stainless steel beer barrel that allows to switch off the primary pumps and that offers the turbo-molecular pumps enough backing to maintain the base pressure. By this means, the noise level in the lab can be reduced and preliminary sample characterization can be carried out without turning off the turbo pumps. A greater number of experiments is feasible with this barrel backing. Note that at the beginning of an experimental cycle the sample preparation recipe is not yet fully mastered and many STM inspections are needed to establish the correct preparation. Bakeouts of the vacuum system readily yield a base pressure of 2×10^{-10} mbar in the preparation chamber. The cryogenically cooled STM chamber can naturally provide better vacuum conditions. However, at the current state, a frequent breaking of the vacuum is necessary for installing and testing newly installed parts, and therefore no particular efforts are made in reaching the ultimate low pressure.

¹Pfeiffer Vacuum HiPace 300



Figure A.2: Time evolution of UHV chamber assembly in lab H0482. (a) The author filling the framework with dry sand. (b) Completely assembled framework with preparation chamber. (c) Measurement chamber with cryostat. (d) First bakeout. (e) Installed sample manipulator and pneumatic legs. (f) Fully assembled UHV system with load lock (status quo the 30.10.12).

Bibliography

- [1] M. D. ABRAMOFF, P. J. MAGALHAES, AND S. J. RAM, *Image processing with ImageJ*, Biophotonics International, 11 (2004), p. 36.
- [2] M. ALLAN, S. BERNER, M. CORSO, T. GREBER, AND J. OSTERWALDER, *Tunable self-assembly of one-dimensional nanostructures with orthogonal directions*, Nanoscale Res. Lett., 2 (2007), p. 94.
- [3] D. ALPERT, *New developments in the production and measurement of ultra high vacuum*, J. Appl. Phys., 24 (1953), p. 860.
- [4] S. ANDERSSON AND J. HARRIS, *Observation of rotational transitions for H_2 , D_2 , and HD adsorbed on Cu(100)*, Phys. Rev. Lett., 48 (1982), p. 545.
- [5] W. J. ARNOULT AND R. B. MCLELLAN, *The solubility of carbon in rhodium ruthenium, iridium and rhenium*, Scr. Metall., 6 (1972), p. 1013.
- [6] W. AUWÄRTER, *One Monolayer of Hexagonal Boron Nitride on Ni(111): an Atomically Sharp Interface*, PhD thesis, University of Zurich, 2003.
- [7] W. AUWÄRTER, T. J. KREUTZ, T. GREBER, AND J. OSTERWALDER, *XPD and STM investigation of hexagonal boron nitride on Ni(111)*, Surf. Sci., 429 (1999), p. 229.
- [8] W. AUWÄRTER, M. MUNTWILER, T. GREBER, AND J. OSTERWALDER, *Co on h-BN/Ni(111): from island to island-chain formation and Co intercalation*, Surf. Sci., 511 (2002), p. 379.
- [9] W. AUWÄRTER, M. MUNTWILER, J. OSTERWALDER, AND T. GREBER, *Defect lines and two-domain structure of hexagonal boron nitride films on Ni(111)*, Surf. Sci., 545 (2003), p. L735.
- [10] P. AVOURIS, D. SCHMEISSER, AND J. E. DEMUTH, *Observation of rotational excitations of H_2 adsorbed on Ag surfaces*, Phys. Rev. Lett., 48 (1982), p. 199.
- [11] F. BANHART, J. KOTAKOSKI, AND A. V. KRASHENINNIKOV, *Structural defects in graphene*, ACS Nano, 5 (2011), p. 26.
- [12] J. BARDEEN, *Tunnelling from a many-particle point of view*, Phys. Rev. Lett., 6 (1961), p. 57.

Bibliography

- [13] K. BARON, D. BLAKELY, AND G. SOMORJAI, *Low energy electron diffraction studies of the surface structures of adsorbed hydrocarbons (n-heptane, toluene, benzene, ethylene, and cyclohexane) on stepped (high miller index) platinum surfaces*, Surf. Sci., 41 (1974), p. 45.
- [14] V. BARONE, O. HOD, AND G. E. SCUSERIA, *Electronic structure and stability of semiconducting graphene nanoribbons*, Nano Lett., 6 (2006), p. 2748. PMID: 17163699.
- [15] P. J. BARRIE, *Analysis of temperature programmed desorption (TPD) data for the characterisation of catalysts containing a distribution of adsorption sites*, Phys. Chem. Chem. Phys., 10 (2008), p. 1688.
- [16] R. S. BECKER, J. A. GOLOVCHENKO, AND B. S. SWARTZENTRUBER, *Electron interferometry at crystal surfaces*, Phys. Rev. Lett., 55 (1985), p. 987.
- [17] L. BENGTTSSON, K. SVENSSON, M. HASSEL, J. BELLMAN, M. PERSSON, AND S. ANDERSSON, *H₂ adsorbed in a two-dimensional quantum rotor state on a stepped copper surface*, Phys. Rev. B, 61 (2000), p. 16921.
- [18] S. BERNER, M. CORSO, R. WIDMER, O. GRÖNING, R. LASKOWSKI, P. BLAHA, K. SCHWARZ, A. GORIACHKO, H. OVER, S. GSELL, M. SCHRECK, H. SACHDEV, T. GREBER, AND J. OSTERWALDER, *Boron nitride nanomesh: Functionality from a corrugated monolayer*, Angew. Chem. Int. Ed., 46 (2007), p. 5115.
- [19] G. BINNIG, K. H. FRANK, H. FUCHS, N. GARCIA, B. REIHL, H. ROHRER, F. SALVAN, AND A. R. WILLIAMS, *Tunneling spectroscopy and inverse photoemission: Image and field states*, Phys. Rev. Lett., 55 (1985), p. 991.
- [20] G. BINNIG AND H. ROHRER, *Scanning tunneling microscop - from birth to adolescence*, Rev. Mod. Phys., 59 (1987), p. 615.
- [21] G. BINNIG, H. ROHRER, C. GERBER, AND E. WEIBEL, *Tunneling through a controllable vacuum gap*, Appl. Phys. Lett., 40 (1982), p. 178.
- [22] P. BLONSKI, A. LEHNERT, S. DENNLER, S. RUSPONI, M. ETZKORN, G. MOULAS, P. BENCOK, P. GAMBARDILLA, H. BRUNE, AND J. HAFNER, *Magnetocrystalline anisotropy energy of Co and Fe adatoms on the (111) surfaces of Pd and Rh*, Phys. Rev. B, 81 (2010), p. 104426.
- [23] B. BORCA, S. BARJA, M. GARNICA, M. MINNITI, A. POLITANO, J. M. RODRIGUEZ-GARCIA, J. J. HINAREJOS, D. FARIAS, A. L. V. DE PARGA, AND R. MIRANDA, *Electronic and geometric corrugation of periodically rippled, self-nanostructured graphene epitaxially grown on Ru(0001)*, New Journal of Physics, 12 (2010), p. 093018.
- [24] L. BREY AND H. A. FERTIG, *Emerging zero modes for graphene in a periodic potential*, Phys. Rev. Lett., 103 (2009), p. 046809.
- [25] I. BRIHUEGA, C. H. MICHAELIS, J. ZHANG, S. BOSE, V. SESSI, J. HONOLKA, M. A. SCHNEIDER, A. ENDERS, AND K. KERN, *Electronic decoupling and templating of Co nanocluster arrays on the boron nitride nanomesh*, Surf. Sci., 602 (2008), p. L95.

-
- [26] T. BRUGGER, H. MA, M. IANNUZZI, S. BERNER, A. WINKLER, J. HUTTER, J. OSTERWALDER, AND T. GREBER, *Nano-texture switching of single layer hexagonal boron nitride on rhodium by hydrogen intercalation*, Ang. Chemie Int. Ed., 49 (2010), p. 6120.
- [27] H. BRUNE, *Microscopic view of epitaxial metal growth: nucleation and aggregation*, Surf. Sci. Rep., 31 (1998), p. 121.
- [28] H. BRUNE, M. GIOVANNINI, K. BROMANN, AND K. KERN, *Self-organized growth of nanostructure arrays on strain-relief patterns*, Nature, 394 (1998), p. 451.
- [29] P. BULUSCHEK, *Submonolayer growth of cobalt on metallic and insulating surfaces studied by scanning tunneling microscopy and kinetic Monte-Carlo simulations.*, PhD thesis, EPFL, 2007.
- [30] O. BUNK, M. CORSO, D. MARTOCCIA, R. HERGER, P. R. WILLMOTT, B. D. PATTERSON, J. OSTERWALDER, J. F. V. D. VEEN, AND T. GREBER, *Surface X-ray diffraction study of boron-nitride nanomesh in air*, Surf. Sci., 601 (2007), p. L7.
- [31] J. CAI, P. RUFFIEUX, R. JAAFAR, M. BIERI, T. BRAUN, S. BLANKENBURG, M. MUOTH, A. P. SEITSONEN, M. SALEH, X. FENG, K. MÜLLEN, AND R. FASEL, *Atomically precise bottom-up fabrication of graphene nanoribbons*, Nature, 466 (2010), p. 470.
- [32] E. ĆAVAR, R. WESTERSTRÖM, A. MIKKELSEN, E. LUNDGREN, A. VINOGRADOV, M. L. NG, A. PREOBRJENSKI, A. ZAKHAROV, AND N. MÄRTENSSON, *A single h-BN layer on Pt(111)*, Surf. Sci., 602 (2008), p. 1722.
- [33] C. J. CHEN, *Introduction to Scanning Tunneling Microscopy*, Oxford University Press, New York, 1993.
- [34] C. J. CHEN AND R. J. HAMERS, *Role of atomic force in tunneling barrier measurements*, J. Vac. Sci. Technol. B, 9 (1991), p. 503.
- [35] K. CHRISTMANN, *Interaction of hydrogen with solid surfaces*, Surf. Sci. Rep., 9 (1988), p. 1.
- [36] M. CORSO, W. AUWÄRTER, M. MUNTWILER, A. TAMAI, T. GREBER, AND J. OSTERWALDER, *Boron nitride nanomesh*, Science, 303 (2004), p. 217.
- [37] M. CORSO, T. GREBER, AND J. OSTERWALDER, *h-BN on Pd(110): a tunable system for self-assembled nanostructures?*, Surf. Sci., 577 (2005), p. L78.
- [38] R. M. DESROSIERS, D. W. GREVE, AND A. J. GELLMAN, *Nucleation of boron nitride thin films on Ni(100)*, Surf. Sci., 382 (1997), p. 35.
- [39] H. DIL, J. LOBO-CHECA, R. LASKOWSKI, P. BLAHA, S. BERNER, J. OSTERWALDER, AND T. GREBER, *Surface trapping of atoms and molecules with dipole rings*, Science, 319 (2008), p. 1824.

Bibliography

- [40] Y. DING, M. IANNUZZI, AND J. HUTTER, *Investigation of boron nitride nanomesh interacting with water*, J. Phys. Chem. C, 115 (2011), p. 13685.
- [41] S. DUSHMAN AND A. H. YOUNG, *Calibration of ionization gauge for different gases*, Phys. Rev., 68 (1945), p. 278.
- [42] M. D. EVANS AND N. S. SULLIVAN, *Experimental studies of hydrogen on boron nitride: II. NMR studies of orientational ordering of H₂*, J. Low Temp. Phys., 100 (1995), p. 551.
- [43] U. FANO, *Effects of configuration interaction on intensities and phase shifts*, Phys. Rev., 124 (1961), p. 1866.
- [44] H. FREIMUTH AND H. WIECHERT, *Phases and phase transitions of para-hydrogen monolayers adsorbed on graphite*, Surf. Sci., 162 (1985), p. 432.
- [45] H. FREIMUTH, H. WIECHERT, AND H. LAUTER, *The commensurate-incommensurate transition of hydrogen monolayers physisorbed on graphite*, Surf. Sci., 189 (1987), p. 548.
- [46] H. FREIMUTH, H. WIECHERT, H. P. SCHILDBERG, AND H. J. LAUTER, *Neutron-diffraction study of the commensurate-incommensurate phase transition of deuterium monolayers physisorbed on graphite*, Phys. Rev. B, 42 (1990), p. 587.
- [47] R. GAISCH, *Scanning tunneling microscopy in ultra-high vacuum at low temperature*, PhD thesis, Université de Lausanne, 1994.
- [48] R. GAISCH, J. K. GIMZEWSKI, B. REIHL, R. R. SCHLITTLER, M. TSCHUDY, AND W. D. SCHNEIDER, *Low-temperature ultra-high vacuum scanning tunneling microscope*, Ultra-microscopy, 42 (1992), p. 1621.
- [49] F. J. GIESSIBL, *High-speed force sensor for force microscopy and profilometry utilizing a quartz tuning fork*, Appl. Phys. Lett., 73 (1998), p. 3956.
- [50] F. J. GIESSIBL, *Advances in atomic force microscopy*, Rev. Mod. Phys., 75 (2003), p. 949.
- [51] A. GORIACHKO, Y. HE, M. KNAPP, H. OVER, M. CORSO, T. BRUGGER, S. BERNER, J. OSTERWALDER, AND T. GREBER, *Self-assembly of a hexagonal boron nitride nanomesh on Ru(0001)*, Langmuir, 23 (2007), p. 2928.
- [52] G. B. GRAD, P. BLAHA, K. SCHWARZ, W. AUWÄRTER, AND T. GREBER, *Density functional theory investigation of the geometric and spintronic structure of h-BN/Ni(111) in view of photoemission and STM experiments*, Phys. Rev. B, 68 (2003), p. 085404.
- [53] T. GREBER, L. BRANDENBERGER, M. CORSO, A. TAMAI, AND J. OSTERWALDER, *Single layer hexagonal boron nitride films on Ni(110)*, e-J. Surf. Sci. Nanotechnol., 4 (2006), p. 410.
- [54] T. GREBER, M. CORSO, AND J. OSTERWALDER, *Fermi surfaces of single layer dielectrics on transition metals*, Surf. Sci., 603 (2009), p. 1373.

-
- [55] K. GRIFFITHS, W. LENNARD, I. MITCHELL, P. NORTON, G. PIRUG, AND H. BONZEL, *Saturated ethylene coverage on Pt(111): a comparison of nuclear reaction analysis and X-ray photoemission data*, Surf. Sci. Lett., 284 (1993), p. L389.
- [56] J. A. GUPTA, C. P. LUTZ, A. J. HEINRICH, AND D. M. EIGLER, *Strongly coverage-dependent excitations of adsorbed molecular hydrogen*, Phys. Rev. B, 71 (2005), p. 115416.
- [57] D. HABERER, D. V. VYALIKH, S. TAIOLI, B. DORA, M. FARJAM, J. FINK, D. MARCHENKO, T. PICHLER, K. ZIEGLER, S. SIMONUCCI, M. S. DRESSSELHAUS, M. KNUPFER, B. BÜCHNER, AND A. GRÜNEIS, *Tunable band gap in hydrogenated quasi-free-standing graphene*, Nano Lett., 10 (2010), p. 3360.
- [58] R. J. HAMERS, *Methods of tunneling spectroscopy with the STM*, 1993.
- [59] M. Y. HAN, B. ÖZYILMAZ, Y. ZHANG, AND P. KIM, *Energy band-gap engineering of graphene nanoribbons*, Phys. Rev. Lett., 98 (2007), p. 206805.
- [60] J. HARRIS AND S. ANDERSSON, *H₂ dissociation at metal surfaces*, Phys. Rev. Lett., 55 (1985), p. 1583.
- [61] A. C. HEWSON, *The Kondo problem to heavy fermions*, Cambridge University Press, 1993.
- [62] M. M. HILLS, J. E. PARMETER, C. B. MULLINS, AND W. H. WEINBERG, *Interaction of ethylene with the ruthenium(001) surface*, J. Am. Chem. Soc., 108 (1986), p. 3554.
- [63] J. HRBEK, *Carbonaceous overlayers on Ru(001)*, J. Vac Sci. Technol., A, 4 (1986), p. 86.
- [64] M. IANNUZZI AND J. HUTTER, *Comparative study of the nature of chemical bonding of corrugated graphene on Ru(0001) and Rh(111) by electronic structure calculations*, Surf. Sci., 605 (2011), p. 1360.
- [65] E. ILISCA, *Ortho-para conversion of hydrogen molecules physisorbed on surfaces*, Prog. Surf. Sci., 41 (1992), p. 217.
- [66] J. JACOBSEN, L. PLETH NIELSEN, F. BESENBACHER, I. STENSGAARD, E. LÆGSGAARD, T. RASMUSSEN, K. W. JACOBSEN, AND J. K. NØRSKOV, *Atomic-scale determination of misfit dislocation loops at metal-metal interfaces*, Phys. Rev. Lett., 75 (1995), p. 489.
- [67] S. KHANNA AND F. REUSE, *Hydrogen absorption around neutral and charged Ni atoms*, Chem. Phys. Lett., 205 (1993), p. 248.
- [68] K. KIM AND N. SULLIVAN, *Orientational ordering in monolayer films of molecular hydrogen on boron nitride*, J. Low Temp. Phys., 114 (1999), p. 173.
- [69] D. A. KING, *Thermal desorption from metal surfaces: A review*, Surface Science, 47 (1975), p. 384.

Bibliography

- [70] J. KLEIN, A. LÉGER, M. BELIN, D. DÉFOURNEAU, AND M. J. L. SANGSTER, *Inelastic-electron-tunneling spectroscopy of metal-insulator-metal junctions*, Phys. Rev. B, 7 (1973), p. 2336.
- [71] T. A. LAND, T. MICHELY, R. J. BEHM, J. C. HEMMINGER, AND G. COMSA, *STM investigation of the adsorption and temperature dependent reactions of ethylene on Pt(111)*, Appl. Phys. A, 53 (1991), p. 414.
- [72] ———, *STM investigation of single layer graphite structures produced on Pt(111) by hydrocarbon decomposition*, Surf. Sci., 264 (1992), p. 261.
- [73] R. LASKOWSKI AND P. BLAHA, *Ab initio study of h-BN nanomeshes on Ru(001), Rh(111), and Pt(111)*, Phys. Rev. B, 81 (2010), p. 075418.
- [74] R. LASKOWSKI, P. BLAHA, T. GALLAUNER, AND K. H. SCHWARZ, *Single-layer model of the hexagonal boron nitride nanomesh on the Rh(111) surface*, Phys. Rev. Lett., 98 (2007), p. 106802.
- [75] A. LEHNERT, P. BULUSCHEK, N. WEISS, J. GIESECKE, M. TREIER, S. RUSPONI, AND H. BRUNE, *High resolution in situ magneto-optic Kerr effect and scanning tunneling microscopy setup with all optical components in UHV*, Rev. Sci. Instrum., 80 (2009), p. 023902.
- [76] H. MA, T. BRUGGER, S. BERNER, Y. DING, M. IANNUZZI, J. HUTTER, J. OSTERWALDER, AND T. GREBER, *Nano-ice on boron nitride nanomesh: Accessing proton disorder*, ChemPhysChem, 11 (2010), p. 399.
- [77] V. MADHAVAN, W. CHEN, T. JAMNEALA, M. F. CROMMIE, AND N. S. WINGREEN, *Tunneling into a single magnetic atom: Spectroscopic evidence of the Kondo resonance*, Science, 280 (1998), p. 567.
- [78] V. MADHAVAN, W. CHEN, T. JAMNEALA, M. F. CROMMIE, AND N. S. WINGREEN, *Local spectroscopy of a Kondo impurity: Co on Au(111)*, Phys. Rev. B, 64 (2001), p. 165412.
- [79] P. MAKSYMOVYCH, D. B. DOUGHERTY, X. Y. ZHU, AND J. T. YATES, *Nonlocal dissociative chemistry of adsorbed molecules induced by localized electron injection into metal surfaces*, Phys. Rev. Lett., 99 (2007), p. 016101.
- [80] S. MARCHINI, S. GÜNTHER, AND J. WINTTERLIN, *Scanning tunneling microscopy of graphene on Ru(0001)*, Phys. Rev. B, 76 (2007), p. 075429.
- [81] D. MARTOCCIA, M. BJÖRCK, C. M. SCHLEPÜTZ, T. BRUGGER, S. A. PAULI, B. D. PATTERSON, T. GREBER, AND P. R. WILLMOTT, *Graphene on Ru(0001): a corrugated and chiral structure*, N. J. Phys., 12 (2010), p. 043028.

-
- [82] D. MARTOCCIA, P. R. WILLMOTT, T. BRUGGER, M. BJÖRCK, S. GÜNTHER, C. M. SCHLEPÜTZ, A. CERVELLINO, S. A. PAULI, B. D. PATTERSON, S. MARCHINI, J. WINTERLIN, W. MORITZ, AND T. GREBER, *Graphene on Ru(0001): A 25×25 supercell*, Phys. Rev. Lett., 101 (2008), p. 126102.
 - [83] T. MASHOFF, M. PRATZER, V. GERINGER, T. J. ECHTERMAYER, M. C. LEMME, M. LIEBMANN, AND M. MORGENSTERN, *Bistability and oscillatory motion of natural nanomembranes appearing within monolayer graphene on silicon dioxide*, Nano Lett., 10 (2010), p. 461.
 - [84] W. MORITZ, B. WANG, M. L. BOCQUET, T. BRUGGER, T. GREBER, J. WINTERLIN, AND S. GÜNTHER, *Structure determination of the coincidence phase of graphene on Ru(0001)*, Phys. Rev. Lett., 104 (2010), p. 136102.
 - [85] F. MÜLLER, S. HÜFNER, H. SACHDEV, R. LASKOWSKI, P. BLAHA, AND K. SCHWARZ, *Epitaxial growth of hexagonal boron nitride on Ag(111)*, Phys. Rev. B, 82 (2010), p. 113406.
 - [86] K. NAGAOKA, T. JAMNEALA, M. GROBIS, AND M. F. CROMMIE, *Temperature dependence of a single Kondo impurity*, Phys. Rev. Lett., 88 (2002), p. 077205.
 - [87] A. NAGASHIMA, N. TEJIMA, Y. GAMOU, T. KAWAI, AND C. OSHIMA, *Electronic dispersion relations of monolayer hexagonal boron nitride formed on the Ni(111) surface*, Phys. Rev. B, 51 (1995), p. 4606.
 - [88] ———, *Electronic structure of monolayer hexagonal boron nitride physisorbed on metal surfaces*, Phys. Rev. Lett., 75 (1995), p. 3918.
 - [89] F. D. NATTERER, F. PATTHEY, AND H. BRUNE, *Ring state for single transition metal atoms on boron nitride on Rh(111)*, Phys. Rev. Lett., 109 (2012), p. 066101.
 - [90] F. D. NATTERER, S. RUSPONI, AND H. BRUNE, *graphene on close-packed metal surfaces – long range order and band gap engineering*, SPG Mitteilungen, 34 (2011), p. 31.
 - [91] F. D. NATTERER, S. RUSPONI, M. PAPAGNO, C. CARBONE, AND H. BRUNE, *Optimizing long-range order, band gap, and group velocities for graphene on close-packed metal surfaces*, J. Phys.: Condens. Matter, 24 (2012), p. 314203.
 - [92] A. T. N'DIAYE, S. BLEIKAMP, P. J. FEIBELMAN, AND T. MICHELY, *Two-dimensional Ir cluster lattice on a graphene moiré on Ir(111)*, Phys. Rev. Lett., 97 (2006), p. 215501.
 - [93] A. T. N'DIAYE, J. CORAUX, T. N. PLASA, C. BUSSE, AND T. MICHELY, *Structure of epitaxial graphene on Ir(111)*, New J. Phys., 10 (2008), p. 043033.
 - [94] M. NIELSEN, J. P. MCTAGUE, AND W. ELLENSON, *Adsorbed layers of D₂, H₂, O₂, and ³He on graphite studied by neutron scattering*, J. Phys. Colloques, 38 (1977), p. C4.

- [95] B. NIEUWENHUYTS, D. HAGEN, G. ROVIDA, AND G. SOMORJAI, *LEED, AES and thermal desorption studies of chemisorbed hydrogen and hydrocarbons (C_2H_2 , C_2H_4 , C_6H_6 , C_6H_{12}) on the (111) and stepped $[6(111) \times (100)]$ iridium crystal surfaces; comparison with platinum*, Surf. Sci., 59 (1976), p. 155.
- [96] J. NIU, B. K. RAO, P. JENA, AND M. MANNINEN, *Interaction of H_2 and He with metal atoms, clusters, and ions*, Phys. Rev. B, 51 (1995), p. 4475.
- [97] K. S. NOVOSELOV, A. K. GEIM, S. V. MOROZOV, D. JIANG, Y. ZHANG, S. V. DUBONOS, I. V. GRIGORIEVA, AND A. A. FIRSOV, *Electric field effect in atomically thin carbon films*, Science, 306 (2004), p. 666.
- [98] K. S. NOVOSELOV, D. JIANG, F. SCHEDIN, T. J. BOOTH, V. V. KHOTKEVICH, S. V. MOROZOV, AND A. K. GEIM, *Two-dimensional atomic crystals*, PNAS, 102 (2005), p. 10451.
- [99] L. OLESEN, M. BRANDBYGE, M. R. SØRENSEN, K. W. JACOBSEN, E. LÆGSGAARD, I. STENSGAARD, AND F. BESENBACHER, *Apparent barrier height in scanning tunneling microscopy revisited*, Phys. Rev. Lett., 76 (1996), p. 1485.
- [100] F. ORLANDO, R. LARCIPRETE, P. LACOVIG, I. BOSCARATO, A. BARALDI, AND S. LIZZIT, *Epitaxial growth of hexagonal boron nitride on Ir(111)*, J. Phys. Chem. C, 116 (2012), p. 157.
- [101] A. F. OTTE, M. TERNES, K. v. BERGMANN, S. LOTH, H. BRUNE, C. P. LUTZ, C. F. HIRJIBEHEDIN, AND A. J. HEINRICH, *The role of magnetic anisotropy in the Kondo effect*, Nat. Phys., 4 (2008), p. 847.
- [102] G. PANACCIONE, I. VOBORNIK, J. FUJII, D. KRIZMANCIC, E. ANNESE, L. GIOVANELLI, F. MACCHEROZZI, F. SALVADOR, A. D. LUISA, D. BENEDETTI, A. GRUDEN, P. BERTOCH, F. POLACK, D. COCCO, G. SOSTERO, B. DIVIACCO, M. HOCHSTRASSER, U. MAIER, D. PESCIA, C. H. BACK, T. GREBER, J. OSTERWALDER, M. GALAKTIONOV, M. SANCROTTI, AND G. ROSSI, *Advanced photoelectric effect experiment beamline at elettra: A surface science laboratory coupled with synchrotron radiation*, Rev. Sci. Instrum., 80 (2009), p. 043105.
- [103] M. PAPAGNO, D. PACILÉ, D. TOPWAL, P. MORAS, P. M. SHEVERDYAEVA, F. D. NATTERER, A. LEHNERT, S. RUSPONI, Q. DUBOUT, F. CALLEJA, E. FRANTZESKAKIS, S. PONS, J. FUJII, I. VOBORNIK, M. GRIONI, C. CARBONE, AND H. BRUNE, *Two distinct phases of bilayer graphene films on Ru(0001)*, ACS Nano, 6 (2012), p. 9299.
- [104] M. PAPAGNO, S. RUSPONI, P. M. SHEVERDYAEVA, S. VLAIC, M. ETZKORN, D. PACILÉ, P. MORAS, C. CARBONE, AND H. BRUNE, *Large band gap opening between graphene Dirac cones induced by Na adsorption onto an Ir superlattice*, ACS Nano, 6 (2012), p. 199.
- [105] C. H. PARK, Y. W. SON, L. YANG, M. L. COHEN, AND S. G. LOUIE, *Landau levels and quantum hall effect in graphene superlattices*, Phys. Rev. Lett., 103 (2009), p. 046808.

-
- [106] M. PIVETTA, F. SILLY, F. PATTHEY, J. P. PELZ, AND W.-D. SCHNEIDER, *Reading the ripples of confined surface-state electrons: Profiles of constant integrated local density of states*, Phys. Rev. B, 67 (2003), p. 193402.
- [107] A. PREOBRJENSKI, M. NESTEROV, M. L. NG, A. VINOGRADOV, AND N. MÄRTENSSON, *Monolayer h-BN on lattice-mismatched metal surfaces: On the formation of the nanomesh*, Chem. Phys. Lett., 446 (2007), p. 119.
- [108] A. PREOBRJENSKI, A. VINOGRADOV, AND N. MÄRTENSSON, *Monolayer of h-BN chemisorbed on Cu(111) and Ni(111): The role of the transition metal 3d states*, Surf. Sci., 582 (2005), p. 21.
- [109] A. B. PREOBRJENSKI, A. S. VINOGRADOV, AND N. MÄRTENSSON, *Ni 3d-BN π hybridization at the h-BN-Ni(111) interface observed with core-level spectroscopies*, Phys. Rev. B, 70 (2004), p. 165404.
- [110] A. B. PREOBRJENSKI, A. S. VINOGRADOV, M. L. NG, E. ČAVAR, R. WESTERSTRÖM, A. MIKKELSEN, E. LUNDGREN, AND N. MÄRTENSSON, *Influence of chemical interaction at the lattice-mismatched h-BN/Rh(111) and h-BN/Pt(111) interfaces on the overlayer morphology*, Phys. Rev. B, 75 (2007), p. 245412.
- [111] B. RADISAVLJEVIC, A. RADENOVIC, J. BRIVIO, V. GIACOMETTI, AND A. KIS, *Single-layer MoS₂ transistors*, Nat Nano, 6 (2011), p. 147.
- [112] P. REDHEAD, *Thermal desorption of gases*, Vacuum, 12 (1962), p. 203.
- [113] J. REPP, G. MEYER, F. E. OLSSON, AND M. PERSSON, *Controlling the charge state of individual gold atoms*, Science, 305 (2004), p. 493.
- [114] E. ROKUTA, Y. HASEGAWA, K. SUZUKI, Y. GAMOU, C. OSHIMA, AND A. NAGASHIMA, *Phonon dispersion of an epitaxial monolayer film of hexagonal boron nitride on Ni(111)*, Phys. Rev. Lett., 79 (1997), p. 4609.
- [115] S. RUSPONI, M. PAPAGNO, P. MORAS, S. VLAIC, M. ETZKORN, P. M. SHEVERDYAEVA, D. PACILÉ, H. BRUNE, AND C. CARBONE, *Highly anisotropic Dirac cones in epitaxial graphene modulated by an island superlattice*, Phys. Rev. Lett., 105 (2010), p. 246803.
- [116] U. SCHLICKUM, R. DECKER, F. KLAPPENBERGER, G. ZOPPELLARO, S. KLYATSKAYA, M. RUBEN, I. SILANES, A. ARNAU, K. KERN, H. BRUNE, AND J. V. BARTH, *Metal-organic honeycomb nanomeshes with tunable cavity size*, Nano Lett., 7 (2007), p. 3813.
- [117] E. G. SEEBAUER, A. C. F. KONG, AND L. D. SCHMIDT, *Surface diffusion of hydrogen and CO on Rh(111): Laser-induced thermal desorption studies*, J. Chem. Phys., 88 (1988), p. 6597.
- [118] J. SEGUIN AND J. SUZANNE, *A LEED study of physisorbed hydrogen on graphite*, Surf. Sci. Lett., 118 (1982), p. L241.

Bibliography

- [119] A. M. SHIKIN, G. V. PRUDNIKOVA, V. K. ADAMCHUK, F. MORESCO, AND K. -H. RIEDER, *Surface intercalation of gold underneath a graphite monolayer on Ni(111) studied by angle-resolved photoemission and high-resolution electron-energy-loss spectroscopy*, Phys. Rev. B, 62 (2000), p. 13202.
- [120] M. SICOT, O. KURNOSIKOV, O. A. O. ADAM, H. J. M. SWAGTEN, AND B. KOOPMANS, *STM-induced desorption of hydrogen from Co nanoislands*, Phys. Rev. B, 77 (2008), p. 035417.
- [121] M. SICOT, O. KURNOSIKOV, H. SWAGTEN, AND B. KOOPMANS, *Hydrogen superstructures on Co nanoislands and Cu(111)*, Surf. Sci., 602 (2008), p. 3667.
- [122] I. F. SILVERA, *The solid molecular hydrogens in the condensed phase: Fundamentals and static properties*, Rev. Mod. Phys., 52 (1980), p. 393.
- [123] J. G. SIMMONS, *Electric tunnel effect between dissimilar electrodes separated by a thin insulating film*, J. Appl. Phys., 34 (1963), p. 2581.
- [124] B. C. STIPE, M. A. REZAEI, AND W. HO, *Coupling of vibrational excitation to the rotational motion of a single adsorbed molecule*, Phys. Rev. Lett., 81 (1998), p. 1263.
- [125] ———, *Single-molecule vibrational spectroscopy and microscopy*, Science, 280 (1998), p. 1732.
- [126] J. STÖHR, *NEXAFS Spectroscopy*, Springer Series in Surface Sciences, Springer-Verlag, 1992.
- [127] E. SUTTER, D. P. ACHARYA, J. T. SADOWSKI, AND P. SUTTER, *Scanning tunneling microscopy on epitaxial bilayer graphene on ruthenium (0001)*, Appl. Phys. Lett., 94 (2009), p. 133101.
- [128] P. W. SUTTER, J. -I. FLEGE, AND E. A. SUTTER, *Epitaxial graphene on ruthenium*, Nat. Mater., 7 (2008), p. 406.
- [129] K. SVENSSON, L. BENGTTSSON, J. BELLMAN, M. HASSEL, M. PERSSON, AND S. ANDERSSON, *Two-dimensional quantum rotation of adsorbed H₂*, Phys. Rev. Lett., 83 (1999), p. 124.
- [130] D. TEILLET-BILLY AND J. GAUYACQ, *Rotational excitation of physisorbed molecules by resonant electron scattering*, Surf. Sci., 502 (2002), p. 358.
- [131] R. TEMIROV, S. SOUBATCH, O. NEUCHEVA, A. C. LASSISE, AND F. S. TAUTZ, *A novel method achieving ultra-high geometrical resolution in scanning tunnelling microscopy*, New J. Phys., 10 (2008), p. 053012.
- [132] M. TERNES, *Scanning tunneling spectroscopy at the single atom scale*, PhD thesis, EPFL, 2006.
- [133] J. TERSOFF AND D. R. HAMANN, *Theory of the scanning tunneling microscope*, Phys. Rev. B, 31 (1985), p. 805.

-
- [134] A. VARYKHALOV, J. SÁNCHEZ-BARRIGA, A. M. SHIKIN, C. BISWAS, E. VESCOVO, A. RYBKIN, D. MARCHENKO, AND O. RADER, *Electronic and magnetic properties of quasifreestanding graphene on Ni*, Phys. Rev. Lett., 101 (2008), p. 157601.
- [135] A. VARYKHALOV, M. R. SCHOLZ, T. K. KIM, AND O. RADER, *Effect of noble-metal contacts on doping and band gap of graphene*, Phys. Rev. B, 82 (2010), p. 121101(R).
- [136] A. L. VAZQUEZ DE PARGA, F. CALLEJA, B. BORCA, M. C. G. PASSEGGI, J. J. HINAREJOS, F. GUINEA, AND R. MIRANDA, *Periodically rippled graphene: Growth and spatially resolved electronic structure*, Phys. Rev. Lett., 100 (2008), p. 056807.
- [137] J. A. VENABLES, G. D. T. SPILLER, AND M. HANBÜCKEN, *Nucleation and growth of thin films*, Rep. Prog. Phys., 47 (1984), p. 399.
- [138] N. A. VINOGRADOV, A. A. ZAKHAROV, V. KOCEVSKI, J. RUSZ, K. A. SIMONOV, O. ERIKSSON, A. MIKKELSEN, E. LUNDGREN, A. S. VINOGRADOV, N. MÄRTENSSON, AND A. B. PREOBRAJENSKI, *Formation and structure of graphene waves on Fe(110)*, Phys. Rev. Lett., 109 (2012), p. 026101.
- [139] N. A. VINOGRADOV, A. A. ZAKHAROV, M. L. NG, A. MIKKELSEN, E. LUNDGREN, N. MÄRTENSSON, AND A. B. PREOBRAJENSKI, *One-dimensional corrugation of the h-BN monolayer on Fe(110)*, Langmuir, 28 (2012), p. 1775.
- [140] B. WANG, M.-L. BOCQUET, S. MARCHINI, S. GUNTHER, AND J. WINTTERLIN, *Chemical origin of a graphene moiré overlayer on Ru(0001)*, Phys. Chem. Chem. Phys., 10 (2008), p. 3530.
- [141] C. WEISS, C. WAGNER, C. KLEIMANN, M. ROHLFING, F. S. TAUTZ, AND R. TEMIROV, *Imaging pauli repulsion in scanning tunneling microscopy*, Phys. Rev. Lett., 105 (2010), p. 086103.
- [142] N. WEISS, *Propriétés magnétiques de nanostructures de cobalt adsorbées.*, PhD thesis, EPFL, 2004.
- [143] R. WIDMER, D. PASSERONE, T. MATTLE, H. SACHDEV, AND O. GRÖNING, *Probing the selectivity of a nanostructured surface by xenon adsorption*, Nanoscale, 2 (2010), p. 502.
- [144] H. WIECHERT, *Adsorption of molecular hydrogen isotopes on graphite and BN*, in Landolt-Börnstein - Group III Condensed Matter, vol. 42A3, 2003.
- [145] L. YANG, C. H. PARK, Y. W. SON, M. L. COHEN, AND S. G. LOUIE, *Quasiparticle energies and band gaps in graphene nanoribbons*, Phys. Rev. Lett., 99 (2007), p. 186801.
- [146] J. ZHANG, V. SESSI, C. H. MICHAELIS, I. BRIHUEGA, J. HONOLKA, K. KERN, R. SKOMSKI, X. CHEN, G. ROJAS, AND A. ENDERS, *Ordered layers of Co clusters on BN template layers*, Phys. Rev. B, 78 (2008), p. 165430.

Curriculum Vitæ

Fabian Donat Natterer

Date of birth: 09.09.1983, Munich

Nationality: Switzerland, Germany

Education

- 2008-2012: PhD studies / teaching assistant, EPFL, Lausanne, Switzerland
- 2002-2008: Studies in Physics (diploma), University of Vienna, Austria
- 1994-2002: Federal high-school (A-level), Reutte, Austria
- 1991-1994: Primary school, Vils, Austria
- 1990-1991: Rudolf-Steiner school, Munich, Germany

Languages

German, English, French

Publications

- "*Mapping the Nuclear Spin State of Hydrogen and Deuterium with STM*", **F. D. Natterer**, F. Patthey, and H. Brune, (*in preparation*)
- "*Ti Adatoms on h-BN: The Interplay with Hydrogen*", **F. D. Natterer**, F. Patthey, and H. Brune, (*in preparation*),
- "*Two Distinct Phases of Bilayer Graphene Films on Ru(0001)*", M. Papagno, D. Pacilé, D. Topwal, P. Moras, Paolo, P. M. Sheverdyeva, **F. D. Natterer**, A. Lehnert, S. Rusponi, Q. Dubout, F. Calleja, E. Frantzeskakis, S. Pons, J. Fujii, I. Vobornik, M. Grioni, C. Carbone, and H. Brune, *ACS Nano* **6**, 9299 (2012)
- "*Ring State for Single Transition Metal Atoms on Boron Nitride on Rh(111)*", **F. D. Natterer**, F. Patthey, and H. Brune, *Phys. Rev. Lett.* **109**, 066101 (2012)
- "*Optimizing long-range Order, Band-gap, and Group Velocities for Graphene on Close-packed Metal Surfaces*", **F. D. Natterer**, S. Rusponi, M. Papagno, C. Carbone, and H. Brune, *J. Phys.: Condens. Matter* **24**, 314203 (2012)
- "*Graphene on Close-packed Metal Surfaces – long range Order and Band-gap Engineering*", **F. D. Natterer**, S. Rusponi, and H. Brune, *SPG Mitteilungen* **34**, 31 (2011)
- "*Ultrathin Mn layers on Rh(001): Investigations using Scanning Tunneling Microscopy and Density Functional Calculations*", M. Zeleny, **F. D. Natterer**, A. Biedermann, and J. Hafner, *Phys. Rev. B* **82**, 165422 (2010)

Acknowledgements

First and foremost I wish to thank my thesis advisor Prof. Harald Brune. I want to thank him for hiring me as his PhD student and for his support in adapting the means of research in the course of my thesis. The discovery of the transition metal rings as well as the rotational excitations of hydrogen molecules are direct offsprings of this vision. Furthermore, I wish to express my gratitude for letting me travel to the many conferences and lectures abroad.

I thank Prof. Karsten Albe, Prof. Thomas Greber, and Prof. Andras Kis for serving on the jury committee and Prof. Romuald Houdré for presiding.

I want to express my gratitude to François Patthey with whom most of the here presented experiments were carried out. It is because of him that much of my initial enthusiasm remained conserved. I consider myself very lucky in being his apprentice for two years. Also, I want to thank him and Marina Pivetta for creating the particular, and very pleasant Cubotron atmosphere. Furthermore, I thank Marina for her critical look at and advice for my figure drafts.

Thanks are due to Stefano Rusponi for initiating me into the labs of our group, and in letting me operate his STM for most of the graphene studies. For the additional graphene experiments I want to thank Marco Papagno, Jun Fujii and the rest of the staff at the APE beamline in Trieste.

I wish to thank Stephan Fedrigo for the collaboration in the STM construction. I want to thank him for taking over the project when I was offered the chance to extend the interim measurements at the Cubotron. I also want to thank Uta Schlickum for her supervision of the STM project at the beginning of my thesis and the technical workshop, headed by Gilles Grandjean, for the professional making of the many components.

I thank Chantal Roulin and Florence Grandjean for their greatly appreciated administrative assistance. Thanks to Martial Doy and Primo Locatelli for their IT support.

I enjoyed the pleasant lunchtime breaks with my colleagues that daily lightened up the atmosphere. I will hold our common walks to the banane and funny discussions in fond memory.

And finally, I would like to thank my family and friends for their ongoing support that helped me to navigate all the extremes the realization of a thesis naturally entails.

Lausanne, 1 January 2013

F. D. Natterer